Modern Control Approaches
for Next-Generation
Interferometric Gravitational Wave Detectors

Von der QUEST-Leibniz-Forschungsschule der
Gottfried Wilhelm Leibniz Universität Hannover
zur Erlangung des Grades
Doktor der Naturwissenschaften

genehmigte Dissertation

von

Dipl.-Phys. Dirk Schütte

2016

Referent: Juniorprof. Dr. rer. nat. Michèle Heurs
Korreferent: Prof. Dr. rer. nat. Karsten Danzmann
Tag der Disputation: 08.07.2016

Abstract

The era of gravitational wave astronomy started with the first direct detection of a gravitational wave on September 14, 2015. This measurement was accomplished by the advanced Laser Interferometer Gravitational Wave Observatory (aLIGO) in collaboration with an international gravitational wave detector (GWD) network. GWDs are highly-complex systems incorporating hundreds of nested control loops, required to reach the detector's design sensitivities. Aiming for a further sensitivity increase, resulting in an increased volume of explorable space and hence a higher event rate, various upgrades for the advanced GWDs and the development of third-generation GWDs are planned. The planned upgrades will inevitably lead to an increased complexity of the system.

In this thesis we propose and demonstrate the implementation of modern control techniques for a range of possible applications, useful for the GWD community and also the field of quantum optics in general. The important benefit of our control approach is the inherent capability of handling multiple-input multiple-output (MIMO) control problems.

We implemented an augmented linear quadratic Gaussian (LQG) controller, which included integral action, for locking a three-mirror ring cavity to the frequency of a laser. The controller acquired a stable lock and the closed-loop performance was verified via step response data.

In a second experiment we implemented an autolocking scheme by applying the combination of a linear quadratic regulator and a time-varying Kalman filter, which is a significantly enhanced version of our previous control scheme. Our controller was able to deal with detunings corresponding to the non-linear region of the error signal. We achieved improved robustness to disturbances and a faster locking time compared to a traditional (*ad hoc*) proportional-integral controller. More importantly, our control scheme automatically reacquired lock for large detunings where the error signal left its linear capture range. This feature cannot

be accomplished by linear time-invariant controllers. The results demonstrate the superior performance of our control scheme.

Further, this thesis includes investigations of describing the squeezed light source in our laboratory as a MIMO control problem, aiming for the generation of fixed-quadrature squeezing. Our result was that the feedback loops for our optical parametric oscillator and the pump phase lock were decoupled due to the applied modulation schemes. Adding the lock of the local oscillator, and defining the readout angle as a third variable led to non-vanishing coupling terms between the implemented control loops. Thus, the control of a squeezed light source can be described as a MIMO control problem, which can potentially benefit from modern control techniques.

Finally, a complex MIMO system presented by a triple pendulum suspension for seismic isolation of optical components of GWDs was investigated. The damping of the system resonances is commonly addressed via traditional control approaches, based on transfer functions obtained via co-located sensor/actuator pairs attached to the upper mass. The limitation of this approach is the lack of reliable information about the motion of the lower mass. We are the first to propose a controller design which incorporates information about lower mass motion. A generalised control formulation was used to examine the implementation of $\mathcal{H}_\infty/\mathcal{H}_2$ controller synthesis techniques allowing for controller frequency weighting and the consideration of coloured noises. The result of our computation was a 75th-order controller achieving damping factors of $\approx 50\,\mathrm{dB}$ without significantly exciting other modes.

The results of this thesis demonstrate that modern control techniques can be beneficial for complex systems such as they occur in quantum optics, and in particular in interferometric gravitational wave detectors. A mathematical control approach is advantageous, as it offers unique controller design possibilities.

Keywords:
Modern Control, Cavity locking, Autolocking, Squeezed states, Seismic isolation

Kurzfassung

Die Ära der Gravitationswellenastronomie begann mit dem ersten direkten Nachweis einer Gravitationswelle am 14. September 2015. Der Nachweis wurde durch die aLIGO-Gravitationswellendetektoren in Zusammenarbeit mit einem internationalen Gravitationswellendetektoren-Netzwerk (GWD) geliefert. GWD sind hochkomplexe Systeme, die hunderte verschachtelte Regelkreise enthalten, welche erforderlich sind, um die GWD im Detektionsmodus zu halten und die gewünschte Sensitivität des Detektors zu gewährleisten.

Eine weitere Steigerung der Empfindlichkeit wird das erforschbare Volumen des Weltraums und damit die Rate der gemessenen Ereignisse erhöhen. Um dies zu erreichen, sind verschiedene Verbesserungen für die nächste GWD Generation vorgesehen, die Entwicklung einer dritten Generation ist bereits in Planung. Diese geplanten Verbesserungen werden unweigerlich zu einer erhöhten Komplexität des Systems führen.

In der vorliegenden Arbeit empfehlen und demonstrieren wir die Anwendung moderner Regelungstechniken für eine Vielfalt von Anwendungsmöglichkeiten, die für die GWD Gemeinschaft und auch für den Bereich der Quantenoptik im Allgemeinen nützlich sein können. Der wichtige Vorteil unseres Regelungsansatzes ist die inhärente Fähigkeit, Multiple-Input-Multiple-Output-Regelungsprobleme (MIMO) händeln zu können.

Wir implementierten einen linearen-quadratischen-Gaußschen (LQG) Regler, erweitert um einen Integrator, zur Stabilisierung eines Drei-Spiegel-Resonators auf die Frequenz eines Lasers. Der Regler ermöglichte eine stabile Regelung des Resonators. Das Leistungsvermögen des geschlossenen Regelkreises wurde über Sprungantworten verifiziert.

In einem zweiten Experiment realisierten wir einen vollautomatischen Regelkreis durch die Kombination eines LQ-Reglers mit einem zeitveränderlichen Kalman Filter. Der neu entworfene Regelkreis stellt eine deutlich weiterentwickelt und

KURZFASSUNG

verbesserte Version des ersten Reglers dar. Unser Regler konnte Frequenzverstimmungen händeln, die dem nichtlinearen Bereich des Fehlersignals entsprechen. Wir erreichten eine verbesserte Unempfindlichkeit gegenüber Störungen und eine schnellere Systemantwort, verglichen mit einem traditionellen (*ad hoc*) Proportional-Integral-Regler. Wichtiger ist, dass unser Regler in der Lage war das System auch für große Verstimmungen vollautomatisch zu stabilisieren. Dieses Leistungsmerkmal kann nicht mit linearen, zeitinvariante, Regler erreicht werden. Die Ergebnisse legen die überlegene Leistungsfähigkeit unseres Regelkreises offenkundig dar.

Des Weiteren umfasst diese Arbeit Untersuchungen zur möglichen Beschreibung der in unserem Labor aufgebauten Quetschlichtquelle als MIMO-Regelungsproblem. Hier ist das Ziel, die Varianz einer Quadratur gezielt zu verringern. Wir konnten feststellen, dass die Regelkreise für den optischen parametrischen Oszillator und die Phase des Pumplichtes aufgrund der verwendeten Modulationsschemata zunächst entkoppelt sind. Die Berücksichtigung des Lokaloszillator-Regelkreises, wodurch der Auslesewinkel als dritte zu kontrollierende Variable eingeführt wird, führt dann zu nicht verschwindenden Kopplungstermen zwischen den verwendeten Regelschleifen. Somit kann die Regelung einer Quetschlichtquelle als MIMO-System beschrieben werden, die möglicherweise von dem Einsatz moderner Regelungstechniken profitieren kann.

Abschließend wurde ein komplexes MIMO-System, bestehend aus einem dreifach aufgehängten Pendel zur seismischen Isolierung der Optiken eines GWDs, untersucht. Die Dämpfung der Eigenfrequenzen des Systems wird für gewöhnlich mittels traditioneller Regelungstechnikansätze realisiert, welche auf Übertragungsfunktionen basieren, die durch an der oberen Testmasse nebeneinander angebrachte Sensoren/Aktuatoren Paare bestimmt werden. Dieser Ansatz ist durch den Mangel an zuverlässigen Informationen über die Bewegung der unteren Masse limitiert. Zum ersten Mal wurde hier ein Regelungsentwurf vorgestellt, der Informationen über die Bewegung der unteren Masse beinhaltet. Eine allgemeine Kontrollformulierung wurde verwendet, um den möglichen Einsatz von $\mathcal{H}_\infty/\mathcal{H}_2$ Reglern zu untersuchen. Diese allgemeine Kontrollformulierung ermöglicht die Betrachtung von farbigem Rauschen und die Verwendung von frequenzabhängigen Gewichtungsfunktionen. Das Ergebnis unseres Reglerentwurfs war ein Regler 75. Ordnung, welcher Dämpfungsfaktoren von ca. $50\,\mathrm{dB}$ erreichte, ohne anderweitige Eigenmoden anzuregen.

Die Ergebnisse dieser Arbeit verdeutlichen, dass moderne Regelungstechnik für

vi

komplexe Systeme, wie sie in der Quantenoptik oder im Gebiet der laserinterfer-ometrischen Gravitationsphysik auftreten, vorteilhaft sein kann. Ein mathematis-cher Regelungsansatz bietet einzigartige Möglichkeiten für Regelkreisentwürfe.

Stichwörter:
Modern Regelungstechnik, Resonatorstabilisierung, vollautomatische Regelung, gequetschte Zustände, Seismische Isolierung

Contents

List of Figures

List of Tables

List of Abbreviations

GW	Gravitational Wave
LIGO	Laser Interferometer Gravitational Wave Observatory
GWD	Gravitational Wave Detector
DFG	Difference-Frequency Generation
SFG	Sum-Frequency Generation
SHG	Second-Harmonic Generation
OPO	Optical Parametric Oscillation
OPA	Optical Parametric Amplification
PPKTP	Periodically Poled Potassium Titanyl Phosphate
BS	Beamsplitter
dB	Decibel
PD	Photodetector
HD	Homodyne Detector
PBS	Polarising Beamsplitter
LO	Local Oscillator
FSR	Free Spectral Range
FWHM	Full Width Half Maximum

LIST OF ABBREVIATIONS

$\mathcal{F}$	Finesse
PDH	Pound-Drever-Hall
ROC	Radius of Curvature
LTI	Linear Time Invariant
FFT	Fast Fourier Transform
PI	Proportional Integral
LQR	Linear Quadratic Regulator
$\mathcal{C}$	Controllability matrix
$\mathcal{O}$	Observability matrix
LQG	Linear Quadratic Gaussian
SISO	Single Input Single Output
PZT	Piezoelectric Transducer
DSA	Digital Signal Analyser
PEM	Prediction Error Minimisation
DAC	Digital-to-Analog-Converter
ADC	Analog-to-Digital-Converter
TVKF	Time-Varying Kalman Filter
Nd:YAG	Neodymium-Doped Yttrium Aluminium Garnet
MgO:LiNbO$_3$	Magnesium Oxide-Doped Lithium Niobate
NTC	Negative Temperature Coefficient
MC	Modecleaner
TEM	Transverse Electromagnetic
DOF	Degree of Freedom
MIMO	Multiple Input Multiple Output
BOSEM	Birmingham Optical Sensor and

	Electro-Magnetic actuator
LED	Light-Emitting Diode
RMS	Root Mean Square
QPD	Quadrant Photodiode
CDS	Control and Data Acquisition System
DTT	Diagnostic Test Tools

1

Introduction

1.1 History of Gravitational Waves

The first direct detection of a gravitational wave (GW) event on the 14th September 2015 opened a new era of astronomy [1]. Gravitational wave astronomy is the only way to gain deep insight into the dynamics of black holes and other stellar phenomena such as spinning neutron stars or binary systems [2, 3].

The foundation for this field of astronomy was built 100 years ago. Shortly after Einstein published his General Theory of Relativity in 1915, the existence of gravitational waves was predicted [4, 5]. These waves, propagating with the speed of light through our universe, are a direct consequence of accelerated massive objects, which perturb space-time. An indirect proof of gravitational waves was accomplished by the astronomers Hulse and Taylor by exploring the binary neutron star system PSR 1913+16 [6]. They observed a decrease in the orbital period of the pulsar, travelling around its companion star, which matched Einstein's prediction and suggested that this system emits gravitational waves [7]. In 1993 Hulse and Taylor received the Nobel Prize for their discovery [8, 9].

It took another two decades of research for the first direct detection of GWs, which can be considered as one of the greatest experimental challenges of contemporary physics. Even Einstein himself doubted that a direct detection would be possible. In the 60s one of the first detection schemes was designed by Weber at the University of Maryland and the Argonne National Laboratory [10, 11]. It was based on cylindrical aluminium bars, whose resonant mode should be ex-

cited by a gravitational wave and the resulting motion could be detected by a piezoelectric transducer. However, the narrow sensitivity bandwidth of the bar detectors was a drawback, since gravitational wave sources cover a broad spectrum [12].

A broadband detector, as it is formed by a laser interferometer, was suggested by Gertsenshtein [13]. In the 70s Weiss, Drever and Thorne carried Gertsenshtein's idea forward and conducted a realistic noise budget analysis for laser interferometric gravitational wave detectors (GWD) [14]. That was the beginning of a detection scheme whose advanced generation finally managed to detect a gravitational wave emitted by a binary black hole merger.

1.2 Advanced Detectors

There exists an international network of advanced laser interferometric gravitational wave detectors. It consists of the French-Italian VIRGO detector near Pisa, with an armlength of 3 km [15], the two 4 km long American LIGO detectors [16] in Livingston and Hanford, and the British-German detector GEO600 [17] near Hannover with an effective armlength of 1.2 km. A Japanese detector called KAGRA [18] is currently under construction at the Kamioka mine, and there are also existing plans for a LIGO-like detector in India [19].

All detectors apply an improved topology of a basic Michelson interferometer for the detection of a gravitational wave. With the beamsplitter as reference point, the effect of a GW is the shortening of one interferometer arm while extending the other periodically. The size of the length variation and therefore the amplitude of the gravitational wave is defined as strain h, where $h = \Delta L/L$ is the length change ΔL over the armlength L. The induced phase shift results in a detectable change of the interferometer's output power.

Although only the two advanced LIGO detectors were operating at the time of the detection of the gravitational wave signal GW150914, it is noteworthy that key technologies required to achieve a adequately sensitivity (see Fig. 1.1) were provided by the GEO600 collaboration. Firstly the laser system [21], which is the core of a laser interferometric gravitational wave detector, is provided by the GEO collaboration. Other contributions are the monolithic suspension [22] and the signal recycling technique [23]. Another technique, proposed by Caves in 1981 [24], suggested to inject squeezed vacuum into the dark port of the gravitational wave detector to improve its sensitivity corresponding to the shot noise
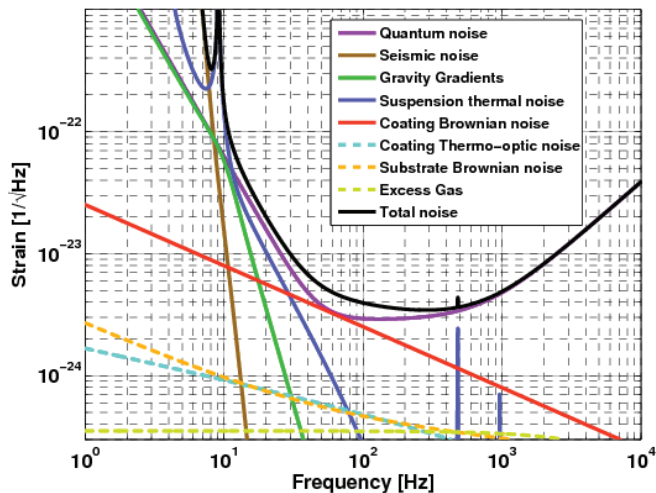
Figure 1.1: Simulated design sensitivity of advanced LIGO [20].

limited frequency range. This was implemented by Vahlbruch *et al.* in GEO600 [25, 26] and is now in permanent operation.

However, all these techniques would be useless without a suitable control scheme, which keeps the entire system at its desired operating point. This is the reason why the advanced gravitational wave detectors employ hundreds of nested feed-back loops.

This thesis aims to pave the way for the implementation of modern control techniques to the field of quantum optics, and in particular interferometric GWD. Mathematical control techniques, inherently capable of coping with undesired coupling terms, become advantageous for complex multiple-input multiple-output systems, for which an intuitive controller design approach is not feasible. The benefits of a mathematical control approach were already demonstrated in 1868 by James Clerk Maxwell (who not only postulated the well-known basis for electromagnetic fields [27]) in his paper *On Governors* [28]. Maxwell used differential equations to derive the flyball governor dynamics and was thereby able to explain occurring instabilities. Modern control techniques follow a similar approach, where first-order differential equations link the inputs, outputs and state variables for the derivation of a mathematical model of the considered sys-

tem. Another powerful tool of modern control techniques is Kalman filtering [29], named after its developer, enabling the estimation of inaccessible system states, which need to be controlled. The capability of Kalman filtering was impressively demonstrated during the Apollo program, which managed to land the first humans on the Moon. Hereby a Kalman filter was used for Apollo's onboard trajectory estimation.

This thesis explores the benefits of a systematic controller design for a variety of control problems that occur in a quantum optics laboratory. The covered problems include locking of an optical resonator, generation of stable non-classical fixed quadrature light, and control of seismic isolation systems. This research can be beneficial for complex, coupled systems in general. A good example of such a system is the *Coherent Quantum Noise Cancellation* scheme [30], which requires locking of at least two coupled cavities.

1.3 Structure of the Thesis

In Chapter 2 we introduce the theoretical description of light fields and their corresponding quadrature operators required for the theoretical model of the cavity locking experiment.

Chapter 3 establishes the basics of non-linear optics. This theoretical groundwork is needed to describe the generation and detection of squeezed states and the impact of losses.

In Chapter 4 we investigate the properties of optical cavities, including their interacting light fields. We also introduce the non-linear error signal, whose linear region is commonly used to acquire cavity lock if the cavity fulfils the stability criterion.

In Chapter 5 we formulate the control theory framework used throughout this thesis. This framework extends the general ideas of feedback control to state-space control and explains the functionality of optimal observers.

Chapter 6 makes use of the introduced state-space control methods for the purpose of locking a three-mirror ring cavity to the frequency of a laser. We experimentally demonstrate the possibility to acquire cavity lock by the implementation of a linear quadratic Gaussian controller with additional integral action. The results were published in [31].

In Chapter 7 we carried the previous controller design forward to demonstrate

a powerful autolocking scheme for optical cavities. We applied a time-varying Kalman filter for the realisation of our control scheme, capable of handling the non-linear region of the error signal, and this allowed us to acquire lock from any operating point. The results validate our control scheme and are published in [32].

Chapter 8 addresses the generation of squeezed states as a multiple-input multiple-output control problem, which can potentially benefit from a systematic control approach.

In Chapter 9 we investigate the control problem dealing with the damping of eigenfrequencies of triple pendulum suspensions, which are used to isolate optical components from seismic noise. We demonstrate a possibility to augment the usually used upper mass to upper mass transfer functions with upper mass to lower mass transfer functions, which have never been incorporated in a controller design before. The result is a $\mathcal{H}_2$ controller, obtained via a mixed-sensitivity control approach, controlling the three relevant degrees of freedom.

Chapter 10 concludes this work and summarises the advantages of modern control approaches.

2

Theory of Electromagnetic Fields

This chapter outlines the quantisation of electromagnetic fields and introduces the operator notation to describe coherent states. These states describe a single-mode laser field, which is the foundation of the quantum optical experiments realised in our laboratory. Coherent states are also required to derive the input-output formalism of optical cavities. This theoretical background provides the basis for a systematic control approach which is applied to cavity length stabilisation. The description of the dynamics of quantum optical systems follows [33, 34].

2.1 Quantised Electromagnetic Field

Maxwell's equations [27] classically describe freely propagating electromagnetic fields. In the absence of matter, they can be written in SI units as follows

$$\vec{\nabla} \cdot \vec{B} = 0 \qquad\qquad \vec{\nabla} \cdot \vec{E} = 0$$
$$\vec{\nabla} \times \vec{B} = \mu_0 \epsilon_0 \frac{\partial E}{\partial t} \qquad\qquad \vec{\nabla} \times \vec{E} = -\frac{\partial B}{\partial t}, \qquad (2.1)$$

where ϵ_0 is the electric permittivity in vacuum, μ_0 is the magnetic permeability in vacuum and $\vec{E}$ and $\vec{B}$ are the electric and magnetic field vectors, respectively. Applying the curl operator to the curl equations yields the wave equation

$$\nabla^2 \vec{E} - \mu_0 \epsilon_0 \frac{\partial^2 \vec{E}}{\partial t^2} = 0, \qquad (2.2)$$

which describes the propagation of an electric field in vacuum.

Let x, y, z define the three spatial axes. Taking the special case of a lossless one-dimensional standing wave cavity along the z-axis into consideration, a single mode electric field, polarised along the x-axis, satisfying Eq. (2.2) can be expressed as

$$E_x(z, t) = \left(\frac{2\omega^2}{V\epsilon_0} \right)^{\frac{1}{2}} q(t) \sin(kz), \tag{2.3}$$

with ω the frequency of the single-mode and k the corresponding wave number. V is the effective volume of the cavity and $q(t)$ acts as a canonical position. The magnetic field associated with the electric field of the cavity can be written as

$$B_y = \left(\frac{\mu_0 \epsilon_0}{k} \right) \left(\frac{2\omega^2}{V\epsilon_0} \right)^{\frac{1}{2}} \dot{q}(t) \cos(kz), \tag{2.4}$$

where $\dot{q}(t)$ can be regarded as a canonical momentum of a particle of unit mass

$$p(t) = \dot{q}(t). \tag{2.5}$$

The canonical position and momentum arise from Hamiltonian mechanics [35] and are utilised below. The energy of the electromagnetic field is given by the Hamiltonian H,

$$H = \frac{1}{2} \int_0^V dV \left(\epsilon_0 E_x^2(z, t) + \frac{1}{\mu_0} B_y^2(z, t) \right). \tag{2.6}$$

This expression can be reduced to [33]

$$H = \frac{1}{2}(p^2 + \omega^2 q^2), \tag{2.7}$$

showing that the single-mode field is equivalent to a harmonic oscillator of unit mass. In this context it is possible to exchange the canonical variables p and q with their dedicated operators $\hat{p}$ and $\hat{q}$, satisfying the canonical commutation relation

$$[\hat{q}, \hat{p}] = i\hbar. \tag{2.8}$$

The Hamiltoninan then becomes

$$\hat{H} = \frac{1}{2}(\hat{p}^2 + \omega^2 \hat{q}^2), \tag{2.9}$$

allowing for the convenient introduction of the non-Hermitian, and therefore non-observable, annihilation ($\hat{a}$) and creation ($\hat{a}^\dagger$) operators. These operators are defined as [33]

$$\hat{a} = (2\hbar\omega)^{-\frac{1}{2}}(\omega\hat{q} + i\hat{p}), \tag{2.10}$$

$$\hat{a}^\dagger = (2\hbar\omega)^{-\frac{1}{2}}(\omega\hat{q} - i\hat{p}), \tag{2.11}$$

with

$$\hbar = \frac{h}{2\pi}, \tag{2.12}$$

where h is the Planck constant [36]. The operators fulfil the commutation relation

$$[\hat{a}, \hat{a}^\dagger] = \hat{a}\hat{a}^\dagger - \hat{a}^\dagger\hat{a} = 1. \tag{2.13}$$

Now the Hamiltonian can be expressed as

$$\hat{H} = \hbar\omega\left(\hat{a}^\dagger\hat{a} + \frac{1}{2}\right). \tag{2.14}$$

An energy eigenstate of the single-mode field with its related energy eigenvalue E_n is denoted by $|n\rangle$ and leads to

$$\hat{H}|n\rangle = \hbar\omega(\hat{a}^\dagger\hat{a} + \frac{1}{2})|n\rangle = E_n|n\rangle. \tag{2.15}$$

$|n\rangle$ is know as a *number* or *Fock state*, which is a state with a defined photon number n.

Multiplying Eq. (2.15) by $\hat{a}^\dagger$ results in another eigenvalue equation

$$\hbar\omega\left(\hat{a}^\dagger\hat{a}^\dagger\hat{a} + \frac{1}{2}\hat{a}^\dagger\right)|n\rangle = E_n\hat{a}^\dagger|n\rangle. \tag{2.16}$$

Taking the Eq. (2.13) into account Eq. (2.16) becomes

$$\hbar\omega(\hat{a}^\dagger\hat{a} + \frac{1}{2})(\hat{a}^\dagger|n\rangle) = (E_n + \hbar\omega)(\hat{a}^\dagger|n\rangle). \tag{2.17}$$

This shows the eigenvalue problem for the eigenstate $\hat{a}^\dagger|n\rangle$ with the energy eigenvalue $E_n + \hbar\omega$. From this relation it is obvious why $\hat{a}^\dagger$ is called the creation operator: it *creates* a *quantum* of energy $\hbar\omega$. Similarly, the eigenvalue problem

for $\hat{a}\,|n\rangle$ can be derived, showing that the annihilation operator $\hat{a}$ *destroys* a quantum of energy. The eigenstate $\hat{a}\,|n\rangle$ has the energy eigenvalue $E_n - \hbar\omega$. Applying the annihilation operator multiple times will lower the energy eigenvalue, but the energy of the harmonic oscillator cannot be negative. Hence, there must be a ground state $|0\rangle$ satisfying the following condition [33],

$$\hat{H}(\hat{a}\,|0\rangle) = E_0 - \hbar\omega(\hat{a}\,|0\rangle) = 0 \tag{2.18}$$

with

$$\hat{a}\,|0\rangle = 0. \tag{2.19}$$

The eigenvalue problem of the ground state

$$\hat{H}\,|0\rangle = \hbar\omega\left(\hat{a}^{\dagger}\hat{a} + \frac{1}{2}\right)|0\rangle = \frac{1}{2}\hbar\omega\,|0\rangle \tag{2.20}$$

defines the lowest-energy eigenvalue $E_0 = \frac{1}{2}\hbar\omega$. The energy eigenvalues E_n are generally described by

$$E_n = \hbar\omega\left(n + \frac{1}{2}\right), \tag{2.21}$$

regarding the effect of the creation and annihilation operators. Looking at Eq. (2.15) suggests the definition of a number operator $\hat{n} = \hat{a}^{\dagger}\hat{a}$, where

$$\hat{n}\,|n\rangle = n\,|n\rangle. \tag{2.22}$$

For the annihilation operator acting on a number state the expression

$$\hat{a}\,|n\rangle = c_n\,|n-1\rangle, \tag{2.23}$$

is obtained, where c_n is a constant to be determined, which is derived via normalisation

$$(\langle n|\,\hat{a}^{\dagger})(\hat{a}\,|n\rangle) = \langle n|\,\hat{a}^{\dagger}\hat{a}\,|n\rangle = n \tag{2.24}$$

$$= \langle n-1|\,c_n^{*}c_n\,|n-1\rangle = \left|c_n^2\right|. \tag{2.25}$$

Thus it appears that $\left|c_n^2\right| = n$. Hence,

$$\hat{a}\,|n\rangle = \sqrt{n}\,|n-1\rangle \quad \text{and} \quad \hat{a}^{\dagger}\,|n\rangle = \sqrt{n+1}\,|n+1\rangle. \tag{2.26}$$

This expression highlights that an arbitrary number state $|n\rangle$ can be created from the ground state $|0\rangle$, also known as *vacuum state*, by applying the creation operator $\hat{a}^{\dagger}$ repeatedly

$$|n\rangle = \frac{(\hat{a}^{\dagger})^n}{\sqrt{n!}}\,|0\rangle. \tag{2.27}$$

2.2 Quantum Fluctuations

The previously determined energy of a number state is well defined in contrast to the electric field of such states

$$\langle n | \hat{\mathrm{E}}_x(z,t) | n \rangle = \epsilon_0 \sin(kz)(\langle n | \hat{a} | n \rangle + \langle n | \hat{a}^\dagger | n \rangle), \qquad (2.28)$$

where the mean field vanishes, but the energy density of the field is non-zero

$$\langle n | \hat{\mathrm{E}}_x^2(z,t) | n \rangle = 2\epsilon_0^2 \sin^2(kz) \left(n + \frac{1}{2} \right). \qquad (2.29)$$

The variance of the field is a suitable quantity to characterise these fluctuations

$$\left\langle (\Delta \hat{\mathrm{E}}_x(z,t))^2 \right\rangle = \left\langle \hat{\mathrm{E}}_x^2(z,t) \right\rangle - \left\langle \hat{\mathrm{E}}_x(z,t) \right\rangle^2. \qquad (2.30)$$

For a number state $|n\rangle$ we obtain

$$\Delta \mathrm{E}_x = \sqrt{2} \epsilon_0 \sin(kz) \left(n + \frac{1}{2} \right)^{\frac{1}{2}}, \qquad (2.31)$$

yielding the fact that even a field with $n = 0$ possesses non-zero energy. These energy fluctuations are known as *vacuum fluctuations*.

2.3 Quadrature Operators

The quadrature operators are introduced for the description of electromagnetic fields and can be expressed as linear combinations of the annihilation and creation operators

$$\hat{X}^+ = \frac{1}{2}(\hat{a} + \hat{a}^\dagger), \qquad (2.32)$$

$$\hat{X}^- = \frac{1}{2i}(\hat{a} - \hat{a}^\dagger), \qquad (2.33)$$

where $\hat{X}^+$ and $\hat{X}^-$ are known as the *amplitude* and *phase quadrature* operators, respectively. An arbitrary quadrature operator can be expressed as

$$\hat{X}_\theta = \hat{X}^+ \cos(\theta) + \hat{X}^- \sin(\theta). \qquad (2.34)$$

Explicitly taking the time dependence of the electric field into account the following equation is obtained

$$\hat{E}_x(t) = \epsilon_0(\hat{a}e^{-i\omega t} + \hat{a}^\dagger e^{i\omega t})\sin(kz). \tag{2.35}$$

Using the quadrature operators Eq. 2.35 becomes

$$\hat{E}_x(t) = 2\epsilon_0\sin(kz)\left[\hat{X}^+\cos(\omega t) + \hat{X}^-\sin(\omega t)\right]. \tag{2.36}$$

Eq. (2.36) illustrates that $\hat{X}^+$ and $\hat{X}^-$ act as field amplitudes oscillating out of phase with each other by $90°$. They satisfy the commutation relation

$$\left[\hat{X}^+, \hat{X}^-\right] = \frac{i}{2}, \tag{2.37}$$

which leads to the Heisenberg uncertainty relation [37]

$$\left\langle(\Delta\hat{X}^+)^2\right\rangle\left\langle(\Delta\hat{X}^-)^2\right\rangle \geq \frac{1}{16}. \tag{2.38}$$

For number states the expectation values for the quadrature operators are

$$\langle n|\hat{X}^+|n\rangle = 0 \tag{2.39}$$
$$\langle n|\hat{X}^-|n\rangle = 0 \tag{2.40}$$

but

$$\langle n|(\hat{X}^+)^2|n\rangle = \frac{1}{4}\langle n|\hat{a}^2 + (\hat{a}^\dagger)^2 + 2\hat{a}\hat{a}^\dagger + 1|n\rangle \quad = \frac{1}{4}(2n+1), \quad (2.41)$$
$$\langle n|(\hat{X}^-)^2|n\rangle = -\frac{1}{4}\langle n|\hat{a}^2 + (\hat{a}^\dagger)^2 + 2\hat{a}\hat{a}^\dagger - 1|n\rangle \quad = \frac{1}{4}(2n+1), \quad (2.42)$$

showing that the fluctuations in both quadratures are identical and that the ground state minimises them

$$\left\langle(\Delta\hat{X}^+)^2\right\rangle_0 = \frac{1}{4} = \left\langle(\Delta\hat{X}^-)^2\right\rangle_0. \tag{2.43}$$

Furthermore, a vacuum state is called *minimum uncertainty state*, as it minimises the inner uncertainty product Eq. (2.38).

2.4 Coherent States

Fock states $|n\rangle$ are appropriate to describe low photon number fields, but are impractical to describe classical laser light, since they have a uniform phase distribution and therefore the phase is not well-defined. Even for $n \to \infty$ the expectation value of the electric field operator vanishes $\langle n| \hat{E}_x |n\rangle = 0$, although it is known that a classical field periodically oscillates in time with respect to a fixed point in space [33]. The concept of coherent states [38] overcomes these problems and is better suited to describe classical fields, although it is a quantum mechanical state.

It is derived that states describing a classical field in a suitable way are given by the eigenstates of the annihilation operator $|\alpha\rangle$. They fulfil the relation

$$\hat{a} |\alpha\rangle = \alpha |\alpha\rangle , \tag{2.44}$$

where α is a complex number, since $\hat{a}$ is a non-Hermitian operator. It is possible to rewrite $|\alpha\rangle$ in terms of number states $|n\rangle$ forming a complete basis

$$|\alpha\rangle = \sum_{n=0}^{\infty} C_n |n\rangle . \tag{2.45}$$

Then Eq. (2.44) becomes

$$\hat{a} |\alpha\rangle = \hat{a} \sum_{n=0}^{\infty} C_n |n\rangle \tag{2.46}$$

$$= \sum_{n=1}^{\infty} C_n \sqrt{n} |n-1\rangle \overset{!}{=} \alpha \sum_{n=0}^{\infty} C_n |n\rangle \tag{2.47}$$

$$\tag{2.48}$$

and

$$C_n \sqrt{n} = \alpha C_{n-1}. \tag{2.49}$$

Rearranging Eq. (2.49) yields

$$C_n = \frac{\alpha}{\sqrt{n}} C_{n-1}$$

$$= \frac{\alpha^2}{\sqrt{n(n-1)}} C_{n-2} = ...$$

$$= \frac{\alpha^n}{\sqrt{n!}} C_0. \tag{2.50}$$

Reformulating Eq. (2.45) leads to

$$|\alpha\rangle = C_0 \sum_{n=0}^{\infty} \frac{\alpha^n}{\sqrt{n!}} |n\rangle , \tag{2.51}$$

where the constant C_0 is again obtained via the normalisation requirement $\langle \alpha | \alpha \rangle = 1$, resulting in

$$|\alpha\rangle = e^{-\frac{1}{2}|\alpha|^2} \sum_{n=0}^{\infty} \frac{\alpha^n}{\sqrt{n!}} |n\rangle . \tag{2.52}$$

Upon closer examination it can be seen that this *coherent state* has a non-vanishing expectation value for the electric field operator. More precisely its expectation value reflects the dynamics of a classical field. Furthermore it can be shown that a coherent state only exhibits vacuum fluctuations. From the expectation value of the electric field operator in polar form

$$\langle \alpha | \hat{E}_x(r, t) | \alpha \rangle = 2 |\alpha| \left(\frac{\hbar \omega}{2 \epsilon V} \right)^{\frac{1}{2}} \sin(\omega t - kr - \theta), \tag{2.53}$$

$|\alpha|$ can be seen as the amplitude of the field. Thus the expectation value of the number operator is

$$\bar{n} = \langle \alpha | \hat{n} | \alpha \rangle = |\alpha|^2 , \tag{2.54}$$

and the resulting $|\alpha|^2$ is the average photon number. Resolving the fluctuations of the photon number Δn, it is necessary to derive the expectation value of $\hat{n}^2$

$$\langle \alpha | \hat{n}^2 | \alpha \rangle = \bar{n}^2 + \bar{n}, \tag{2.55}$$

which leads to

$$\Delta n = \sqrt{\langle \hat{n}^2 \rangle - \langle \hat{n} \rangle^2} = \sqrt{\bar{n}}. \tag{2.56}$$

This behaviour is characteristic of a Poisson process [33].
Another way of defining a coherent state is given by the application of a unitary displacement operator $\hat{D}$ to the ground state $|0\rangle$

$$|\alpha\rangle = \hat{D}(\alpha) |0\rangle \tag{2.57}$$

$$= e^{-\frac{1}{2}|\alpha|^2} \sum_{n=0}^{\infty} \frac{\alpha^n}{\sqrt{n!}} |n\rangle \tag{2.58}$$
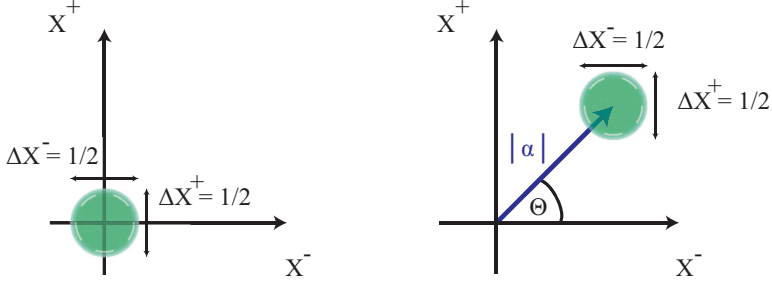
Figure 2.1: The left illustration shows the ground state $n = 0$ with its corresponding fluctuations associated with the field quadratures. On the right hand side a coherent state of amplitude $|\alpha|$, phase Θ and uniformly distributed minimal fluctuations is depicted.

where

$$\hat{D}(\alpha) = e^{(\alpha\hat{a}^\dagger - \alpha^*\hat{a})}. \tag{2.59}$$

A coherent state with an amplitude α, a phase angle Θ and field fluctuations corresponding to uniform vacuum fluctuations

$$\Delta\hat{X}^+ = \Delta\hat{X}^- = \frac{1}{2} \tag{2.60}$$

is illustrated in Fig. 2.1 in a *phase-space representation* [34]. It shows two coherent states with $n = 0$ and $n = \alpha$. The derivation of coherent states, describing a laser field, allows for introduction of an input/output formalism capable of describing the dynamics of optical cavities. This formalism is used in upcoming chapters.

<div style="text-align: right">**3**</div>

Non-Linear Optics

In this chapter a quantum-mechanical description of squeezed states will be established. Furthermore the physical parameters for generating and detecting squeezed states are discussed and characterised. This theoretical background gives helpful insights for designing control loops required for stable cavity-enhanced squeezing, which is one goal of the thesis. The discussion in this entire chapter follows the methodologies used in [33] and [39].

3.1 Squeezed States

Any two operators satisfying the commutation relation $\left[\hat{A}, \hat{B}\right] = i\hat{C}$ result in [33]

$$\left\langle (\Delta \hat{A})^2 \right\rangle \left\langle (\Delta \hat{B})^2 \right\rangle \geq \frac{1}{4} \left| \left\langle \hat{C} \right\rangle \right|^2. \tag{3.1}$$

Substituting $\hat{X}^{\pm}$ for $\hat{A}, \hat{B}$ and taking into account that coherent states are minimum uncertainty states,

$$\left\langle (\Delta \hat{X}^+)^2 \right\rangle = \left\langle (\Delta \hat{X}^-)^2 \right\rangle = \frac{1}{4}, \tag{3.2}$$

Eq. (3.1) can be converted into

$$\left\langle (\Delta \hat{X}^+)^2 \right\rangle \left\langle (\Delta \hat{X}^-)^2 \right\rangle = \frac{1}{16}. \tag{3.3}$$

This uncertainty product defines a lower limit for the product of the quadrature fluctuations. However it does not prohibit the case of one quadrature operator exhibiting a lower uncertainty than the ground state, as long as the other quadrature operator shows an increased uncertainty such that the commutation relation is still valid. A state which has a non-uniform fluctuation distribution with

$$\left\langle (\hat{X}^{\pm})^2 \right\rangle < \frac{1}{4} \tag{3.4}$$

is called a *squeezed state*.

In a theoretical approach the generation of a squeezed state can be achieved by a squeezing operator [33], acting on a state. The operator is defined as

$$\hat{S}(\xi) = e^{\left[\frac{1}{2}(\xi^*\hat{a}^2 - \xi\hat{a}^{\dagger 2})\right]}, \tag{3.5}$$

where

$$\xi = re^{i\Theta}. \tag{3.6}$$

r and Θ are known as *squeezing parameter* and *squeezing angle*, respectively, with

$$0 \le r < \infty, \qquad 0 \le \Theta \le 2\pi. \tag{3.7}$$

The squeezing operator $\hat{S}(\xi)$ can be considered as a two-photon generalisation of the displacement operator, see Eqs. (2.57)-(2.58). $\hat{S}(\xi)$ always creates or destroys photons in pairs. To determine the variances of a squeezed state, the expectation values for the annihilation operator and its square must be calculated. The Baker-Hausdorff lemma leads to the following relations [33]

$$\hat{S}^{\dagger}(\xi)\hat{a}\hat{S}(\xi) = \hat{a}\cosh(r) - \hat{a}^{\dagger}e^{i\Theta}\sinh(r),$$
$$\hat{S}^{\dagger}(\xi)\hat{a}^{\dagger}\hat{S}(\xi) = \hat{a}^{\dagger}\cosh(r) - \hat{a}e^{-i\Theta}\sinh(r), \tag{3.8}$$

where $\hat{S}^{\dagger}(\xi) = \hat{S}(-\xi)$. Considering a squeezed state

$$|\psi_s\rangle = \hat{S}(\xi)|\psi\rangle, \tag{3.9}$$

we get

$$\langle\psi_s|\,\hat{a}\,|\psi_s\rangle = \langle\psi|\,\hat{S}^{\dagger}(\xi)\hat{a}\hat{S}(\xi)\,|\psi\rangle \tag{3.10}$$

and

$$\langle\psi_s|\,\hat{a}^2\,|\psi_s\rangle = \langle\psi|\,\hat{S}^{\dagger}(\xi)\hat{a}\hat{S}(\xi)\hat{S}^{\dagger}(\xi)\hat{a}\hat{S}(\xi)\,|\psi\rangle. \tag{3.11}$$
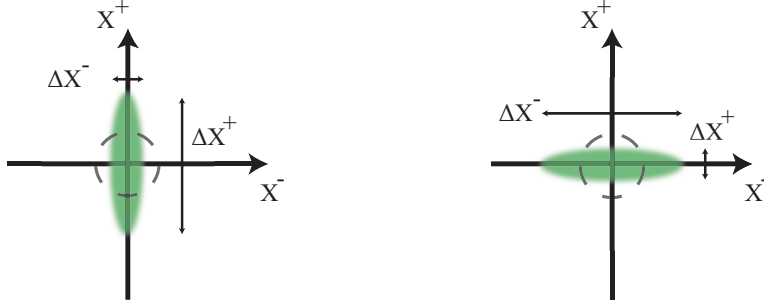
Figure 3.1: Phase-space representation of two squeezed vacuum states. The left picture shows squeezing in the $\hat{X}^+$-quadrature, where the dashed circle illustrates the uniform noise distribution of a coherent state. The second picture represents a squeezed $\hat{X}^-$-quadrature.

For these expressions, the variances of the two quadratures can be generalised to

$$\left\langle (\Delta\hat{X}^+)^2 \right\rangle = \frac{1}{4}\left(\cosh^2(r) + \sinh^2(r) - 2\sinh(r)\cosh(r)\cos(\Theta) \right),$$
$$\left\langle (\Delta\hat{X}^-)^2 \right\rangle = \frac{1}{4}\left(\cosh^2(r) + \sinh^2(r) + 2\sinh(r)\cosh(r)\cos(\Theta) \right). \quad (3.12)$$

By considering a fixed phase angle $\Theta = 0$, Eq. (3.12) can be simplified to

$$\left\langle (\Delta\hat{X}^+)^2 \right\rangle = \frac{1}{4}e^{-2r}$$
$$\left\langle (\Delta\hat{X}^-)^2 \right\rangle = \frac{1}{4}e^{2r} \quad (3.13)$$

and squeezing will be obtained for $\hat{X}^+$, whereas $\hat{X}^-$ will be antisqueezed. For a graphical illustration of squeezed states it is convenient to use the phase-space representation [34]. Fig. 3.1 shows two examples of a squeezed ground state, also known as *squeezed vacuum*, with $\Theta = 0$ and $\Theta = \pi$ and the resulting squeezing in the $\hat{X}^+$ and $\hat{X}^-$ quadratures, respectively. It is possible to define rotated quadrature operators $\hat{Y}^+$ and $\hat{Y}^-$, similar to Eq. (2.34), related to any value of the squeezing angle Θ by

$$\begin{pmatrix} \hat{Y}^+ \\ \hat{Y}^- \end{pmatrix} = \begin{pmatrix} \cos(\frac{\Theta}{2}) & \sin(\frac{\Theta}{2}) \\ -\sin(\frac{\Theta}{2}) & \cos(\frac{\Theta}{2}) \end{pmatrix} \begin{pmatrix} \hat{X}^+ \\ \hat{X}^- \end{pmatrix}. \quad (3.14)$$

21

The rotated quadrature operators satisfy

$$\left\langle (\Delta \hat{Y}^{+})^{2} \right\rangle = \frac{1}{4} e^{-2r}$$

$$\left\langle (\Delta \hat{Y}^{-})^{2} \right\rangle = \frac{1}{4} e^{2r} \tag{3.15}$$

for any squeezing angle. A general form for a coherent squeezed state, describing a squeezed field with a coherent amplitude, is given by

$$|\alpha, \xi\rangle = \hat{D}(\alpha)\hat{S}(\xi) |0\rangle, \tag{3.16}$$

and the expectation value of the number operator $|\hat{n}\rangle$ becomes

$$\langle \hat{n} \rangle = |\alpha|^{2} + \sinh^{2}(r), \tag{3.17}$$

showing that the squeezing operator creates photons. From Eq. (3.17) it is evident that squeezed vacuum has a non-zero photon number. Furthermore, the variances of a squeezed coherent state remain unchanged, as given by Eq. (3.14). The fluctuations of a squeezed state are not influenced by the displacement operator or, more precisely, by a coherent amplitude α, therefore the operators can be interchanged. Fig. 3.2 shows a squeezed ground state where the squeezing is in the rotated quadrature $\hat{Y}^{-}$ and a squeezed coherent state illustrating the states described above.

3.2 Non-Linear Optics

For the experimental realisation of squeezing a non-linear process is required. When a non-linear material is pumped with a strong field of frequency ω_p, some photons of the pump field will be converted into pairs of identical photons with frequency $\omega_p = 2\omega$, with ω denoting the frequency of the signal field. This case is called *degenerate parametric down-conversion*, and its Hamiltonian can be expressed as [33]

$$\hat{H} = \hbar\omega\hat{a}^{\dagger}\hat{a} + \hbar\omega_p\hat{b}^{\dagger}\hat{b} + i\hbar\chi^{(2)}(\hat{a}^2\hat{b}^{\dagger} - \hat{a}^{\dagger 2}\hat{b}), \tag{3.18}$$

where $\hat{a}$ and $\hat{b}$ describe the signal and the pump modes, respectively. $\chi^{(2)}$ is the second-order non-linear susceptibility and is essential for the generation of quadrature squeezing. Therefore, the $\chi^{(2)}$ non-linearity is further investigated in the following. An extensive description of non-linear optics is given in [40], which is also the source upon which the upcoming subsections are based.
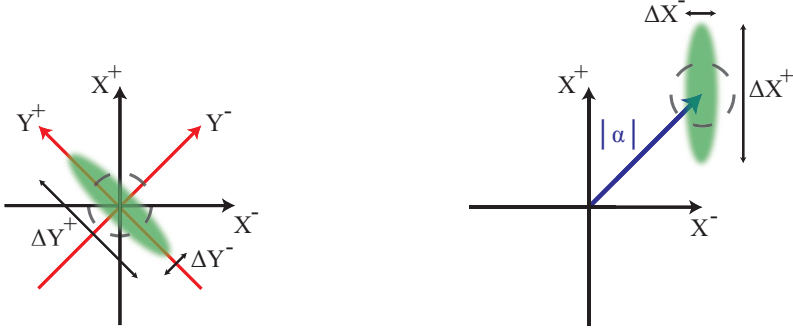
Figure 3.2: On the left a vacuum state with a squeezed quadrature $\hat{Y}^-$ is shown. The squeezing ellipse is rotated by $\Theta/2$. On the right is an illustration of a squeezed coherent state with amplitude α and a squeezed $\hat{X}^-$-quadrature.

3.2.1 Dielectric Polarisation

An electromagnetic field propagating through a dielectric medium can be viewed as a force acting on charge carriers. The separation of charges induces a dipole moment with a distinct strength given by the polarisation [40]

$$\vec{P} = \epsilon_0(\chi^{(1)}\vec{E}(t) + \chi^{(2)}\vec{E}^2(t) + \chi^{(3)}\vec{E}^3(t) + ...) = \vec{P}^{(1)} + \vec{P}^{(NL)}, \quad (3.19)$$

where $\chi^{(i)}$ are susceptibilities of the i-th order. For a single-mode field

$$E(t) = E_0 e^{-i\omega t} + \text{c.c.} \quad (3.20)$$

the second-order polarisation can be expressed as

$$P^{(2)} = 2\epsilon_0\chi^{(2)}\left(E_0 E_0^* + E_0^2 e^{-2i\omega t}\right) + \text{c.c.}. \quad (3.21)$$

Eq. (3.21) shows that the second-order polarisation yields a field component at twice the frequency of the input field. In [40] it is demonstrated on the example of the sum-frequency generation case $\omega_3 = \omega_1 + \omega_2$ that $\chi^{(2)}$ interactions can be expressed via an effective susceptibility value d_{eff}

$$P^{(2)}(w_3) = 4\epsilon_0 d_{\text{eff}} E(\omega_1) E(\omega_2). \quad (3.22)$$

Materials with a high $\chi^{(2)}$ value are within a range of $\chi^{(2)} \approx 10^{-10} - 10^{-13} \frac{\text{m}}{\text{V}}$. Since $\chi^{(1)}$ is of the order of 1 it becomes clear that the intensity of the incident field plays an important role for the generation of squeezed states.

3.2.2 Optical Parametric Conversion

For this work the $\chi^{(2)}$ interactions of interest involve three modes of light (or photons) and are described by the process of *three-wave mixing*. To be precise, the focus lies on the two cases illustrated in Fig. 3.3, known as *sum-frequency* (SFG) and *difference-frequency generation* (DFG).
For sum-frequency generation two photons with frequencies ω_1 and ω_2 are con-
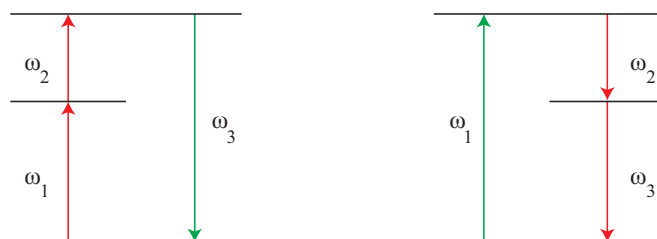
Figure 3.3: This picture shows energy-level diagrams, in which the sum-frequency generation is illustrated on the left and the difference-frequency generation on the right. ω_i denotes the interacting frequencies.

verted by a dielectric medium (e.g. a non-linear crystal) into a photon with frequency

$$\omega_3 = \omega_1 + \omega_2. \tag{3.23}$$

For $\omega_1 = \omega_2$ the special case of *second harmonic generation* (SHG) or parametric-up conversion is obtained.
Difference-frequency generation defines a $\chi^{(2)}$ interaction where a photon with ω_1 is converted into two photons with ω_2 and ω_3 which again must satisfy energy conservation, equivalent to Eq. (3.23). The case of

$$\omega_2 = \omega_3 = \frac{1}{2}\omega_1, \tag{3.24}$$

describes a special case of this, namely *parametric down-conversion*, also known as *degenerate squeezing*.
Considering DFG under appropriate phase matching conditions, by injecting a strong pump field with ω_1 and a weak field with ω_2 into a dielectric medium,

the weak field is amplified via the non-linear process. This process is called *optical parametric amplification* (OPA). Placing the dielectric medium inside a resonant optical cavity increases the strength of the non-linear process. If the amplification factor exceeds the loss factor, related to the internal optical losses of the cavity, oscillations can arise. These oscillations result in the generation of fields with ω_2 and ω_3 via a pump field at ω_1, without the need of injecting an additional weak field. This process is known as *optical parametric oscillation* (OPO). The condition where the optical losses are identical to the amplification corresponds to the OPO *threshold*. Below this threshold an OPO effectively becomes an OPA, which is the device used to generate quadrature squeezing in our laboratory. This is also denoted as a subthreshold OPO.

3.2.3 Phase Matching

Considering the SFG case for collimated, monochromatic, continuous waves the intensity of the generated field with ω_3 can be written in SI units as [40]

$$I_3 = \frac{8d_{\text{eff}}^2\omega_3^2 I_1 I_2}{n_1 n_2 n_3 \epsilon_0 c^3} L^2 \text{sinc}^2\left(\frac{\Delta kL}{2}\right), \tag{3.25}$$

where n_i are the refractive indices of the non-linear media related to the interacting fields. d_{eff} is the effective susceptibility, c the speed of light, ϵ_0 the permittivity of vacuum, $I_{1,2}$ intensity of the injected fields and L the length of the non-linear medium. An important factor affecting the intensity of the generated field and therefore the conversion efficiency is the *wavevector mismatch* Δk described by the wavevectors k_i as

$$\Delta k = k_1 + k_2 - k_3. \tag{3.26}$$

If $\Delta k = 0$ the intensity reaches its maximum. The effect of wavevector mismatch is shown in Fig. 3.4. For $\Delta k = 0$ an optimal phase matching point is achieved. The wavevector mismatch can also be expressed via the refractive indices

$$\frac{n_1\omega_1}{c} + \frac{n_2\omega_2}{c} - \frac{n_3\omega_3}{c} = 0. \tag{3.27}$$

One option to fulfil the above stated requirement makes use of the birefringence of the dielectric medium, where n is frequency- and temperature-dependent. For the case shown in Fig. 3.4 the temperature of the non-linear medium is tuned
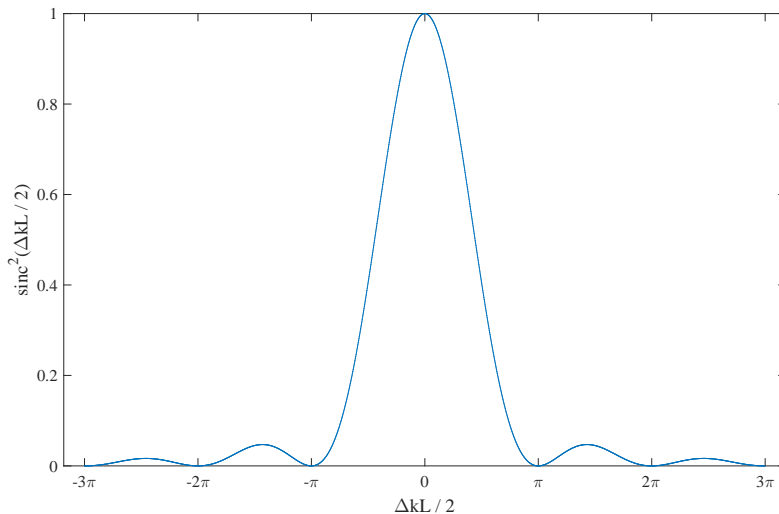
Figure 3.4: Conversion efficiency of a non-linear interaction in relation to the wavevector mismatch.

to achieve the optimal phase matching $\Delta k = 0$, where Δk can be calculated via the Sellmeier equations. The interested reader is referred to [41, 42] for more details.

Another possibility to obtain phase matching without the need for temperature tuning is known as *quasi-phase matching*. Here phase matching is realised by a periodically-poled dielectric medium; the fabrication is described in [43]. This poling causes a periodic change of the orientation of the optical axis. For each interval the ratio of the refractive indices of the pump and generated fields is inverted. By periodically varying this ratio the accumulated relative optical phase from one interval is compensated for in the following interval. To good approximation an appropriate periodicity/poling period length results in phase matching. Since this kind of phase matching only depends on the dielectric medium's grating period Λ,

$$\Delta k = \frac{n_1 \omega_1}{c} + \frac{n_2 \omega_2}{c} - \frac{n_3 \omega_3}{c} - \frac{2\pi}{\Lambda}, \tag{3.28}$$

it is possible to use materials with a higher d_{eff}, where the optimal phase matching condition cannot be achieved via temperature tuning.

The dielectric medium used for the experimental implementation of a squeezed light source in this work is periodically-poled potassium titanyl phosphate (PP-KTP).

3.2.4 Impact of Losses

After the generation of squeezed states, it is essential to avoid any optical loss channels in the experimental setup. This is a crucial point since losses irrevocably reduce the squeezing strength. Loss channels introduced by scattering and unwanted absorption can be modelled via a beamsplitter (BS) interaction. Hereby one BS port acts as an input for the squeezed state and the other describes the loss channel injecting vacuum fluctuations. Assuming the BS transfer matrix from [34], the superposition of vacuum fluctuations and squeezing can be written as

$$\left\langle (\hat{X})^2 \right\rangle_{in} = \left\langle (\hat{X})^2 \right\rangle_{out} \sqrt{\eta} + \left\langle (\hat{X})^2 \right\rangle_{vac} \sqrt{1-\eta}. \tag{3.29}$$

Here $\left\langle (\hat{X})^2 \right\rangle_i$ and $\left\langle (\hat{X})^2 \right\rangle_{vac}$ are the variances of a squeezed field and the vacuum, respectively. η is a measure for losses l and defines the reflectivity $R = l$ and the transmissivity $T = 1 - l = \eta$ of the BS. Eq. (3.29) is valid for any kind of quadrature squeezing.

In general the squeezing strength is given in Decibel (dB), where the dB value refers to a reduction of fluctuations with respect to those of a coherent state and can be expressed as

$$V[\text{dB}] = -10 \log(e^{-2r}). \tag{3.30}$$

r is the squeezing parameter introduced earlier Eq. (3.6). With Eq. (3.30) it is possible to calculate how losses affect $V[\text{dB}]$

$$V_{\text{out}}[\text{dB}] = -10 \log \left(\eta 10^{\frac{V[\text{dB}]}{10}} + (1 - \eta) \right). \tag{3.31}$$

Eq. (3.31) illustrates that strongly squeezed states are affected to a greater extent by any kind of losses than less strongly squeezed states. This impact of losses on squeezed and accordingly anti-squeezed states is illustrated in Fig. 3.5. The detection efficiency η_{tot} determines the apparent total loss factor of our experimental setup. It is given by

$$\eta_{\text{tot}} = \eta_{\text{prop}} \underbrace{\eta_{\text{PD}} \cdot \eta_{\text{vis}}}_{\text{detection losses}}, \tag{3.32}$$
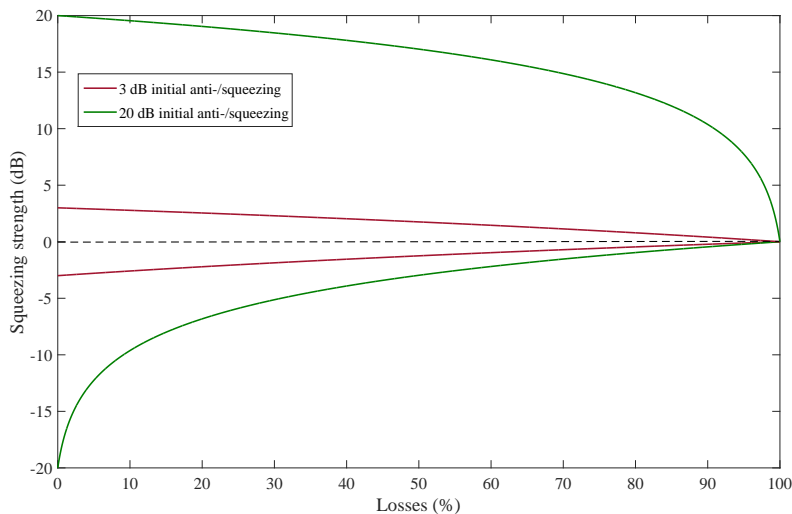
Figure 3.5: Impact of losses on the squeezing/antisqueezing strength, shown for two different initial squeezing/antisqueezing values.

where the first factor η_{prop} denotes the optical propagation loss and the two other factors η_{PD} and η_{vis} define readout losses, specifically, η_{PD} determines the quantum efficiency of the detection and η_{vis} is a measure of contrast discussed in the upcoming subsection.

3.2.5 Detection of Quadrature Squeezing

A common single photodiode (PD) [44] produces a photocurrent i proportional to the power of the incident light field and therefore also proportional to the number operator $\hat{n}$

$$i \propto \hat{a}^{\dagger}\hat{a}, \tag{3.33}$$

where $\hat{a}^{\dagger}$ and $\hat{a}$ are the annihilation and creation operators discussed in Chap. 2. Introducing the linearised form of the incident light field $\hat{A}$ from [34]

$$\hat{A} = \alpha + \delta\hat{A}(t), \tag{3.34}$$
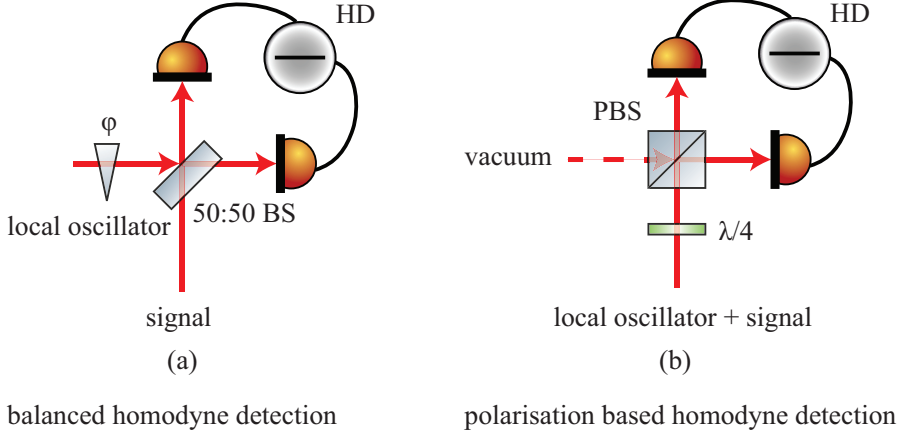
Figure 3.6: Two possible detection schemes used for the characterisation of squeezed states. ϕ denotes the phase of the local oscillator, HD is the homodyne detector, BS and PBS denote a beamsplitter and a polarising beamsplitter, respectively.

with α denoting the mean of the amplitude and $\delta\hat{A}(t)$ representing the fluctuations of the field, Eq. (3.33) becomes approximately

$$i \propto \alpha^2 + \alpha\delta\hat{X}^+. \tag{3.35}$$

Eq. (3.35) highlights that a PD is only capable of measuring power and fluctuations in the amplitude quadrature. For this reason a PD is not an appropriate device to detect arbitrarily squeezed states. For an accurate characterisation of squeezed/antisqueezed states measurements of both quadrature variances are required. The purity of a squeezed state and the detection efficiency, see Eq. (3.32), can only be determined with knowledge of both quadrature variances. One such approach that is capable of measuring both quadratures is described in [34, 45] and is referred to as *balanced homodyne detection*. A modified version of the balanced homodyne detection is the *polarisation-based homodyne detection* [46]. Both schemes are used in our laboratory and will be described in the upcoming subsections and are illustrated in Fig. 3.6.

29

Balanced Homodyne Detection

In this detection scheme a signal field $\hat{A}$ interferes on a $50:50$ BS with a strong local oscillator field $\hat{B}$ (LO). The resulting fields $\hat{C}$ and $\hat{D}$ are detected by a homodyne detector (HD) consisting of two PDs, where the photocurrents are subtracted. A perfect interference of the two fields is guaranteed if they possess the same frequency, spatial mode and polarisation. A measure of interference is given by the contrast [47] known as *fringe visibility*

$$\text{vis} = \frac{V_{\text{max}} - V_{\text{min}}}{V_{\text{max}} + V_{\text{min}}}. \tag{3.36}$$

$V_{\text{max/min}}$ determine the maximal and minimal output voltages of a PD, while the relative phase between signal and LO is tuned periodically. Furthermore the fringe visibility defines the loss channel η_{vis} mentioned above in Eq. (3.32) as follows

$$\eta_{\text{vis}} = \text{vis}^2. \tag{3.37}$$

Assuming the case of lossless detection this scheme can be modelled as follows. Using the beamsplitter matrix defined in [34] with the matched amplitude transmission and reflection coefficients t and r for a $50:50$ beamsplitter leads to

$$
\begin{pmatrix} \hat{C} \\ \hat{D} \end{pmatrix} = \begin{pmatrix} t & r \\ r & -t \end{pmatrix} \begin{pmatrix} \hat{A} \\ \hat{B} \end{pmatrix}
$$
$$
= \frac{1}{\sqrt{2}} \begin{pmatrix} 1 & 1 \\ 1 & -1 \end{pmatrix} \begin{pmatrix} \hat{A} \\ \hat{B} \end{pmatrix}. \tag{3.38}
$$

Hence, the output fields are given by

$$\hat{C} = \frac{1}{\sqrt{2}}(\hat{A} + \hat{B}) \qquad \text{and} \qquad \hat{D} = \frac{1}{\sqrt{2}}(\hat{A} - \hat{B}). \tag{3.39}$$

The measured signals of the two output ports can be calculated with $\hat{A}$ and $\hat{B}$ written in the linearised form

$$\hat{A} = \alpha + \delta\hat{A} \tag{3.40}$$
$$\hat{B} = (\beta + \delta\hat{B})e^{-i\phi}, \tag{3.41}$$

where $e^{-i\phi}$ defines the relative phase between the signal and LO fields and the knowledge that $i \propto \hat{n}$. These assumptions lead to

$$
\begin{aligned}
\hat{i}_c \propto \hat{C}^\dagger \hat{C} = \frac{1}{2}\Big[&\alpha^2 + \beta^2 + 2\alpha\beta\cos(\phi) \\
&+ 2\alpha\left(\delta\hat{X}_A^+ + \cos(\phi)\delta\hat{X}_B^+ - \sin(\phi)\delta\hat{X}_B^-\right) \\
&+ 2\beta\left(\delta\hat{X}_A^+ + \cos(\phi)\delta\hat{X}_A^+ + \sin(\phi)\delta\hat{X}_A^-\right)\Big] + \mathcal{O}(\delta^2)
\end{aligned}
\tag{3.42}
$$

and

$$
\begin{aligned}
\hat{i}_d \propto \hat{D}^\dagger \hat{D} = \frac{1}{2}\Big[&\alpha^2 + \beta^2 - 2\alpha\beta\cos(\phi) \\
&- 2\alpha\left(\cos(\phi)\delta\hat{X}_B^+ - \sin(\phi)\delta\hat{X}_B^- - \delta\hat{X}_A^+\right) \\
&- 2\beta\left(\cos(\phi)\delta\hat{X}_A^+ + \sin(\phi)\delta\hat{X}_A^- - \delta\hat{X}_B^-\right)\Big] + \mathcal{O}(\delta^2).
\end{aligned}
\tag{3.43}
$$

Taking the following relations for an arbitrary operator $\hat{\varphi}$ into account

$$
\begin{aligned}
\delta\hat{\varphi} + \delta\hat{\varphi}^\dagger &= \delta\hat{X}_\varphi^+ \\
i(\delta\hat{\varphi} - \delta\hat{\varphi}^\dagger) &= \delta\hat{X}_\varphi^- \\
\delta\hat{\varphi}e^{\pm i\phi} + \delta\hat{\varphi}^\dagger e^{\mp i\phi} &= \delta\hat{X}_\varphi^\phi
\end{aligned}
\tag{3.44}
$$

and considering that the local oscillator field is much stronger than the signal field

$$
|\beta|^2 \gg |\alpha|^2 \,,
\tag{3.45}
$$

the difference between the two detected photocurrents is approximately

$$
\begin{aligned}
i_- \propto i_c - i_d &\propto \beta\left(\cos(\phi)\delta\hat{X}_A^+ + \sin(\phi)\hat{X}_A^-\right) \\
&\propto \beta\delta\hat{X}_A^\phi.
\end{aligned}
\tag{3.46}
$$

Thus, the fluctuations of the $\hat{X}^\phi$ quadrature are amplified by the mean field amplitude of the LO. The detection angle ϕ determining the observed quadrature can be addressed with a phase shifter, see Fig. 3.6a. The variance of the signal field

$$
V(i_-) \propto \beta^2 V(\hat{X}_A^\phi)
\tag{3.47}
$$

is measured with a spectrum analyser and converted into the frequency domain via a Fast Fourier Transform (FFT).

Polarisation-Based Homodyne Detection

In this scheme [46] the signal and LO fields are co-propagating. The signal and LO fields have identical frequencies and spatial modes but differ in their polarisations. More precisely the polarisations of the fields are perpendicular to each other. An advantage of this scheme is that co-propagating fields from one source intrinsically show a vis $= 1$. The combination of a BS and an external LO is replaced by a $\lambda/4$-waveplate, a polarising beamsplitter (PBS) and a co-propagating LO. The mathematical model of this rearranged scheme is similar to the balanced homodyne detector case. Eq. (3.38) is extended by the Jones calculus [48] for a quarter-waveplate

$$\begin{pmatrix} \hat{C} \\ \hat{D} \end{pmatrix} = \frac{1}{\sqrt{2}} \begin{pmatrix} e^{i\frac{\pi}{4}} & 0 \\ 0 & e^{-i\frac{\pi}{4}} \end{pmatrix} \frac{1}{\sqrt{2}} \begin{pmatrix} 1 & 1 \\ 1 & -1 \end{pmatrix} \begin{pmatrix} \hat{A} \\ \hat{B} \end{pmatrix}. \tag{3.48}$$

The waveplate allows for interference of the signal and LO fields, previously orthogonally polarised to each other. Furthermore the waveplate introduces a phase difference of $\pi/2$ between the interacting fields. Consequently this scheme is only capable of reading out the phase quadrature $\hat{X}_A^-$ of the signal field.

This setup is also suitable for additional spectroscopy measurements. If the signal field interacts with a phase-sensitive object, it obtains a phase-shift with respect to the LO. The signal field is now given by

$$\hat{A} = \alpha + \delta\hat{A}e^{i\Delta\psi} \tag{3.49}$$

and the detected signal at the HD output becomes

$$i_- = -2\alpha\beta\sin(\Delta\psi) + \beta\delta\hat{X}_A^-. \tag{3.50}$$

Since an optical cavity is a phase-sensitive device, this scheme can be used to generate an error signal used to stabilise its length [46].

The polarisation-based homodyne detection can also be realised with an external LO. In this case the LO and signal fields are not co-propagating all the time, which leads to the advantage that the HD output can look at both quadratures. A disadvantage is that the beneficial common-mode rejection of disturbances does not occur in this case. An additional downside is that the intrinsic fringe visibility vis $= 1$ is not guaranteed anymore. We implemented and investigated both polarisation-based homodyne detection setups in our laboratory.

Basics of Optical Cavities

In this chapter the fundamentals of optical cavities are discussed following the descriptions presented in [49, 50]. These basics shall provide the characteristic dynamics of optical cavities and an explanation for the commonly required length control, which is experimentally implemented and characterised in Chap. 6.

4.1 Field Amplitudes of a Fabry-Pérot Resonator

A linear optical cavity, known as *Fabry-Pérot resonator*, is used as an example to introduce the important properties of optical cavities. It consists of two mirrors $M1$ and $M2$ with corresponding amplitude reflection and transmission coefficients $r_{1,2}$ and $t_{1,2}$, respectively. The amplitude coefficients are related to optical losses l caused by scattering or absorption via

$$r_i^2 + t_i^2 + l = 1, \tag{4.1}$$

where $r_i^2 = R$ and $t_i^2 = T$ are the power reflection and transmission coefficients. For the description of light fields interacting with optical surfaces and propagating through vacuum/air, the notation given in [49] is used. The light fields interacting with a cavity are defined by their parameters r_i, t_i corresponding to the mirror M_i and its length L. A schematic of a Fabry-Pérot resonator with light fields a_i is shown in Fig. 4.1. The field amplitudes in vacuum for plane waves
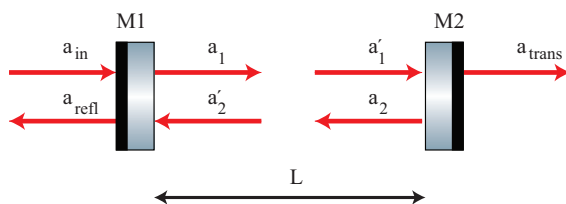
Figure 4.1: Schematic of a two mirror linear cavity with amplitude reflection and transmission coefficients r_i and t_i corresponding to mirror M_i. The cavity has a length L and the light field amplitudes are given by a_i.

can be expressed as follows

$$a_1 = r_1 a_2' + it a_{in},$$
$$a_{refl} = r a_{in} + it a_2',$$
$$a_1' = a_1 e^{-ikL},$$
$$a_{trans} = it_2 a_1',$$
$$a_2 = r_2 a_1',$$
$$a_2' = a_2 e^{-ikL}. \tag{4.2}$$

By substituting one equation into the other the amplitudes of the reflected, transmitted and circulating fields are derived. The circulating field amplitude after one round trip is given by

$$a_2' = a_{in} \frac{i r_2 t_1 e^{-2ikL}}{1 - r_1 r_2 e^{-2ikL}}. \tag{4.3}$$

The reflected field amplitude becomes

$$a_{ref} = a_{in} \frac{r_1 - r_2(r_1^2 + t_1^2)e^{-2ikL}}{1 - r_1 r_2 e^{-2ikL}} \tag{4.4}$$

and the transmitted field amplitude is

$$a_{trans} = a_{in} \frac{-t_1 t_2 e^{-2ikL}}{1 - r_1 r_2 e^{-2ikL}}. \tag{4.5}$$

Another more convenient way to compute the dynamics of optical cavities or more complex systems is given by applying coupling matrices, which are able to

describe every single part of the optical assembly. Hence, the behaviour of the system is given by the product of the associated matrices. The interested reader is referred to [49, 50] for a more complete treatment.

4.2 Characteristic Values of Optical Cavities

After deriving the field amplitudes important characteristics of optical cavities can be determined. The performance of the optical cavity depends on its length L, the wavelength λ and the amplitude reflection and transmission coefficients r_i and t_i.

The frequency-dependent transmission transfer function of a Fabry-Pérot resonator is given by an Airy function

$$\frac{a_{trans}}{a_{in}} = \frac{-t_1 t_2 e^{-2ikL}}{1 - r_1 r_2 e^{-2ikL}}, \tag{4.6}$$

where $k = 2\pi f / c$ is the wavevector, c is the speed of light and f the frequency of the light.

Eq. (4.6) reaches its maximum when the cosine of the exponential function in the denominator becomes one. This is the case for

$$\frac{2\pi f L}{c} = N\pi \quad \text{or} \quad L = N\frac{\lambda}{2}, \tag{4.7}$$

where N is a positive integer. This maximal transmittance defines the *resonance* condition for an optical cavity. From Eq. (4.7) it is evident why cavity length control is needed. External disturbances affecting the length of the optical cavity or frequency fluctuations of the incident light field [51] are the reason why the resonance condition is not permanently satisfied. To keep the system on resonance a controller is needed to compensate for these effects.

The frequency difference between two adjacent resonance conditions is defined as the *free spectral range* (FSR)

$$\text{FSR} = \frac{c}{2L}. \tag{4.8}$$

The resonance of an optical cavity has a certain linewidth $\Delta\nu$, it is usually given as full width half maximum (FWHM). It describes the lifetime of photons inside

an optical cavity. This photon lifetime is known as *cavity decay rate* κ and depends on the reflectivity r_i of the mirrors, losses l, c the speed of light and the cavity length L. κ is defined as [34, 50]

$$\kappa = -\frac{c \ln \left[r_1^2 r_2^2 \left(1 - l \right) \right]}{4L}. \tag{4.9}$$

The relation between the linewidth and the photon lifetime is

$$\kappa = 2\pi \Delta\nu. \tag{4.10}$$

Furthermore the ratio of FSR and linewidth defines the *finesse* $\mathcal{F}$, a commonly utilised quality measure of a resonant system

$$\mathcal{F} = \frac{\text{FSR}}{\Delta\nu}. \tag{4.11}$$

This Q-factor $\mathcal{F}$ can also be expressed via the reflectivity of the mirrors [49]

$$\mathcal{F} = \frac{\pi}{2 \arcsin \left(\frac{1 - r_1 r_2}{2\sqrt{r_1 r_2}} \right)}. \tag{4.12}$$

For the high finesse scenario the argument of the arcsin function becomes small, which allows for the approximation

$$\mathcal{F} \approx \frac{\pi \sqrt{r_1 r_2}}{1 - r_1 r_2}. \tag{4.13}$$

The frequency-dependent transmitted power of an optical cavity and the associated parameters $\Delta\nu$ and FSR are illustrated in Fig. 4.2.

4.3 Error Signal

For the example of locking the length of an optical cavity to the frequency of an incident laser an error signal is needed to keep the system on resonance. The error signal determines the discrepancy from the reference point of the system. Here the reference point is given by the resonance condition of the optical cavity and the discrepancy is determined by the detuning Δ

$$\Delta = f_c - f_L = \frac{c}{nL} - f_L, \tag{4.14}$$
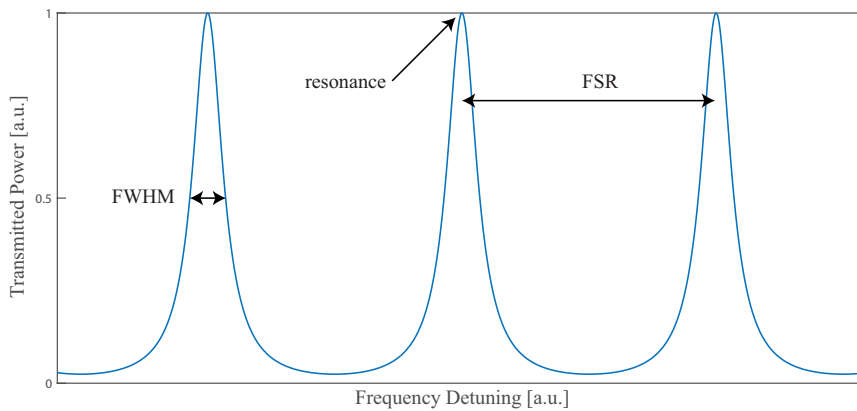
Figure 4.2: Frequency-dependent transmitted power of a Fabry-Pérot resonator. The maxima correspond to the resonances of the optical system. The FSR defines the frequency separation of two adjacent resonances associated with a single fundamental mode, and the linewidth $\Delta\nu$ of the optical cavity can be given in FWHM.
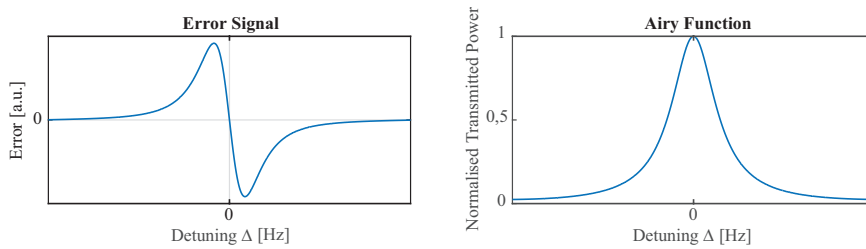
Figure 4.3: Illustration of an appropriate error signal in dependence on the detuning Δ and the corresponding transmitted power.

with f_c the resonance of the cavity, f_L the laser frequency, c the speed of light n the index of refraction and L the cavity length. From Eq. (4.14) it can be seen that the error signal is linear around the reference point and switches its sign on resonance. Why the linearity of the error signal plays an important role is discussed in Chap. 5. The mentioned requirement on the error signal leads to the question: how can an appropriate error signal for cavity frequency be generated? The transmitted power cannot be used as a suitable error signal, since a specific power, away from resonance, does not provide a unique solution for the detuning. Hence, the sign of the corresponding error signal is not well defined (for a detuned cavity lock the transmitted power can be used as error signal. This detuned case is known as *midfringe locking* [52]). However, the derivative of the Airy function describing the gradient of the transmitted power yields an appropriate error signal. The transmitted power and its derivative, which is a suitable error signal, are shown in Fig. 4.3. An experimental generation of such an error signal can be achieved by utilising a modulation/demodulation scheme with subsequent low-pass filtering. A well-known modulation scheme for cavity locking is described in [53] and called *Pound-Drever-Hall* (PDH) technique. Other typical techniques yielding error signals useful for cavity locking are tilt locking [54], Hänsch-Couillaud locking [55] or homodyne locking [46]. An advantage of these techniques is the lack of modulation, thereby avoiding additional noise channels. Tilt locking generates an error signal via the interference signal of the carrier with a non-resonant spatial mode. Hänsch-Couillaud and homodyne locking perform polarisation spectroscopy of an optical cavity, where the relative phase between the resonant and non-resonant polarisation is read out by a polarisation-based homodyne detection scheme, see Chap. 3.

The phase response of an optical cavity is affected by the reflectivity of its mirrors. The impedance of the cavity describes this effect.

4.4 Cavity Impedance

There are three possible impedance scenarios for a Fabry-Pérot resonator. All described cases assume a lossless setup and are defined via the power reflectivity of the mirrors $T_i = t_i^2$.

- Impedance-matched cavity: $T_1 = T_2$
  On resonance the light field in reflection of the Fabry-Pérot resonator vanishes and the transmitted power reaches its maximum. More precisely the transmitted power is equal to the power of the incoming light field. On resonance the intracavity field is enhanced, with respect to the incoming light field.

- Overcoupled cavity: $T_1 > T_2$
  On resonance the power of the reflected field reaches its minimum, but it is still stronger than the power of the transmitted field. The circulating power inside the resonator is significantly enhanced with respect to the power of the incoming field.

- Undercoupled cavity: $T_1 < T_2$
  On resonance the ratio of reflected to transmitted field power is comparable to the overcoupled case, but this time the circulating field is not enhanced with respect to the power of the incoming field. Also noteworthy is the fact that the phase response of the reflected field is almost a constant.

The undercoupled case highlights the importance of a well-defined impedance, since a Hänsch-Couillaud or polarisation-based homodyne lock, which are applied techniques in our laboratory, in reflection of an undercoupled optical cavity does not provide a suitable locking scheme, due to near-constant phase response. For a system which exhibits losses l the coupling conditions can be extended. For example the impedance matched case becomes $T_1 = T_2 l$ and the power transmission T_1 matches the power reduction obtained in one cavity round-trip. These scenarios are discussed in more detail and illustrated in [49].

4.5 Stability Criterion

Laser used for most metrology purposes emit a transverse Gaussian (TEM_{00}) mode. In order to determine if an optical cavity is stable, it is useful to define a measure, which describes how well the Gaussian beam inside the optical cavity reproduces itself after reflection on the mirrors. The properties affecting the self reproduction are the mirrors' radii of curvature (ROC) and the length L of the optical cavity, which are further used to formulate a stability criterion via the ray transfer matrix analysis introduced in [56]

$$0 \leq \underbrace{\left(1 - \frac{L}{ROC_1}\right)}_{g_1} \underbrace{\left(1 - \frac{L}{ROC_2}\right)}_{g_2} \leq 1. \qquad (4.15)$$

The parameter space of Eq. (4.15) provides a range of stable combination possibilities, which result in various optical cavity layouts, see Fig. 4.4 [56].

 The ray transfer matrix analysis describes how a Gaussian beam is transformed by optical components and hence it can be used to match the spatial and phase profile of a beam to the resonant mode of a stable optical cavity. This process is referred to as *mode matching*.
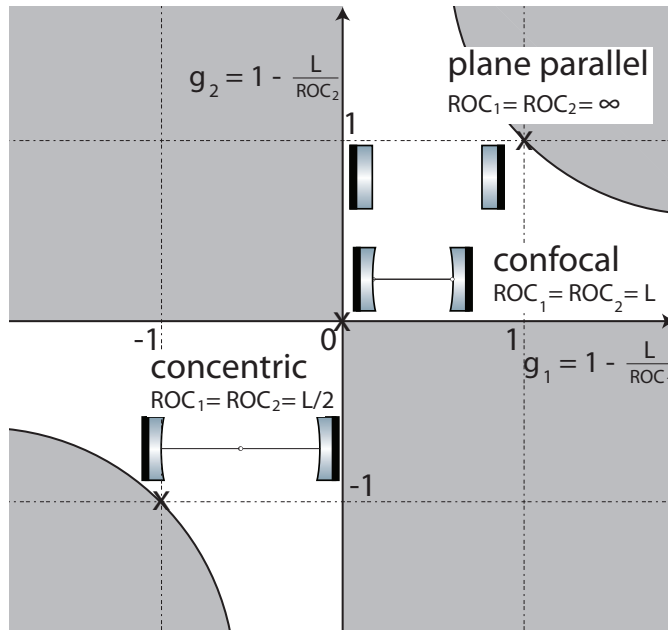
Figure 4.4: Stability diagram for various cavity configurations. The coordinate axes are given by g_1 and g_2. Configurations satisfying Eq. (4.15) are bounded to the white areas.

<div style="text-align: right">**5**</div>

Control Theory

The design of feedback controllers is essential for a wide range of optical experiments. For example continuous-wave laser sources require feedback control to obtain a constant output field [57]; cavity locking and squeezing experiments are also dependent on feedback control [58]. Without the implementation of suitable control schemes high performance operation cannot be achieved. Since many optics experiments are affected by external disturbances, such as variations in temperature and acoustic disturbances, it is often also expected that the controller should suppress external disturbances to ensure long-term operation. In complex systems it can be phenomenally difficult to manually design feedback controllers, particularly in the multiple-input multiple-output case. Modern controller synthesis techniques utilize system models and sophisticated algorithms to handle this complexity. A systematic control approach may be beneficial not only because it simplifies the controller design process, but also because it can produce optimal controllers. Since the focus of this work lies on the implementation of model-based controllers a fundamental understanding of system and control theory is required and is introduced in this chapter.

5.1 Signals and Systems

All physical systems are non-linear. However, many systems can be well approximated by linear, time-invariant models around a certain operating point. Non-linear systems are in general computationally and conceptually difficult to

control [59]. Therefore if a system can be linearised this simplifies its characterisation and the design of an appropriate feedback controller. The systems utilized in this work can often be well described by *linear time-invariant* (LTI) models and these are considered in the remainder of this thesis. LTI systems satisfy the principles of superposition and homogeneity [60].

A system satisfies the principle of superposition if the input signals $x_i(t)$ can be transformed into output signals $y_i(t)$ in the following way

$$
\begin{aligned}
x_1(t) &\Rightarrow y_1(t), \\
x_2(t) &\Rightarrow y_2(t), \\
x_1(t) + x_2(t) &\Rightarrow y_1(t) + y_2(t).
\end{aligned}
\tag{5.1}
$$

The principle of homogeneity is described in a similar fashion. Here an excitation $x_i(t)$ multiplied by a constant factor γ leads to an output signal $y_i(t)$ also multiplied by γ

$$
\gamma x_i(t) \Rightarrow \gamma y_i(t).
\tag{5.2}
$$

If these characteristics are constant over time, the system is LTI.

The time evolution of a system G_1, see Fig. 5.1, is determined by the convolution integral

$$
y_1(t) = \int_0^t g_1(t - \tau) x_1(\tau) d\tau,
\tag{5.3}
$$

where $x_1(t)$ is the input signal and $y_1(t)$ denotes the system output defined for $t \in [0, \infty)$. $g_1(t)$ is the impulse response of the system; its Laplace transform $G_1(s)$ is the transfer function of the system. An illustration of the signal flow is usually shown in a *block diagram* [59, 60], see Fig. 5.1. In control theory, the system of interest is often referred to as the *plant*. It is convenient to convert Eq. (5.3) into the frequency domain via the Laplace transform

$$
F(s) = \int_0^\infty f(t) e^{-st} dt,
\tag{5.4}
$$

where $F(s)$ is the Laplace transform of $f(t)$.

In the frequency domain Eq. (5.3) becomes

$$
Y_1(s) = G_1(s) X_1(s),
\tag{5.5}
$$

where $s = \sigma + i\omega$ is the complex angular frequency, and $X_1(s)$ and $Y_1(s)$ are the input and output of the system in the frequency domain, respectively. Eq. (5.5)
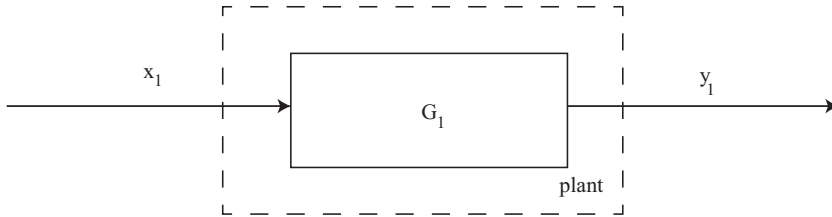
Figure 5.1: Block diagram of a system G_1 and its associated input x_1 and output y_1.

highlights the convenience of working in the frequency domain; the convolution integrals in the time domain simplify to algebraic manipulation in the frequency domain. Furthermore it can be seen that a transfer function is defined as the ratio of the output to input in the frequency domain. The transfer function of a system consisting of two systems G_1 and G_2 connected in series can be determined by taking into account that the output of the first system $Y_1(s)$ is the input of the second one: $Y_2(s) = G_2(s)Y_1(s)$. Substituting $Y_1(s)$ from Eq. 5.5 leads to $Y_2(s) = G_2(s)G_1(s)X_1(s)$. The transfer function of the overall system $G_{total}(s)$ can be expressed as

$$G_{total}(s) = G_1(s)G_2(s) = \frac{Y_2(s)}{X_1(s)}. \tag{5.6}$$

This form can be expanded to n cascaded subsystems, where the transfer function $G_{total}(s)$ completely characterises the overall system [61]

$$G_{total}(s) = \prod_{i=1}^{n} G_i(s). \tag{5.7}$$

Analogously n systems in parallel can be described by

$$G_{total}(s) = \sum_{i=1}^{n} G_i(s). \tag{5.8}$$

5.2 System Stability

An important property of a system is its stability. There are numerous definitions for stability in control theory, including Lyapunov stability, asymptotic stability, bounded-input bounded-output stability. We consider exponential stability for LTI systems in the following. An exponentially stable LTI system will never produce an unbounded output.

A transfer function $G(s)$ can always be expressed in the following form [62]

$$G(s) = \frac{N(s)}{D(s)} = K\frac{(s - z_1)(s - z_2)...(s - z_{m-1})(s - z_m)}{(s - p_1)(s - p_2)...(s - p_{n-1})(s - p_n)}, \quad m \leq n, \quad (5.9)$$

where z_i, the system *zeros*, are the roots of the equation

$$N(s) = 0, \tag{5.10}$$

and p_i, the system *poles*, are the roots of the equation

$$D(s) = 0. \tag{5.11}$$

The system poles define the modes of the plant. The zeros of the system essentially determine how the modes of the system are combined to generate the system response. The location of the sensors/actuators affect the system zeros and therefore the overall input/output response of the system. The combination of the poles and zeros define the system dynamics. The time evolution of a LTI system can be expressed as [62]

$$y(t) = \sum_{i=1}^{n} c_i e^{p_i t}, \tag{5.12}$$

where p_i are the system poles and c_i are the weighting factors for each mode, which depend upon the system zeros. From Eq. (5.12) it can be seen that when the system poles p_i are in the right half plane, the response goes to infinity. As a result, the system is termed unstable. Since $D(s)$ is real, all poles must either be real or appear in complex conjugate pairs. Taking this into account Eq. (5.12) leads to the fact that real negative poles describe an exponentially decaying component in the transient response and complex conjugate pole pairs of the form $p_i = -\sigma \pm i\omega$ describe an exponentially-decaying sinusoidal component. Noteworthy are the marginally stable cases, where a pole is at the origin or a complex
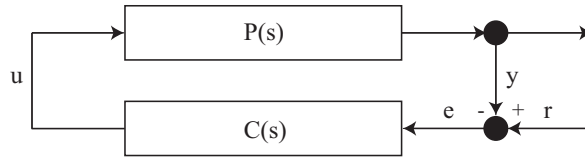
Figure 5.2: Block diagram of a feedback control loop consisting of a controller and a plant with transfer functions $C(s)$ and $P(s)$, respectively. y is the output of the plant, r a reference signal, e the error signal and u is the controller output.

pole pair is located on the imaginary axis, resulting in an integrator or a perfect oscillator, respectively. A more in-depth review of these cases can be found in [63].

5.3 Feedback Control

The goal of many control loops is to keep the plant at a desired operating point r. An exemplary control loop is represented as a block diagram in Fig. 5.2. The control loop consists of a plant $P(s)$ and a controller $C(s)$. The goal of the feedback loop is to control the plant in a way such that its output y tracks the defined reference r. In the frequency domain, the output $Y(s)$ is given by

$$Y(s) = P(s)U(s), \tag{5.13}$$

where $U(s)$ is the controller output. Since the output of the system is used for control this scheme is known as *output feedback*. The deviation between y and r due to external disturbances determines the error signal e which, in the frequency domain, is the controller input

$$e = y - r. \tag{5.14}$$

Ideally the controller converts the error signal into an output signal u which counteracts the disturbances and enforces $e = 0$. A classical example for a controller capable of driving the error signal to zero is a *proportional integral*
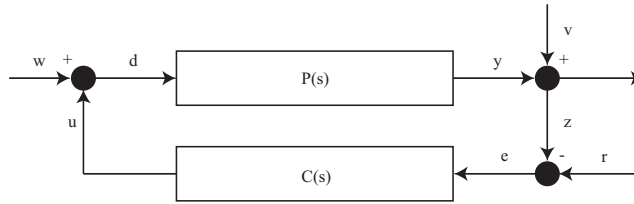
Figure 5.3: Modified block diagram with additional noise inputs. w denotes an input disturbance to the plant, whereas v defines the sensor noise.

(PI) controller, consisting of a proportional gain and an integrator. A PI controller can be expressed in the frequency domain as

$$C(s) = K_p + K_i \frac{1}{s},$$

(5.15)

where the controller is defined by two tunable variables K_p the proportional gain and K_i the integral gain of the controller.

Fig. 5.3 illustrates a slightly modified block diagram of the control loop including a port for an input disturbance w acting on the plant and a port for sensor noise v that corrupts the readout. The input and output of the plant become $d = u + w$ and $z = y + v$, respectively. A feedback loop in general is fully characterised by considering the input/output responses from all inputs (including disturbances) to all outputs. It turns out that a set of four transfer functions completely describes the performance of the feedback loop. The derivation of one of these closed-loop transfer functions, simply from the plant input to its output, is included here. Adhering to the mathematical description introduced in Sec. 5.1 and the notation from Fig. 5.2 we obtain

$$
\begin{aligned}
Y(s) &= P(s)C(s)E(s), \\
E(s) &= R(s) - P(s)C(s)E(s), \\
R(s) &= E(s) + P(s)C(s)E(s), \\
\frac{Y(s)}{R(s)} &= \frac{P(s)C(s)E(s)}{E(s) + P(s)C(s)E(s)} \\
&= \frac{P(s)C(s)}{1 + P(s)C(s)}.
\end{aligned}
$$

(5.16)

The remaining transfer functions are calculated in a similar fashion. The complete set is

$$\frac{PC}{1+PC}, \quad \frac{1}{1+PC}, \quad \frac{P}{1+PC}, \quad \frac{C}{1+PC}. \tag{5.17}$$

The first two transfer functions are particularly important as they describe the tracking performance and disturbance rejection performance, respectively; they are the *complementary sensitivity function* (T) and the *sensitivity function* (S). It is worth mentioning that

$$T + S = 1, \tag{5.18}$$

which emphasises that compromises must be made in feedback control, since it is not possible to independently define S and T. Fortunately the requirements for S and T are usually complementary for good performance. Usually S is small in the bandwidth of interest, which reduces the effects of output disturbances, and therefore $T \approx 1$ which ensures good tracking performance. T rolls off at high frequencies, usually outside the bandwidth of interest, where sensor noise becomes more significant and $S \approx 1$ [60]. The third transfer function captures the effect of an input disturbance w and is called the *load disturbance sensitivity function*. The fourth transfer function determines the effect of measurement noise v and is known as the *noise sensitivity function*.

A simple example demonstrates why it is necessary to examine the set of transfer functions in Eq. (5.17). Considering an example [64] comparable to Fig. 5.3 highlights that examination of only S and T (as is commonly done) is inadequate in completely describing the response of the closed-loop system. P and C are given by

$$P(s) = \frac{1}{(s+0.02)(s+1)} \quad \text{and} \quad C(s) = \frac{s+0.02}{s} \tag{5.19}$$

and the four transfer functions describing the closed-loop system are

$$T = \frac{1}{s^2 + s + 1} \qquad \frac{P}{1+PC} = \frac{s}{(s+0.02)(s^2+s+1)}$$

$$S = \frac{s(s+1)}{s^2+s+1} \qquad \frac{C}{1+PC} = \frac{(s+0.02)(s+1)}{s^2+s+1}, \tag{5.20}$$

whose step responses are shown in Fig. 5.4. Here it can be seen that a a disturbance at the plant input has severe effects on the transient performance. The reason for the impractically large settling time is the low-frequency pole, which is
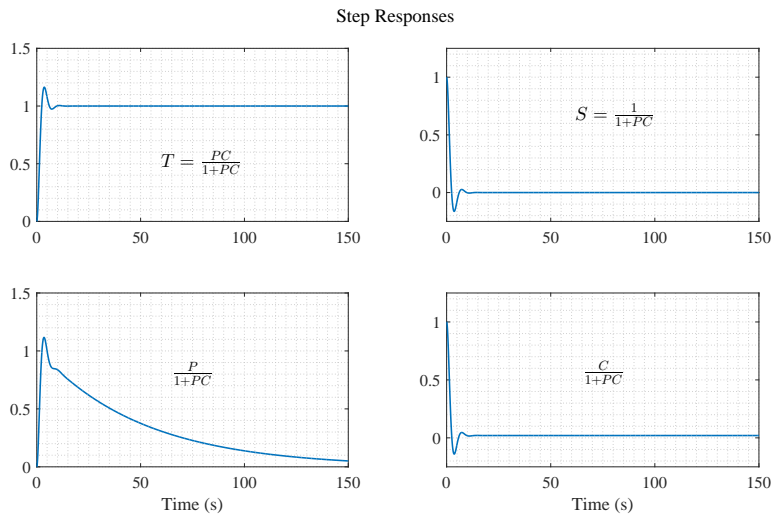
Step Responses

Figure 5.4: The performance of the closed-loop system can be characterised by the step responses of the set of four transfer functions. In this case the set of four transfer functions represents the dynamics of a plant $P = \frac{1}{(s+0.02)(s+1)}$ and a PI controller $C = \frac{s+0.02}{s}$.

not cancelled by the controller. Such examples highlight the importance of fully characterising the feedback loop and not just examining the transfer function of interest. The stability of a closed-loop system is also crucial. The feedback connection of two stable systems can produce an unstable system and improperly designed feedback controllers can and do result in unstable closed-loop systems. To examine the stability of the closed-loop system we must examine the location of the poles by solving $1 + PC = 0$. Another useful concept is the idea of the stability margins: how far is the system from instability? In practical settings knowledge of the gain and phase margins, which are related to Bode plots of the open-loop system, is often useful. Bode plots will be often used throughout this thesis and illustrate the frequency-dependent behaviour of measured transfer functions. They consist of two plots: the gain of the system in dB and the phase in degrees. According to [62] the gain and phase margins of a closed loop transfer function $H(s)$ are defined as:

- The gain margin is equal to $g_m = -20 \log_{10} |H(i\omega_1)|$, where $\omega_1 = 2\pi f_1$ and f_1 corresponds to the phase $\phi = -180°$. If the overall gain is larger than the unity gain (0 dB) at f_1 the system is unstable. The gain margin highlights how much the gain must increase before the system becomes unstable. As a rule of thumb a gain margin of 6 dB or more is desirable.

- The phase margin in degree is given by $\phi_m = 180 + \phi(f_0)$, where f_0 refers to the unity gain frequency. A negative phase margin is related to an unstable closed-loop system. As a rule of thumb a phase margin of 60° or more is desirable in practice.

The example from Eq. (5.20) highlights the importance of a thoughtful controller design process. Usually in physics the controllers are designed by ad hoc methods, focusing on loop shaping via tuning of electronic circuits. This ad hoc approach works well for simple systems, but with an increased system complexity the controller implementation becomes very challenging. The reasons for this are often due to cross-coupling between inputs and outputs whose effects can not always be intuitively accounted for.

One possible approach to control highly complex systems is the use of modern control techniques. These systematic techniques require accurate system models that account for the dynamics and cross-couplings between inputs and outputs. This work is primarily concerned with the application of modern control techniques to experiments in quantum optics.

5.4 State-Space Control

To consider modern control techniques, it is necessary to introduce state-space models. All LTI systems can be described via a *state-space model*, which has the form

$$\dot{x} = Ax + Bu, \tag{5.21}$$

$$y = Cx + Du, \tag{5.22}$$

where $x_k \in \mathbb{R}^n$ is the state vector, $u_k \in \mathbb{R}^m$ is the input vector and $y_k \in \mathbb{R}^p$ is the output vector at time instant k. The matrix $A \in \mathbb{R}^{n \times n}$ is called the system or state matrix and it represents the system dynamics. The input matrix $B \in \mathbb{R}^{n \times m}$ describes how the inputs affect the time-evolution of the system and the output
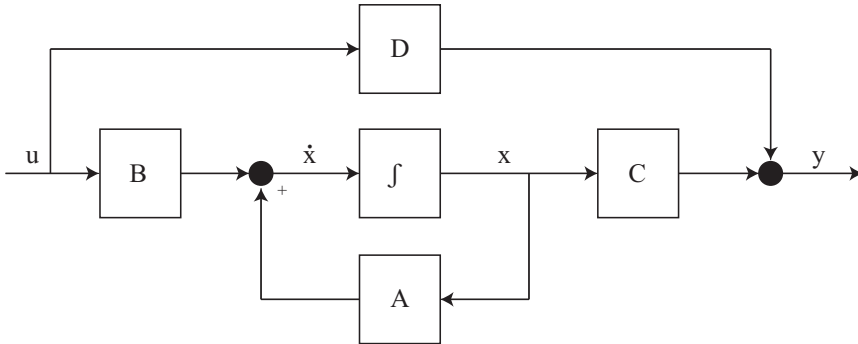
Figure 5.5: The block diagram presents a LTI system in its state-space form.

matrix $C \in \mathbb{R}^{p \times n}$ describes how the measured outputs depend on the system states. The matrix $D \in \mathbb{R}^{p \times m}$ represents a direct feedthrough from the input to the output. Fig. 5.5 illustrates a block diagram of a LTI system in state-space form. The internal state x is sufficient to describe the complete system. For a LTI system there exists a set of matrices $\{A, B, C, D\}$ that generates the same input/output response as the transfer function $G(s)$. The conversion of the state-space representation into a transfer function can be highlighted by application of the Laplace transform [61]

$$sX(s) = AX(s) + BU(s)$$
$$Y(s) = CX(s) + DU(s)$$

$$(sI - A)X(s) = BU(s)$$
$$X(s) = (sI - A)^{-1}BU(s)$$
$$Y(s) = C(sI - A)^{-1}BU(s) + DU(s)$$

$$G(s) = \frac{Y(s)}{U(s)}$$
$$= C(sI - A)^{-1}B + D. \tag{5.23}$$

It is also important to mention that state-space models are not unique. In fact, there are an infinite number of state-space models, which could describe a given input/output response. Some *system identification* methods, known as subspace identification, can convert measured data directly into a state-space model for the purposes of system analysis and control.

Stability analysis of a state-space model highlights interesting relations between the A matrix and the system poles p_i: the system poles are the eigenvalues of the A matrix.

The time evolution of a state-space model is given by

$$x(t) = e^{At}x_0 + \int_0^t e^{A(t-\tau)}Bu(\tau)d\tau,$$

$$y(t) = Ce^{At}x_0 + \int_0^t Ce^{A(t-\tau)}Bu(\tau)d\tau + Du(t), \qquad (5.24)$$

where A, B, C and D have appropriate dimensions and define state-space model, x is the internal state, y the measured output of the system and x_0 is the initial state. We see the matrix exponential plays an important role for the system response. Given a diagonal matrix H

$$H = \begin{bmatrix} h_1 & & & \\ & h_2 & & \\ & & \ddots & \\ & & & h_n \end{bmatrix}, \qquad (5.25)$$

the matrix exponential e^H can be easily calculated as

$$e^H = \begin{bmatrix} e^{h_1} & & & \\ & e^{h_2} & & \\ & & \ddots & \\ & & & e^{h_n} \end{bmatrix}. \qquad (5.26)$$

If an arbitrary matrix F can be diagonalised such that $F = UDU^{-1}$ then $e^F = Ue^DU^{-1}$. Since the eigenvalues do not change in such a transformation, they define the index of the exponential in e^D or the system poles. Thus for a state-space system to be exponentially stable all eigenvalues of the matrix A must have negative real parts.

In feedback control problems, an important property of the state-space system is *controllability*. In general, the concept of controllability relates to how easy it is to move the system through its entire state space. Complete state controllability means that it is possible to move the system state from any initial state to any final state in a finite time using an external input [65, 66]. It is evident that such a concept has huge implications for the performance of a control system as it defines what can and cannot be accomplished with feedback control. One approach to determine if a system is fully controllable is if

$$\mathcal{C} = \begin{bmatrix} B & AB & ... & A^{n-1}B \end{bmatrix},$$

(5.27)

has full rank

$$\text{rank}(\mathcal{C}) = n.$$

(5.28)

There are sometimes practical issues with such binary rank tests as numerical errors may state that a system is fully controllable when in fact it is not. More sophisticated tests are available. The PBH test, which requires that

$$\text{rank} \begin{bmatrix} sI - A & B \end{bmatrix} = n,$$

(5.29)

may yield more reliable results. Techniques have also been devised to quantify the controllability of specific modes [67–69].

The concept of *observability* is also important and is the analog to controllability. Observability means that it is possible to reconstruct the internal state from observations of the system inputs and outputs. In most situations the internal states of the system are not directly accessible. Observability then determines whether it is possible to estimate the state vector. One approach to determining if a system is observable is if

$$\mathcal{O} = \begin{bmatrix} C & AC & ... & A^{n-1}C \end{bmatrix},$$

(5.30)

has full rank

$$\text{rank}(\mathcal{O}) = n.$$

(5.31)

As stated above, there can be practical issues with rank tests, and again the PBH is an alternative observability test which requires that

$$\text{rank} \begin{bmatrix} sI - A \\ C \end{bmatrix} = n.$$

(5.32)
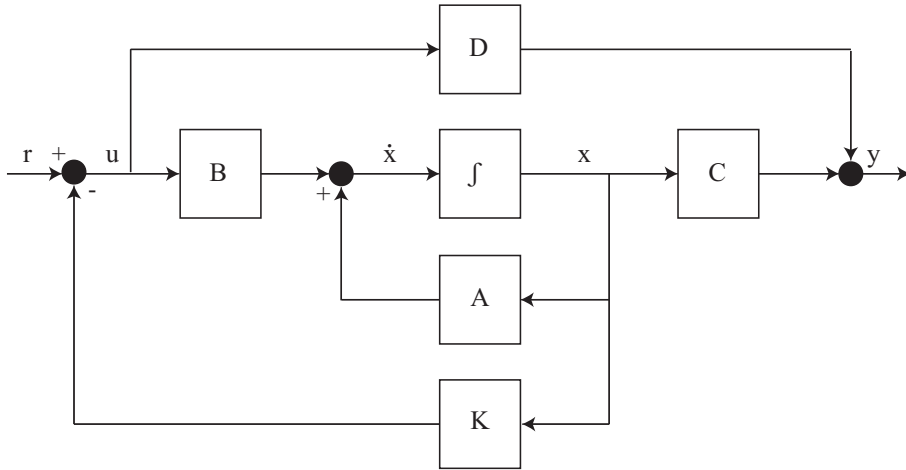
Figure 5.6: Block diagram of a static state feedback control loop with an controller K.

The techniques outlined in [67–69] are therefore applicable to observability. For controller design it is clearly advantageous when the system is fully controllable and observable. Let's consider a simple control law for a state-space control system: static state feedback defined by

$$u = -Kx, \tag{5.33}$$

where K is a proportional gain matrix. Here we assume that we have access to the internal state. While this is not always possible, we address this limitation in the following section. For now, we emphasise that this differs from output feedback, which is performed when the system output is used for control purposes. A block diagram for state feedback is illustrated in Fig. 5.6, with a gain matrix K applied to the state vector before the state is fed back to the input. The reference r for this case is zero and thus the feedback loop illustrated in Fig. 5.6 can be mathematically expressed by

$$\dot{x} = (A - BK)x, \tag{5.34}$$
$$y = (C - DK)x, \tag{5.35}$$

where $u = -Kx$ has been substituted into Eq. (5.22). One of the fundamental results in modern control theory is that it is possible to arbitrarily place the closed-loop eigenvalues (or closed-loop poles) of $A - BK$ via selection of K if the system is fully controllable. The previously defined concept of stability is also applicable in the closed-loop case; the system is exponentially stable if all eigenvalues of $A - BK$ have negative real parts. It is worth mentioning that even if the system is not fully controllable, it may still be possible to achieve the design objectives, but there are certain features of the system which cannot be modified.

The previous result suggests that we have unlimited flexibility in enhancing the system performance, however there are practical limitations. To move the system poles significantly often requires large control energy and this is not always feasible. There are physical limitations on the actuators. While the mathematical result holds true, often we must find a compromise between system performance and control energy. This compromise between the system performance and the required control energy can be formulated as an optimisation problem. The *cost function* is typically defined as a quadratic function; in optimal control the following cost function is used extensively

$$\mathcal{J} = \int_0^\infty x^T Q x + u^T R u \, dt, \tag{5.36}$$

where $Q \in \mathbb{R}^{n \times n}$ and $R \in \mathbb{R}^{m \times m}$ are design parameters. The Q term penalises the speed of convergence and the R term regulates the applied control energy. This form of optimisation is known as the linear quadratic regulator (LQR) problem and has been well studied. For a more in-depth treatment see [60, 70]. Solution of this problem yields an interesting result: the optimal control law is static state feedback

$$u = -Kx. \tag{5.37}$$

The full derivation has not been included here as this is a standard result in optimal control theory; the interested reader is referred to [71]. The static feedback gain K is computed by

$$K = (B^T S B + R)^{-1} B^T S A, \tag{5.38}$$

where S satisfies the algebraic Riccati equation [59]

$$A^T[S - SB(B^T S B + R)^{-1} B S]A - S + Q = 0. \tag{5.39}$$

The optimal controller derived for the LQR problem is a static state feedback controller, essentially a proportional controller. Such a controller possesses some limitations such as steady-state error and the inability to cope with constant disturbances. Furthermore state feedback cannot be realised if the internal state is not accessible. Integrators can be used to overcome the inability of eliminating steady state errors as discussed in Chap. 6. To address the problem of the inaccessible state vector, the concept of observers is introduced.

5.5 Optimal Observers

Since we usually do not have access to all internal states, we utilise the concept of observability and knowledge of the measured input and output to construct a state estimate $\hat{x}$. For a sophisticated analysis, we consider the presence of noise sources, both measurement noise v and process noise w. It is assumed that both noise processes are white Gaussian, which is typically not a limitation since coloured noise sources can also be modelled by augmenting additional dynamics into the system description. The modified system description is

$$\dot{x} = Ax + Bu + w, \tag{5.40}$$
$$y = Cx + Du + v, \tag{5.41}$$

where $w \in \mathbb{R}^n$ and $v \in \mathbb{R}^p$.

In 1960, Kalman proposed the *Kalman filter*, the optimal estimator capable of producing minimum-variance state estimates from noisy measurements [29]. The Kalman filter has found widespread application in aeronautics and space exploration, navigation, economics and many others. We introduce the steady-state Kalman filter and highlight how it can generate asymptotically-converging state estimates.

Consider the estimator in Fig. 5.7. That is, the estimator is essentially a mathematical model of the system. In fact, the estimator design problem is the dual problem, the mathematical analog, to the previously introduced LQR problem, where the tuning parameters reflect the process and measurement noises. The time evolution of the state estimate depends on both the measured output and the mathematical model of the system dynamics. The objective is to design the optimal gain L, which determines whether the measured output y or the estimated output $\hat{y} = C\hat{x}$ should be trusted more; this depends on the noise statistics for the given problem. The optimal observer for the system is given by [60]
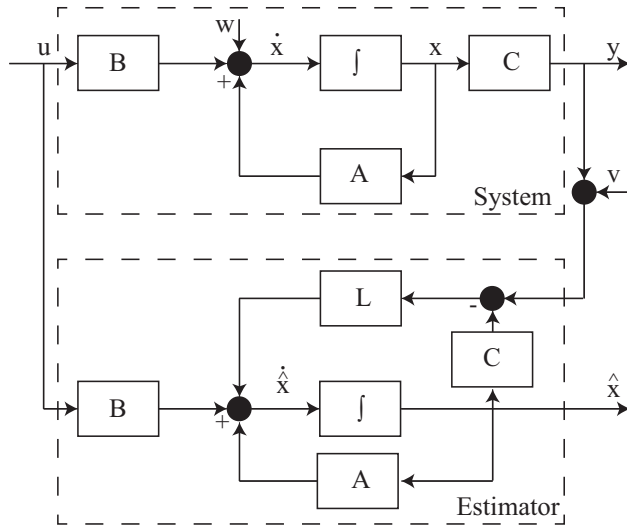
Figure 5.7: Block diagram of an optimal observer estimating the internal state x of a system under consideration.

$$\dot{\hat{x}} = A\hat{x} + Bu + L(y - C\hat{x})$$
$$= (A - LC)\hat{x} + Bu + Ly, \qquad (5.42)$$

where $\hat{x}$ denotes the state estimate and L is determined by

$$L = PC^T V^{-1}. \qquad (5.43)$$

P is the solution of the *algebraic* Riccati equation

$$AP + PA^T - PC^T V^{-1} CP + W = 0, \qquad (5.44)$$

and V and W are the covariances of the above mentioned noises expressed as

$$E(vv^T) = V,$$
$$E(ww^T) = W. \qquad (5.45)$$

Ideally, the observer's state estimate $\hat{x}$ should converge to the actual state x as t goes to ∞. The estimation error e is defined as

$$e(t) = x(t) - \hat{x}(t). \qquad (5.46)$$

Taking the time derivative of the estimation error and inserting it into Eq. (5.42) leads to

$$\dot{e} = Ax + Bu - A\hat{x} - Bu - L(y - C\hat{x}),$$
$$\dot{e}(t) = (A - LC)e(t). \tag{5.47}$$

Here we see that the error between the actual and estimated states e converges to 0 when all eigenvalues of $A - LC$ have strictly negative real parts. Thus even when we are not able to measure the state directly, an observer is capable of generating a state estimate if the system is observable. In the system is not fully observable, only estimates for the observable states can be generated.

Another incredibly useful result is the separation principle [72], which states that the design of an optimal feedback controller for a stochastic system can be achieved by designing an optimal estimator and feeding the optimal state estimate into the deterministic optimal feedback controller as shown in Fig. 5.8. This combination is better known as a *linear quadratic Gaussian* (LQG) controller. The derived LQG controller is a combination of a LQR and a steady-state Kalman filter and is applied for a cavity locking experiment described in Chap. 6. A LQG controller can also be realised with a time-varying Kalman filter, which is discussed in Chap. 7. The time-varying Kalman filter assumes the general form of the Riccati equation

$$AP + PA^T - PC^TV^{-1}CP + W = -\dot{P}, \tag{5.48}$$

whereas the time-invariant Kalman filter uses the *algebraic* Riccati equation Eq. (5.44).

5.6 Discrete-Time Systems

The analysis so far has dealt with continuous-time systems. However, usually estimators and controllers are digitally implemented with computers and are discrete-time. While conceptually, there are many similarities between continuous- and discrete-time systems, it is important to acknowledge their differences. The purpose of this section is to briefly outline the conversion of continuous-time systems to discrete-time systems.

The bilinear transform, also known as *Tustin's method*, transforms a continuous-time system into a discrete-time system. Critical to this conversion is the sampling time T of the digital system. The relation between characteristic values in
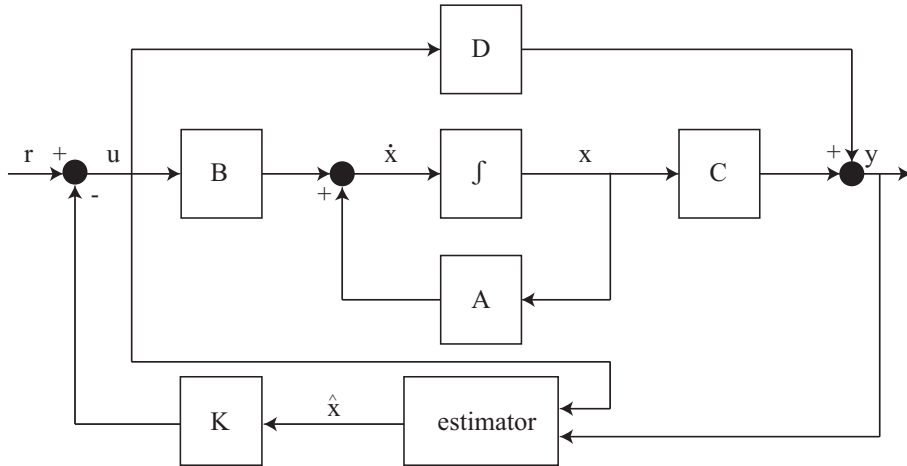
Figure 5.8: Block diagram of a LQG controller. The optimal estimate of an unobservable state is fed to an optimal controller stabilising the system.

the z-plane to those in the s-plane is given by [61]

$$z = e^{sT} \approx \frac{1 + sT/2}{1 - sT/2}, \tag{5.49}$$

This means for example that a pole at $s = -a$ corresponds to a pole $z = e^{-aT}$, but the first-order approximation is often preferred since e^{sT} is infinite dimensional. It can be seen that the poles of a stable continuous-time system, which are located in the left half-plane, are mapped inside the unit circle $|z| = 1$ in the z-plane.

The inverse mapping can also be approximated as

$$
\begin{aligned}
s &= \frac{1}{T} \ln(z), \\
&\approx \frac{2}{T} \left(\frac{z-1}{z+1} \right), \\
&\approx \frac{2}{T} \left(\frac{1 - z^{-1}}{1 + z^{-1}} \right).
\end{aligned}
\tag{5.50}
$$

6

Linear Quadratic Gaussian Control for a Three-Mirror Ring Cavity

Our demonstration of implemented systematic control approaches starts with a controller design for a single input single output (SISO) system. It was given by an optical cavity requiring a feedback loop for length control, or in other words the resonance frequency of the cavity was matched to the frequency of the incident laser field. The problem of frequency matching a cavity is usually known as *locking*. Although this SISO system was not highly complex, it is a suitable test bed for modern control approaches and of interest for a myriad of experiments. For applications in fields such as spectroscopy [73, 74], quantum information [75, 76], optical imaging [77] and many others it is necessary to lock the cavity length of an optical resonator to the frequency of a laser (or vice versa) to achieve transmission of the light through the cavity (or a desired frequency noise reduction). Another reason for our investigations was that one of the most advanced applications that necessitates cavity locking is a interferometric gravitational wave detector (GWD) [17, 78].

We designed and implemented an integral linear quadratic Gaussian (LQG) controller to achieve cavity lock for a three-mirror ring cavity in cooperation with the groups of Prof. I. R. Petersen and Prof. E. H. Huntington. The results of our novel test bed for modern control approaches, consisting of a three-mirror ring cavity, were published in [31, 79]. Previous results published by this cooperation involved the locking of a linear optical cavity with a LQG controller [80, 81].
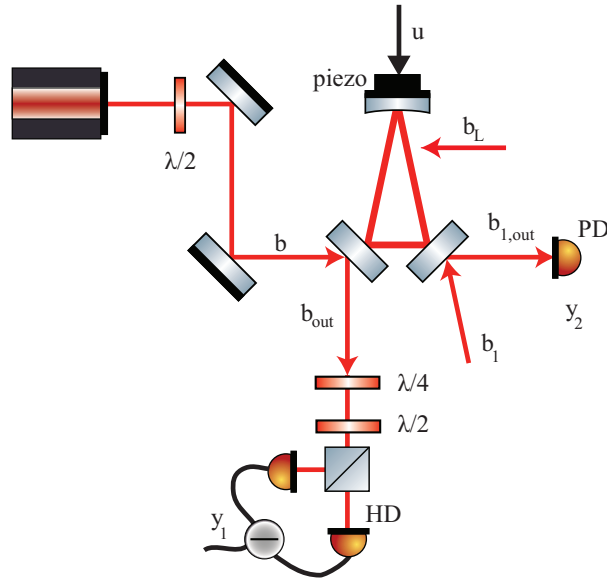
Figure 6.1: Schematic of the optical plant including the optical fields b_i, the control input to the piezoelectric actuator u and the measured outputs y_1 and y_2 corresponding to the error signal and the transmitted signal respectively. HD, PD, $\lambda/2$ and $\lambda/4$ refer to homodyne detector, single photodetector, half-wave and quarter-wave waveplate respectively.

6.1 Experimental Setup

We set up an impedance-matched three-mirror ring cavity as shown schematically in Fig. 6.1 to demonstrate operation of a modern controller. The length control of an optical cavity can be realised by controlling a piezoelectric transducer (PZT), which is attached to one of the cavity mirrors. The parameters of the optical resonator (given in Table 6.1) were chosen to provide easy and convenient handling of the system to test new locking schemes. For this reason, a cavity with a low finesse of $\mathcal{F} \approx 10$ and a correspondingly large spectral linewidth of $\Delta\nu \approx 65\,\mathrm{MHz}$ (equivalent to a decay rate $\kappa \approx 410 \cdot 10^6\,\frac{\mathrm{rad}}{\mathrm{s}}$) was constructed. This results in a small power build-up within the optical resonator and a suitably large linear region of the error signal, which simplifies the locking procedure.

Table 6.1: Parameters of the optical ring cavity.

Parameter	Value
Wavelength	$1550\,\mathrm{nm}$
Finesse	≈ 10
Spectral linewidth	$\approx 65\,\mathrm{MHz}$
Waist	$453\,\mu\mathrm{m}$

Furthermore a ring cavity setup was chosen to simplify the implementation of the homodyne locking scheme [46], since the incoming light field is spatially separated from the reflected light field. Homodyne locking [46] generates the error signal via polarisation spectroscopy of the system. Hence, the two measured output signals are y_1, the phase quadrature of the reflected beam measured via a HD, and y_2, the intensity of the transmitted beam measured by a single PD. Signal y_2 is not required for the design process of a feedback control loop, however it is convenient to verify that the system is in lock via the maximised transmitted power. The light source for our test bed was a fibre-coupled diode laser with a wavelength of $\lambda = 1550\,\mathrm{nm}$. Since a systematic control approach is based on a model describing the system dynamics, we derived a state-space model, see Chap. 5, describing the equations of motion for an optical cavity.

6.2 State Space Representation of Cavity Dynamics

With the introduction of quantised electromagnetic fields and coherent states, see Chap. 2, and the derivation of the field amplitudes for an optical cavity, see Chap. 4, we were able to formulate the quantum equations of motion for our system in the Heisenberg picture [82]. The quantum equations of motion for the intracavity field represented by the annihilation operator $\hat{a}$ and the equation for the reflected field $\hat{b}_{out}$ are given by [34], whereby for simplicity reasons the 'hat

formalism' will be dropped in the following equations,

$$\dot{a} = -\left(\frac{\kappa}{2} - i\Delta\right)a - \sqrt{\kappa_0}\left(\beta + b_0\right) - \sqrt{\kappa_l}b_l - \sqrt{\kappa_L}b_L,$$
$$b_{out} = \sqrt{\kappa_0}a + \beta + b_0. \tag{6.1}$$

b is the annihilation operator of the input light field, which can be expressed in a linearised form as a boson field $b = \beta + b_0$. Hereby the operator b is written as a combination of a complex number β describing the amplitude and an operator b_0 describing a vacuum field. Hence, b_0 describes the fluctuations of the field b and defines them to be white Gaussian with unit variance. All of these field equations were formulated in a rotating reference frame with respect to the frequency of the boson field b. κ is the total decay rate of the cavity and is the sum of the individual decay rates κ_0, κ_l and κ_L of the optical fields b, b_l (the vacuum field from the rear plane mirror/output coupler) and b_L (the optical loss field) coupling to the cavity, respectively

$$\kappa = \kappa_0 + \kappa_l + \kappa_L. \tag{6.2}$$

Δ is the frequency detuning, introduced in Chap. 4, between the optical cavity and laser given by

$$\Delta = f_c - f_L = q\frac{c}{nL} - f_L, \tag{6.3}$$

where f_c is the resonance frequency of the cavity, f_L the laser frequency, nL the optical path length of the cavity, consisting of an index of refraction n and L the physical path length, c the speed of light and q a large integer indicating the qth longitudinal cavity mode.

Due to the non-linear error signal Δ of the system, the dynamics to be controlled Eq. (6.1) also become non-linear. However the region of interest around $\Delta = 0$ corresponds to the linear region of the error signal. Hence, in order to enable the use of linear control techniques we linearised the dynamics around $\Delta = 0$. The intracavity field can be described by $a = \alpha + \tilde{a}$, where α is the steady state amplitude mean value of a and $\tilde{a}$ denotes the perturbation operator satisfying

$$\dot{\tilde{a}} = -\frac{\kappa}{2}\tilde{a} + i\Delta\alpha - \sqrt{\kappa_0}b_0 - \sqrt{\kappa_l}b_l - \sqrt{\kappa_L}b_L,$$
$$\tilde{b}_{out} = \sqrt{\kappa_0}\tilde{a} + b_0. \tag{6.4}$$

This set of equations describes the perturbed intracavity and output fields. The perturbed output $\tilde{y}_1$, which is a part of the feedback loop, can be expressed as

$$\tilde{y}_1 = e^{-i\phi}b_{out} + e^{i\phi}b_{out}^\dagger$$
$$= \sqrt{\kappa_0}\left(e^{-i\phi}\tilde{a} + e^{i\phi}\tilde{a}^\dagger\right) + q_0, \tag{6.5}$$

where q_0 is a Gaussian white noise process describing the noise of the input field $q_0 = b_0 + b_0^\dagger$ and ϕ is the homodyne measurement angle. For our polarisation-based homodyne locking scheme, ϕ is determined by the orientation of the quarter-wave/half-wave plate combination.

In the real physcial experiment we measure the amplitude and phase quadrature, which are defined as

$$q = a + a^\dagger, \qquad p = i(a^\dagger - a). \tag{6.6}$$

Taking the perturbed form of the quadrature operators into account, we can rewrite the cavity dynamics in state space form

$$\begin{bmatrix} \dot{\tilde{q}} \\ \dot{\tilde{p}} \end{bmatrix} = \begin{bmatrix} -\frac{\kappa}{2} & 0 \\ 0 & -\frac{\kappa}{2} \end{bmatrix}\begin{bmatrix} \tilde{q} \\ \tilde{p} \end{bmatrix} + \begin{bmatrix} 0 \\ 2\alpha \end{bmatrix}\Delta$$
$$-\sqrt{\kappa_0}\begin{bmatrix} \cos\phi & \sin\phi \\ -\sin\phi & \cos\phi \end{bmatrix}\begin{bmatrix} q_0 \\ p_0 \end{bmatrix}$$
$$-\sqrt{\kappa_l}\begin{bmatrix} 1 & 0 \\ 0 & 1 \end{bmatrix}\begin{bmatrix} q_l \\ p_l \end{bmatrix} - \sqrt{\kappa_L}\begin{bmatrix} 1 & 0 \\ 0 & 1 \end{bmatrix}\begin{bmatrix} q_L \\ p_L \end{bmatrix} \tag{6.7}$$
$$y_1 = k_2\sqrt{\kappa_0}\begin{bmatrix} \cos\phi & \sin\phi \end{bmatrix}\begin{bmatrix} \tilde{q} \\ \tilde{p} \end{bmatrix} +$$
$$k_2\begin{bmatrix} 1 & 0 \end{bmatrix}\begin{bmatrix} q_0 \\ p_0 \end{bmatrix} + \tilde{v}_1, \tag{6.8}$$

where $q_i = b_i + b_i^\dagger$ and $p_i = i(b_i^\dagger - b_i)$ are the noise quadratures for $i = 0, l, L$. k_2 is the transfer impedance gain, including the quantum efficiency of the HD, with electronic noise $\tilde{v}_1$. The homodyne detection angle ϕ is set to $\pi/2$, since the polarisation-based homodyne detection scheme is a phase-sensitive measurement. Before we were able to implement a suitable controller based on the derived state-space model we had to overcome two challenges, explained in the next sections.
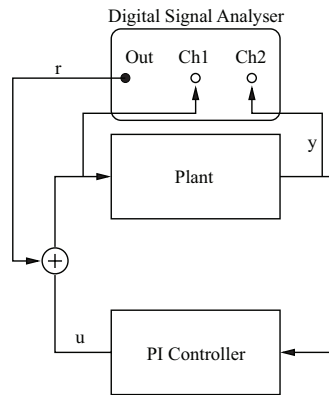
Figure 6.2: Block diagram of the setup for measuring the transfer function of the optical cavity, with u the controlled input, r the swept sine and y the error signal. [31]

6.3 Frequency Response and System Identification

Unfortunately, the analytically derived state space model does not completely describe the physical system. The true physical dynamics were more complex due to the dynamics of the piezoelectric actuator attached to one of the end mirrors to control the cavity length. Hence, we measured the cavity transfer function which we were able to use to construct a state-space model, mirroring the true dynamics, by utilising subspace system identification [83]. The relation of transfer functions and a state-space model are described in Chap. 5.

We obtained the transfer function of our plant, including the dynamics of the PZT, by injecting a swept sine r into the controlled input u and measuring the error signal y_1 generated via the homodyne detection scheme. The HP 35665A 2-channel digital signal analyser (DSA) generated the swept sine and recorded the input signal $u+r$ and the output signal y_1. A block diagram of the setup used for frequency response measurement is shown in Fig. 6.2. The signal $u+r$ was enhanced by a high-voltage amplifier, driving the PZT and the desired frequency response data $\mathrm{transferfunction} = Y(s)/(U(s) + R(s))$ was generated via a fast Fourier transform (FFT) performed by the DSA. During the data acquisition for the transfer function, we held the cavity in lock with a suitable PI controller. Keeping the system on resonance and choosing an appropriate input signal $u+r$
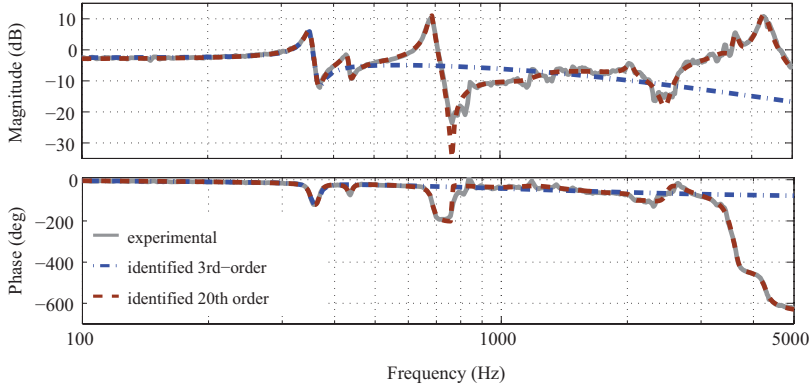
Figure 6.3: Bode plot of the experimentally acquired frequency response of the plant in comparison to two simulated models. [31]

is essential to guarantee that the range of the output y corresponds to its linear region. This was essential to ensure the applicability of linear control techniques. The Bode plot illustrating the frequency response of the plant and two plant models are shown in Fig. 6.3. For the control design process we took the frequency data up to the first resonance into account. This was done since usually it is only necessary to suppress the first resonant mode, as the primary mode of the optical cavity/PZT combination should have the strongest impact on the dynamics [84, 85], although this was not the case for our setup (third mode was dominant). We used truncated frequency response data, regarding a range from 100 Hz to 400 Hz, for the subspace system identification. We fitted a third-order model to the data, which was then used for the controller design. We computed the model with the help of the iterative prediction error minimisation (PEM) method from Matlab's system identification toolbox [86]. We also fitted a 20th-order model, incorporating the complete frequency data. We could have used the 20th-order model for the controller design as well, but the third-order model was computationally more convenient. The third-order model describing the input/output relation of the plant was used to construct a state-space model of the well-known

form, see Chap. 5,

$$\dot{x} = Ax + Bu,$$
$$y = Cx + Du,$$

where

$$A = 10^4 \cdot \begin{bmatrix} -0.0180 & -0.2865 & 0.0573 \\ 0.1693 & -0.0157 & 0.2339 \\ 0.0446 & 0.1109 & -1.1449 \end{bmatrix}$$

$$B = \begin{bmatrix} 2.8394 \\ 4.2852 \\ -24.9287 \end{bmatrix}$$

$$C = \begin{bmatrix} 24.0014 \\ 37.3086 \\ -34.4903 \end{bmatrix}^{T}$$

$$D = 0. \tag{6.9}$$

6.4 Controller Design

The control objective is to drive the detuning Δ to zero. Since we cannot measure the state of the intracavity field directly an observer/estimator was required. This lead to a LQG control approach, presented in detail in Chap. 5, which was augmented due to several limitations of static state feedback control. Firstly, feedforward control is required to eliminate steady state tracking error, and therefore perfect knowledge of the plant model is required. Secondly, with static state feedback, the states cannot converge in the presence of constant input/output disturbances. To regulate the detuning Δ to 0 in the presence of unmodelled external disturbances, such as $1/f$ laser phase noise, integral control must be included. Integral action can be built into the LQG problem by adding another system state, $q_{k+1} = q_k + y_k$, which integrates the system output. The discrete-

time augmented state-space model then becomes

$$\begin{bmatrix} x \\ q \end{bmatrix}_{k+1} = \begin{bmatrix} A & 0 \\ C & I \end{bmatrix} \begin{bmatrix} x \\ q \end{bmatrix}_k + \begin{bmatrix} B \\ 0 \end{bmatrix} \tilde{u}_k + \tilde{w}_k \qquad (6.10)$$

$$\tilde{y}_k = \begin{bmatrix} C & 0 \end{bmatrix} \begin{bmatrix} x \\ q \end{bmatrix}_k + \tilde{v}_k, \qquad (6.11)$$

with $\tilde{v} = [v_1 v_2]^T$. The LQG control design can be performed on the augmented system $\left\{ \tilde{A}, \tilde{B}, \tilde{C} \right\}$ where

$$\tilde{A} = \begin{bmatrix} A & 0 \\ C & I \end{bmatrix}; \quad \tilde{B} = \begin{bmatrix} B \\ 0 \end{bmatrix}; \quad \tilde{C} = \begin{bmatrix} C & 0 \end{bmatrix}; \quad \tilde{x} = \begin{bmatrix} x \\ q \end{bmatrix}.$$

We chose the following weighting factors for the implementation of the LQG controller. The weighting matrices for the LQR and Kalman filter cost functional were

$$Q_L = \sigma_1^2 = 1, \qquad R_L = \begin{bmatrix} \sigma_2^2 & 0 \\ 0 & \sigma_3^2 \end{bmatrix} = \begin{bmatrix} 1 & 0 \\ 0 & 10^{-7} \end{bmatrix},$$

$$Q_K = q = 5 \cdot 10^5, \qquad R_K = r = 0.5. \qquad (6.12)$$

σ_1 is the standard deviation related to the process noise $\tilde{w}$, σ_2 and σ_3 are the measurement noises associated with the HD and the augmented integral output, respectively. The noise covariances and weighting parameters were considered to be design parameters and do not need to reflect physical covariances of the system [87]. We determined the above stated values to generate a controller with a sufficient bandwidth [88]. The resulting controller was robust to errors in plant modelling, was able to reject constant disturbances and was able to drive the detuning to 0. A Bode plot of the LQG controller, defined by the ratio between the controller output u and controller input (error signal) e, is shown in Fig. 6.4.

6.5 Controller Implementation

We implemented the discretised state-space model for the LQG controller including integral action with a DS1104 dSPACE DSP system. The dSpace board consists of 8 Digital-to-Analog-Converter (DAC) channels and 16 Analog-to-Digital-Converter (ADC) channels with a sampling rate of $300\,\text{kHz}$. The board is fully
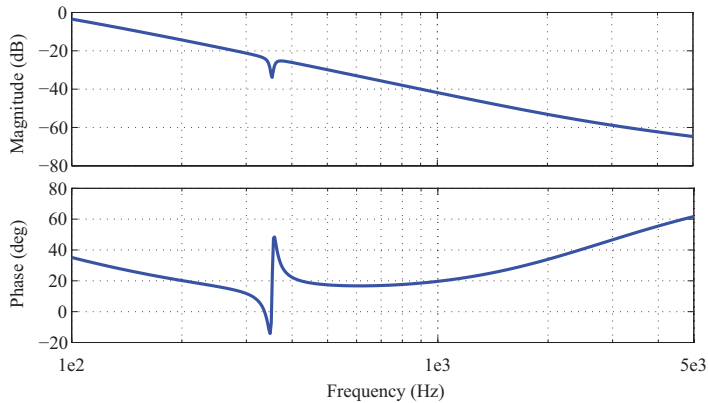
Figure 6.4: Bode plot of the LQG controller. [31]

programmable via Matlab's Simulink toolbox and possesses a 12-bit resolution. With the help of this hardware we were able to successfully implement a LQG controller based on a third-order model. The controller was capable of achieving lock and its bandwidth was not limited by the hardware. A schematic of the closed loop system is depicted in Fig. 6.5.

6.6 Results

The LQG controller state feedback gain was computed to obtain appropriate values for the gain crossover frequency, gain margin, and phase margin of the loop gain corresponding to the product of the augmented plant transfer function and the integral LQG controller transfer function. We achieved suitable margins by tuning the weighting parameters. Furthermore we used the loop gain transfer function to characterise the designed feedback control loop [62]. The simulated frequency response for the corresponding loop gain transfer function is shown in Fig. 6.6, which has a gain margin of $20.2\,\text{dB}$ at $251\,\text{Hz}$, a phase margin of $47°$ at $61\,\text{Hz}$, and a gain crossover frequency of $61\,\text{Hz}$. We chose these robustness margin values in order to ensure closed-loop stability of the system. A guide to adequate robustness margins for LQG controllers is described in [89]. We evaluated the performance of the closed-loop system with the integral LQG
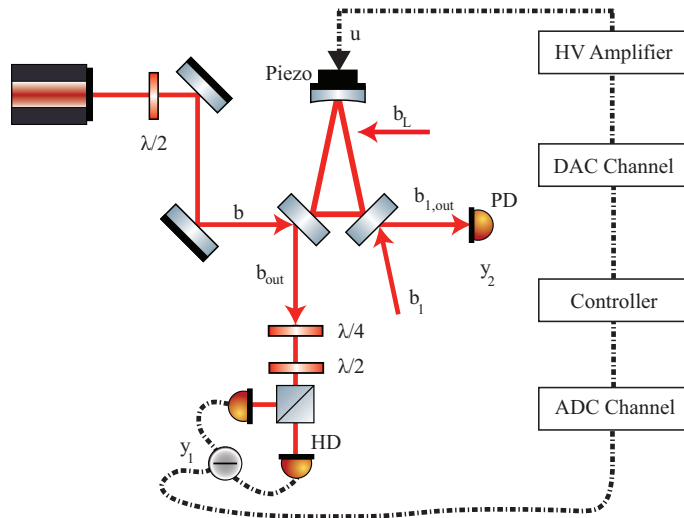
Figure 6.5: Schematic of the cavity locking experiment, including the combination of a time-invariant Kalman filter and a linear quadratic regulator. The dashed lines depict electronic links.
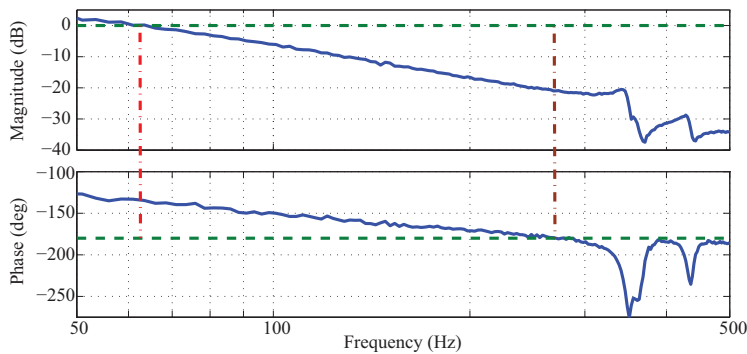
Figure 6.6: Loop gain of the three-mirror ring cavity test bed system with integral LQG control. The cross sections of the dashed lines denote the gain and phase margin. The gain margin is $20.2\,\text{dB}$ at $251\,\text{Hz}$ and the phase margin is $47°$ at $61\,\text{Hz}$. [31]

Figure 6.7: Comparison between a measured close loop step response and a simulation based on a 20th-order plant model. [31]

controller by injecting a step function and measuring the system response. We compared the acquired data with a simulation, which used the 20th-order model for the description of the plant. The comparison is shown in Fig. 6.7 and the resulting closed-loop frequency response is plotted in Fig. 6.8. We applied a step input of 0.04 V for the characterisation of the integral LQG controller. The same step function was used for the simulation. The output y_1 of the plant, initially at 0 V, settles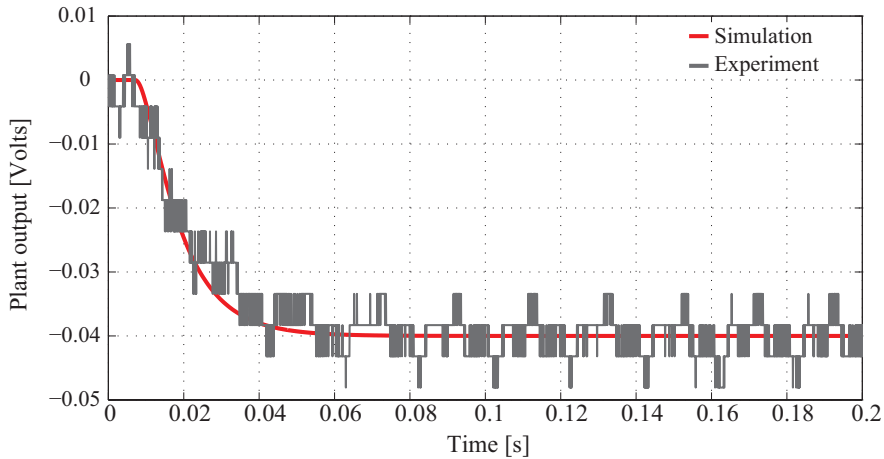 within 0.1 s to a mean value of -0.0391 V. We demonstrated that the performance of the closed-loop system was stable over all operational conditions. Furthermore the optical cavity lock was able to keep the system on resonance over extended periods of time. Fig. 6.9 highlights the functionality of the controller. The controller satisfied its objective and kept the system on resonance, leading to an error signal close to zero, and the corresponding transmitted power is maximised. The reason for the observed noise in the experimental step response is assumed to be due to quantisation effects arising from the 12-bit resolution of the ADCs. These quantisation effects could have been the reason for the noisy signals shown in Fig. 6.9. An option to solve this quantisation problem is the acquisition of a new dSPACE board including ADCs with an improved dynamic range.
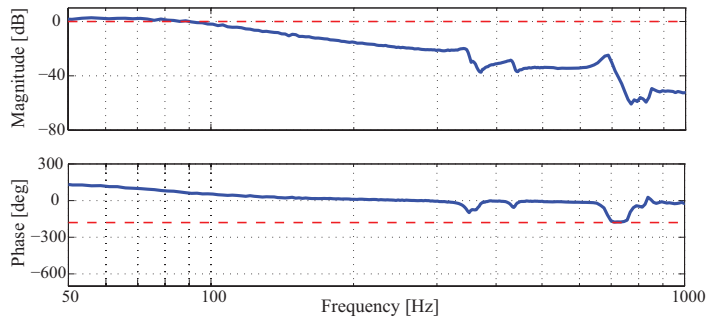
Figure 6.8: Closed loop frequency response of the three-mirror ring cavity. [31]
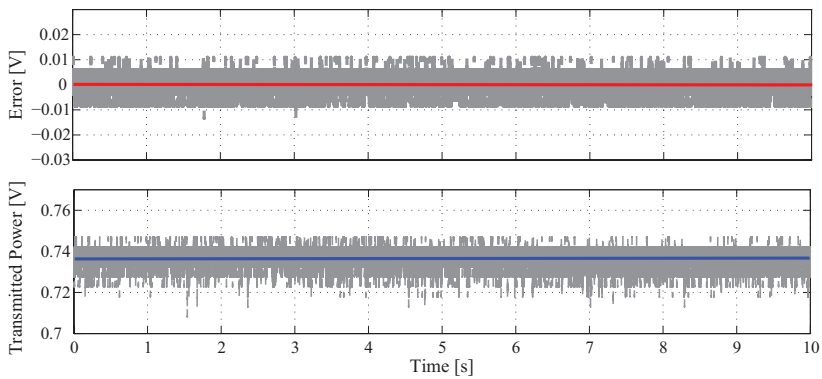
Figure 6.9: Measured time data of the error signal and the transmitted power, while the system was in lock. The mean values of the plots are the red and blue lines corresponding to 0 V and 0.738 V, respectively. [31]

6.7 Conclusions

In this chapter we demonstrated a successful implementation of a modern con-
troller by applying modern control techniques. We used a third-order state-space
model model, describing the plant, for the computation of a LQG controller with
integral action. We satisfied the control objective by acquiring lock with our mod-
ern controller. We verified the stability and performance of the feedback loop via
step response data. This data was compared with a simulated step response of
the plant. In addition to the successful control implementation, we also designed
a test bed for systematic modern control approaches regarding the challenge of
frequency locking optical cavities.

7

Autolocking an Optical Cavity Using a Time-Varying Kalman Filter

In the previous chapter we demonstrated a modern control approach capable of locking an optical resonator. A strict requirement for this locking scheme is that the initial system is not strongly detuned. Therefore the detuning Δ does not exceed the linear region of the error signal. Since the error signal is inherently non-linear lock cannot be acquired outside of its linear region via linear control techniques. In general the non-trivial lock acquisition is achieved by an auto-mated process which scans the cavity length with a PZT until the fundamental resonance is found by detecting the transmitted power. At that point the scan stops and the controller is engaged. This process, known as *autolocking* [90] eases and speeds up the lock acquisition. This is important to guarantee a high duty-cycle for long-term experiments/projects like a gravitational wave detector (GWD).

In this chapter we introduce a new autolocking scheme based on a systematic control approach utilising the combination of an integral LQR and a time-varying Kalman filter (TVKF). This scheme was proposed in [91] and the simulated re-sults highlighted that, with respect to the linear region of the error signal, the lock acquisition was more robust and faster than PI control. Furthermore the simulation showed that this control scheme was able to perform even when the non-linear error signal was not in the linear region, which cannot be overcome by PI control or a static integral LQG controller with a time-invariant Kalman

filter.

We implemented and thereby verified the superior performance of the integral
LQG/TVKF combination. The results are published in [32].

7.1 Experimental Setup

We used the constructed test bed, introduced in Chap. 6 (see Fig. 6.1), to demon-
strate the superior performance of our novel control scheme. Although the exper-
imental setup stayed unchanged, we needed to reformulate the state-space model
of the system. Firstly the TVKF needs the information of a phase-sensitive and
an amplitude measurement to quantitatively determine the detuning Δ. Hence
we needed to add an additional output signal y_2 to the state-space model. The
phase-sensitive output signal y_1 is given by the error signal, generated via
polarisation-based homodyne detection [46]. The additional amplitude measure-
ment y_2 is obtained by detecting the transmitted power with a single detector.
Secondly the state-space model given in Chap. 6 was based on a linearisation
of the system around zero detuning. However for the TVKF approach we took
the non-linear region of the error signal into account as well, since we wanted to
demonstrate that this approach is able to cope with this non-linear control prob-
lem and acquires lock from any operating point.

We extend the quantum equations of motion [34] from Eq. (6.1) by the second
output field $b_{l,out}$

$$\dot{a} = -\left(\frac{\kappa}{2} - i\Delta\right) a - \sqrt{\kappa_0}\left(\beta + b_0\right) - \sqrt{\kappa_l}b_l - \sqrt{\kappa_L}b_L,$$
$$b_{out} = \sqrt{\kappa_0}a + \beta + b_0,$$
$$b_{l,out} = \sqrt{\kappa_l}a + \beta + b_l. \tag{7.1}$$

a is the annihilation operator of the intracavity field and b the annihilation op-
erator of the incident light field. This laser input is expressed as a boson field
$b = \beta + b_0$, with β denoting the coherent field amplitude and b_0 describing the
field fluctuations. κ is the total decay rate of the cavity, which is given by the
sum of the individual decay rates κ_i of the optical fields b_i, with $i = 0, l, L$. The

two detected outputs are expressed as

$$
\begin{aligned}
y_1 &= e^{-i\phi}b_{out} + e^{i\phi}b_{out}^{\dagger} \\
&= \sqrt{\kappa_0}(e^{-i\phi}a + e^{i\phi}a^{\dagger}) + 2\beta\cos\phi + q_0 \\
y_2 &= b_{1,out}^{\dagger}b_{1,out} \\
&= \kappa_l a^{\dagger}a + \sqrt{\kappa_l}(a^{\dagger}b_l + b_l^{\dagger}a) + b_l^{\dagger}b_l,
\end{aligned}
\tag{7.2, 7.3}
$$

where q_0 is Gaussian white noise of the input field and ϕ describes the homodyne detection angle. With these sets of equations we were able to reformulate the state-space model, where the state x is described by the amplitude q and phase p quadrature

$$
\begin{aligned}
\begin{bmatrix} \dot{q} \\ \dot{p} \end{bmatrix} &= \begin{bmatrix} -\frac{\kappa}{2} & -\Delta \\ \Delta & -\frac{\kappa}{2} \end{bmatrix} \begin{bmatrix} q \\ p \end{bmatrix} - \begin{bmatrix} 2\beta\sqrt{\kappa_0} \\ 0 \end{bmatrix} \\
&\quad -\sqrt{\kappa_0} \begin{bmatrix} \cos\phi & \sin\phi \\ -\sin\phi & \cos\phi \end{bmatrix} \begin{bmatrix} q_0 \\ p_0 \end{bmatrix} \\
&\quad -\sqrt{\kappa_l} \begin{bmatrix} 1 & 0 \\ 0 & 1 \end{bmatrix} \begin{bmatrix} q_l \\ p_l \end{bmatrix} - \sqrt{\kappa_L} \begin{bmatrix} 1 & 0 \\ 0 & 1 \end{bmatrix} \begin{bmatrix} q_L \\ p_L \end{bmatrix}
\end{aligned}
\tag{7.4}
$$

$$
\begin{aligned}
y_1 &= k_2\sqrt{\kappa_0} \begin{bmatrix} \cos\phi & \sin\phi \end{bmatrix} \begin{bmatrix} q \\ p \end{bmatrix} \\
&\quad + k_2 \begin{bmatrix} 1 & 0 \end{bmatrix} \begin{bmatrix} q_0 \\ p_0 \end{bmatrix} + 2k_2\beta\cos\phi + \tilde{v}_1
\end{aligned}
\tag{7.5}
$$

$$
y_2 = \tilde{k}_2 \left(\frac{\kappa_l}{4}(p^2 + q^2) + \frac{\sqrt{\kappa_l}}{2} \begin{bmatrix} q & p \end{bmatrix} \begin{bmatrix} q_l \\ p_l \end{bmatrix} \right) + \tilde{v}_2,
\tag{7.6}
$$

where k_2 and $\tilde{k}_2$ denote the transfer impedance of the HD and PD, respectively and $\tilde{v}_i$ are sensor noises of the associated output. As mentioned in Chap. 6, the mathematical state-space model does not describe the complete physical dynamics, which were more complex due to the PZT attached to one of the mirrors for the length actuation. We obtained the physically exact input/output relation via a transfer function of the plant. The frequency data were used to generate a state-space model via subspace system identification [83].

7.2 Singular Perturbation Method

Until now all of the applied techniques correspond to linear control techniques, although we consider a non-linear control problem. We tackled this issue by simplifying the system via the singular perturbation method [92] and implementing the TVKF. This ensured that a linear control approach can still be applied. The singular perturbation method decomposes the plant, consisting of the optical cavity and the two readouts, into two subsystems which differ by their time constants. This technique is known as *separation of time-scales*. For our case the dynamics of the light fields are fast compared to the mechanical assembly. The slow mechanical block whose output is the detuning Δ is the dominant effect. It is followed by a fast block representing a discrepancy from the dominant behaviour. This discrepancy can be modelled as a static sensor non-linearity applied to the output. This approach enabled the use of linear control techniques. Static non-linearities imply that the time derivatives $\dot{q} = \dot{p} = 0$. With the help of this relation we determined the behaviour of the static non-linearity

$$\begin{bmatrix} q \\ p \end{bmatrix} = \frac{-1}{\left(\frac{\kappa}{2}\right)^2 + \Delta^2} \begin{bmatrix} \kappa\beta\sqrt{\kappa_0} \\ 2\beta\sqrt{\kappa_0}\Delta \end{bmatrix}. \tag{7.7}$$

For the homodyne locking scheme [46] the detection angle is set to $\phi = \pi/2$ and the outputs y_1 and y_2 become

$$\begin{aligned}
y_1 &= k_2\sqrt{\kappa_0}p + 2k_2\beta\cos\phi + v_1 \\
&= -\frac{2k_2\beta\kappa_0\Delta}{\left(\frac{\kappa}{2}\right)^2 + \Delta^2} + v_1 \\
&= f_1(\Delta) + v_1, \tag{7.8} \\
y_2 &= \frac{\tilde{k}_2\kappa_1\left(p^2 + q^2\right)}{2} + v_2 \\
&= \frac{1}{2}\frac{\tilde{k}_2\kappa_1\kappa_0\beta^2}{\left(\frac{\kappa}{2}\right)^2 + \Delta^2} + v_2 \\
&= f_2(\Delta) + v_2. \tag{7.9}
\end{aligned}$$

If the optical cavity is perturbed strongly enough and the error signal leaves its linear regime, we cannot unambiguously determine the detuning if y_1 is the only measurement, as shown in Fig. 7.4. Therefore we complemented y_1 with y_2 to

correctly ascertain the detuning. Even when both y_1 and y_2 are considered, both signals tend to zero for very large detuning and become very sensitive to noise. Because of this we set up a *bounded noise model*, estimating the actual state of our system via noise-corrupted measurements. In our case the measurement noise was unknown but bounded. To fulfil this constraint at each time instant the measurement noises $v_{1,k}$ and $v_{2,k}$ need to satisfy the inequalities

$$v_{1,k}^2 \leq \mu_1^2; \qquad v_{2,k}^2 \leq \mu_2^2, \tag{7.10}$$

where μ_1 and μ_2 are constants defining the upper magnitude bound of the noise. In the next step we handled the problem of characterising the set of all possible Δ_k consistent with the measured outputs $y_{1,k}$ and $y_{2,k}$ to determine the set $\mathcal{S}_k$ that fulfils the inequalities in Eq. (7.10),

$$
\begin{aligned}
\mathcal{S}_k \;=\; &\Big\{ \Delta_k \in \mathbb{R} : (y_{1,k} - f_1(\Delta_k))^2 \leq \mu_1^2 \ \text{ and} \\
& \qquad (y_{2,k} - f_2(\Delta_k))^2 \leq \mu_2^2 \Big\}.
\end{aligned}
\tag{7.11}
$$

Using Eq. (7.8)-(7.10) it is straightforward to show that $\mathcal{S}_k$ corresponds to the set of $\Delta_k \in \mathbb{R}$ satisfying the inequalities

$$
\begin{aligned}
(16\Delta_k^4 + \kappa^4)(y_{1,k}^2 - \mu_1^2) &+ 64\Delta_k^3 k_2 \beta \kappa_0 y_{1,k} \\
&+ 8\Delta_k^2 (8k_2^2 \beta^2 \kappa_0^2 + \kappa^2 y_{1,k}^2 - \kappa^2 \mu_1^2) \\
&+ 16\Delta_k k_2 \beta \kappa_0 \kappa^2 y_{1,k} \leq 0,
\end{aligned}
\tag{7.12}
$$

$$
\begin{aligned}
(16\Delta_k^4 + \kappa^4)(y_{2,k}^2 - \mu_2^2) & \\
+ 8\Delta_k^2 (\kappa^2 y_{2,k}^2 - 4k_3 \kappa_0 \beta^2 y_{2,k} - \kappa^2 \mu_2^2) & \\
- 8\kappa^2 k_3 \beta^2 \kappa_0 y_{2,k} + 16 k_3^2 \beta^4 \kappa_0^2 &\leq 0.
\end{aligned}
\tag{7.13}
$$

The set $\mathcal{S}_k$ is computed by solving the inequalities Eq. (7.12) and Eq. (7.13) using a numerical analysis, known as *Laguerre's method* [93, 94]. If we obtain m roots as a solution, they will define $m+1$ regions of interest:

$$
\begin{aligned}
\mathcal{S}_{k,1} &= \{\Delta_k \in \mathbb{R} : -\infty < \Delta_k < \Delta_{k,1}\} \\
\mathcal{S}_{k,2} &= \{\Delta_k \in \mathbb{R} : \Delta_{k,1} < \Delta_k < \Delta_{k,2}\} \\
&\;\;\vdots \\
\mathcal{S}_{k,m} &= \{\Delta_k \in \mathbb{R} : \Delta_{k,m-1} < \Delta_k < \Delta_{k,m}\} \\
\mathcal{S}_{k,m+1} &= \{\Delta_k \in \mathbb{R} : \Delta_{k,m} < \Delta_k < \infty\}.
\end{aligned}
$$

The set $\mathcal{S}_k$ consists of the subsets $\mathcal{S}_{k,i}$, satisfying Eq. (7.12) and Eq. (7.13) at time
instant k. Let us briefly outline the reasons for this approach: To apply the TVKF,
we must transform the given measurements y_1 and y_2 into the mean detuning $\bar{\Delta}_k$
and its variance. Thus we present a heuristic approach, which attempts to convert
the given information into the required quantities. The set $\mathcal{S}_k$ can be non-convex;
it is possible for two regions on either side of the resonance peak to satisfy the
inequalities when the detuning is large. In this situation, we want to inform
the Kalman filter that there is a large uncertainty in this measurement, which is
reflected by a large variance. Therefore, when we have a non-convex solution set
we consider $\bar{\mathcal{S}}_k$, the convex hull of $\mathcal{S}_k$ (i.e. we force the set to become convex
by including all possible values between the minimum and maximum values),
which makes the set significantly larger with a large variance. On the other hand,
when $\mathcal{S}_k$ only consists of one subset $\mathcal{S}_{k,i}$, the set is equal to its convex hull,
$\mathcal{S}_k = \bar{\mathcal{S}}_k$, and the variance is small, reflecting our increased confidence that
this is in fact the actual detuning. Taking the convex hull of the solution set
is motivated intuitively and we developed the following equations for the mean
value for $\bar{\Delta}_k$ and the standard deviation σ_k, where we have assumed a uniform
distribution over the convex set $\bar{\mathcal{S}}_k$,

$$\bar{\Delta}_k = \frac{1}{2} \left[\min_{\Delta_k \in \bar{\mathcal{S}}_k} (\Delta_k) + \max_{\Delta_k \in \bar{\mathcal{S}}_k} (\Delta_k) \right], \tag{7.14}$$

$$\sigma_k = \frac{1}{2\sqrt{3}} \left[\max_{\Delta_k \in \bar{\mathcal{S}}_k} (\Delta_k) - \min_{\Delta_k \in \bar{\mathcal{S}}_k} (\Delta_k) \right]. \tag{7.15}$$

The quantities $\bar{\Delta}_k$ and σ_k^2 represent the new measurement for the mean detuning
and the measurement covariance. These quantities are the inputs to the TVKF,
which is described in the following section. A schematic highlighting this algo-
rithm is shown in Fig. 7.1.

7.3 Time-Varying Kalman Filter

The Kalman filter utilises the mathematical model of the system and the measure-
ments to estimate inaccessible system states. For an optimal estimate, the pro-
cess and measurement noises must be known white Gaussian processes. There
are two stages to the time-varying Kalman filter: the *prediction step* and the *up-
date step*. In the prediction step, the Kalman filter uses the current state estimate
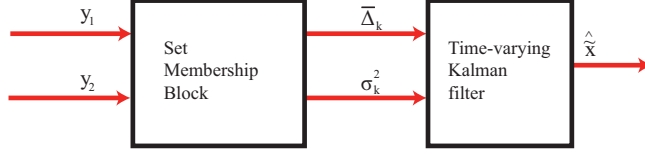
Figure 7.1: Block diagram for the calculation of the state estimate $\hat{\tilde{x}}$. y_1, y_2 are the measured signals, $\bar{\Delta}$ is the estimated mean detuning, and σ^2 is the estimated measurement covariance.

$\hat{\tilde{x}}_k$ and error covariance P_k to predict the state estimate and error covariance at the next time step using the system model:

$$
\begin{aligned}
\hat{\tilde{x}}_{k+1}^- &= \tilde{A}\hat{\tilde{x}}_k + \tilde{B}\tilde{u}_k, & (7.16)\\
P_{k+1}^- &= \tilde{A}P_k\tilde{A}^T + \tilde{B}W\tilde{B}^T, & (7.17)
\end{aligned}
$$

where W is the covariance of the process noise and is assumed to be diagonal. Here, $\hat{\tilde{x}}_k^-$, P_k^- denote the *a priori* state estimate and error covariance. The error covariance in general is defined by the estimation error e_k as

$$
\begin{aligned}
e_k &= \tilde{x}_k - \hat{\tilde{x}}_k \qquad \text{and}\\
P_k &= E\left[e_k e_k^T\right]. & (7.18)
\end{aligned}
$$

The *a posteriori* state estimate and error covariance are given by $\hat{\tilde{x}}_k$ and P_k, respectively.

In the update step, the Kalman filter compares the measured output to the predicted output. The Kalman gain, which is updated at each instant of time, weights the difference between the predicted and measured outputs and *optimally adjusts* the state estimate. The Kalman gain K_k is the optimal weighting factor, based on the specified noise statistics, and it determines whether the measurement or the model-generated state estimate is more reliable at each time instant. K_k is optimal in the sense that it minimises the variance between the actual and estimated states. The following equations summarise the update step, whereas the
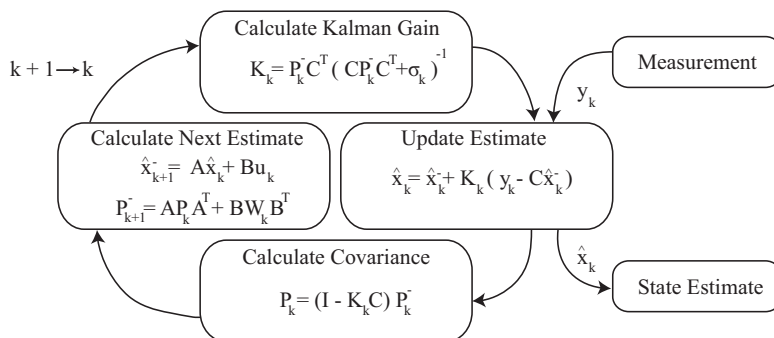
Figure 7.2: Overview of the discrete-time time-varying Kalman filter.

error covariance P_k^- satisfies the Riccati equation, see Eq. (5.44):

$$K_k = P_k^- \tilde{C}^T (\tilde{C} P_k^- \tilde{C}^T + \sigma_k)^{-1}, \qquad\qquad P_0^- = P_{x_0}; \qquad (7.19)$$

$$\hat{\tilde{x}}_k = \hat{\tilde{x}}_k^- + K_k(\tilde{y}_k - \tilde{C}\hat{\tilde{x}}_k^-), \qquad\qquad \hat{\tilde{x}}_0^- = \bar{\tilde{x}}_0; \qquad (7.20)$$

$$P_k = (I - K_k \tilde{C}) P_k^- . \qquad (7.21)$$

The equations presented here can be found in any standard text on estimation, for
more information see [66, 95]. Fig. 7.2 highlights the recursive nature of the time-
varying Kalman filter algorithm. At each time instant k, the new measurement
$\tilde{y}_k = \bar{\Delta}_k$ and the measurement covariance σ_k are determined from equations
Eq. (7.14) and Eq. (7.15).

7.4 Control Implementation

As in the work presented in Chap. 6 we implemented the control scheme on a
dSpace DS1103 Power PC DSP Board. The dSpace board consists of 8 Digital-
to-Analog-Converter (DAC) and 16 Analog-to-Digital-Converter (ADC) chan-
nels with a sampling rate of 300 kHz. The board is fully programmable via
Matlab's Simulink toolbox and possesses a 16-bit resolution. The computational
results related to $\bar{S}_k$ were obtained via a C-program; the update rate is 10 kHz to
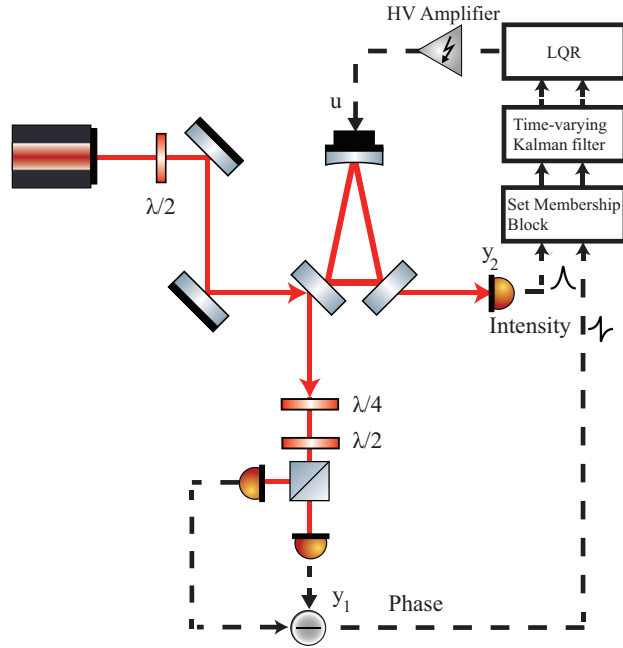
Figure 7.3: Schematic of the cavity locking experiment, including the combination of a time-varying Kalman filter and a linear quadratic regulator. The dashed lines depict electronic links.

guarantee a sufficient bandwidth. The result was a highly robust controller that successfully achieved frequency lock of the optical cavity to the laser from any initial operating point. While a twelfth-order polynomial is solved in the simulation [91], we chose to implement a simpler fourth-order model (third-order plant model and an additional integrator), which did not include mode-splitting. We were able to safely neglect mode-splitting, because the gradients of the error signals corresponding to the non-degenerate s/p-polarised cavity modes differ in sign, as shown in Fig. 7.4. Hence it is only possible to lock to one mode at a time; in our case we chose to lock to the p-polarisation. A schematic of the closed-loop system is depicted in Fig. 7.3.

7.5 Results

We validated the proposed controller by comparing its performance to a typical
PI controller, designed such that the gains of the two controllers and therefore
their residual frequency noise reductions were approximately equal when the
cavity was in lock. The resulting PI controller had a gain of

$$K_{PI}(s) = \frac{0.1s + 316.5}{s}. \tag{7.22}$$

We first set up an experiment to demonstrate the control performance in the lin-
ear region, where conventional controllers can successfully stabilise the cavity.
Then we demonstrated the superior operation of our control scheme in the non-
linear region where the PI controller fails.

We determined the quality and robustness of our locks by injecting a disturbance
in the form of a step function. For the resonant case the transmitted signal y_1
has its maximum value and the error signal y_2 varies around zero, in contrast
to the unlocked case where y_1 and y_2 are both close to zero, see Fig. 7.4. For
the first test we applied a step voltage to a PZT mounted to one of the cavity
mirrors for length control. The voltage step was 0.3 V, which drove the detuning
to the edge of the linear region. This disturbance was equivalent to a detuning of
≈ 32 MHz or $0.5\,\kappa$. Fig. 7.5 shows the influence of the input disturbance on the
plant locked with the PI controller. The PI controller reacquired lock after 0.14 s.
Fig. 7.6 highlights the response of our systematic control approach, which per-
formed much faster, reacquiring lock in just 0.03 s.

 For the second test we applied a step voltage of 0.4 V to the PZT. This drove
the detuning into the non-linear region, which is equivalent to a detuning of
≈ 43 MHz or $0.66\,\kappa$. As a result, the PI controller was unable to maintain/reac-
quire cavity lock as shown in Fig. 7.7. On the other hand, our proposed control
scheme reacquired lock in ≈ 35 ms as shown in Fig. 7.8. Fig. 7.9 illustrates the
transfer functions of the proposed controller at fixed instants of time after apply-
ing the step input of 0.4 V at $t = 0$ s. The controller transfer function varies in
time since it depends on the operating point of the system and therefore on the
estimate of the detuning. The evolution of the controller transfer function is the
reason why the time-varying Kalman filter is capable of handling the non-linear
regime. Note that the plots for $t = -5$ ms, where the system was in lock before
it was disturbed at $t = 0$ s, and $t = 35$ ms, where the system reacquired lock
overlap and describe the optimal controller for the plant on resonance.   When
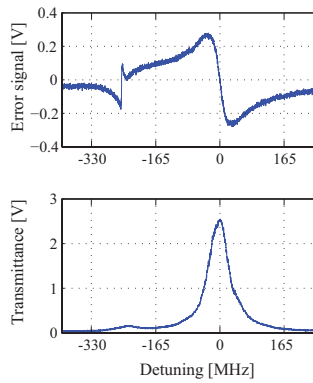
Figure 7.4: Frequency response of the optical cavity, showing the error signal from the homodyne detector y_1 (top) and the transmitted signal y_2 (bottom). The main Airy peak/error signal at $\Delta = 0$ MHz corresponds to the p-polarised cavity input, whereas the Airy peak/error signal at $\Delta \approx -230$ MHz belong to the s-polarised field utilised as local oscillator of our homodyne locking scheme.
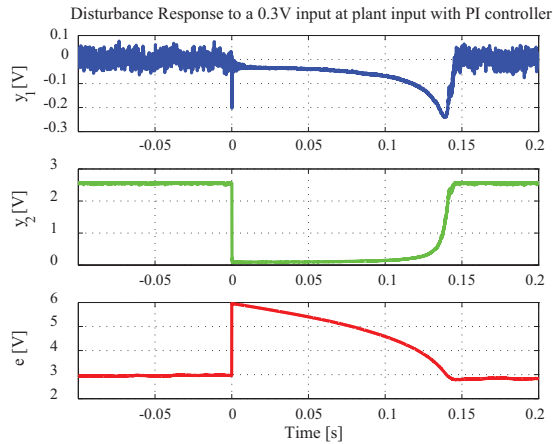
Figure 7.5: Response of optical system locked with a traditional proportional-
integral controller to an input disturbance step function of 0.3 V,
equivalent to a detuning $\Delta \approx 32$ MHz $\approx 0.5\kappa$. The PI controller
reacquires lock after 0.14 s.

the detuning is very large, the measured output is essentially white noise. Since
the augmented system integrates the white noise output, we obtain a Wiener pro-
cess for large detunings. The Wiener process describes a random walk ensuring
that the controller moves in a direction until $y1$ and $y2$ become significant.

7.6 Conclusion

We have successfully demonstrated the operation of our time-varying Kalman fil-
ter locking scheme, highlighting its ability to automatically reacquire cavity lock
– without scanning the frequency – in an automated way from any given operating
point. Our novel autolocking scheme successfully overcomes the inherent non-
linearity of the considered control problem. We utilised the singular perturbation
method to simplify the non-linear control problem to enable the implementation
of convenient linear control techniques. Compared to a traditional PI controller
our controller was able to reacquire lock in a significantly shorter time (0.03 s as
opposed to 0.14 s) while in the linear region. Furthermore we demonstrated that

Figure 7.6: Response of optical system locked with a time-varying Kalman filter to an input disturbance step function of $0.3\,\mathrm{V}$, equivalent to a detuning $\Delta \approx 32\,\mathrm{MHz} \approx 0.5\kappa$. Our controller reacquires lock after $0.03\,\mathrm{s}$ which is faster compared to the PI controller.

our autolocking scheme is capable of autonomously bringing the system back to resonance even in the presence of large disturbances, which cause the system to leave the linear region of the error signal, where linear time-invariant controllers fail. Our autolocking scheme significantly improved the robustness of the cavity lock and thereby increased the duty-cycle of the experiment. This superior performance of the feedback loop could be beneficial in a myriad of applications in fields such as spectroscopy [73, 74] or quantum information [75, 76].

Figure 7.7: Response of optical system locked with a proportional-integral controller to an input disturbance step function of 0.4 V, equivalent to a detuning $\Delta \approx 43\,\text{MHz} \approx 0.66\kappa$. The PI controller was not able to reacquire lock.
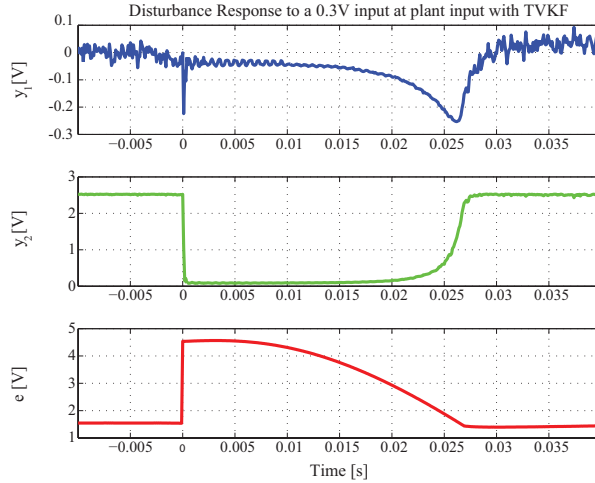
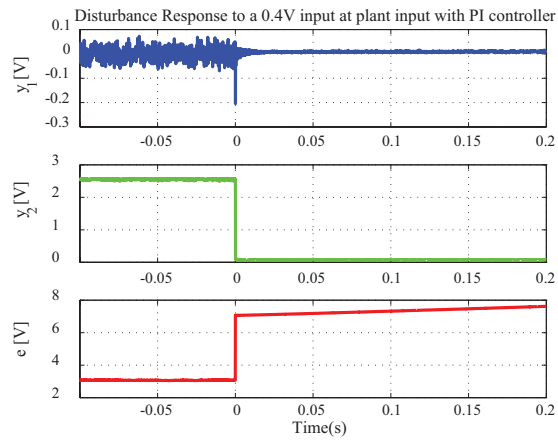Figure 7.8: Response of optical system locked with a time-varying Kalman filter
to an input disturbance step function of 0.4 V, equivalent to a detuning
$\Delta \approx 43\,\text{MHz} \approx 0.66\kappa$. Our control scheme reacquired lock after
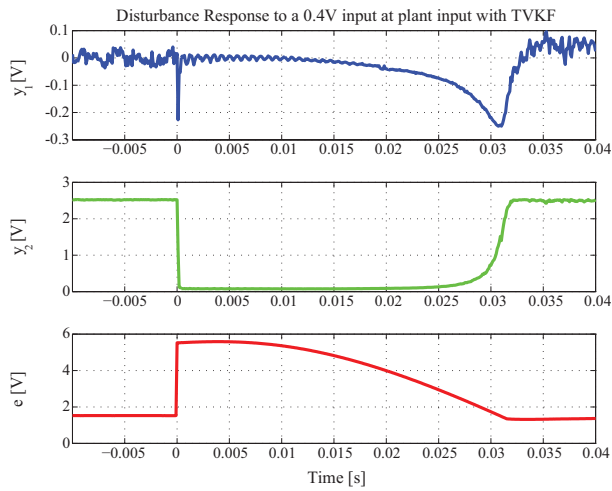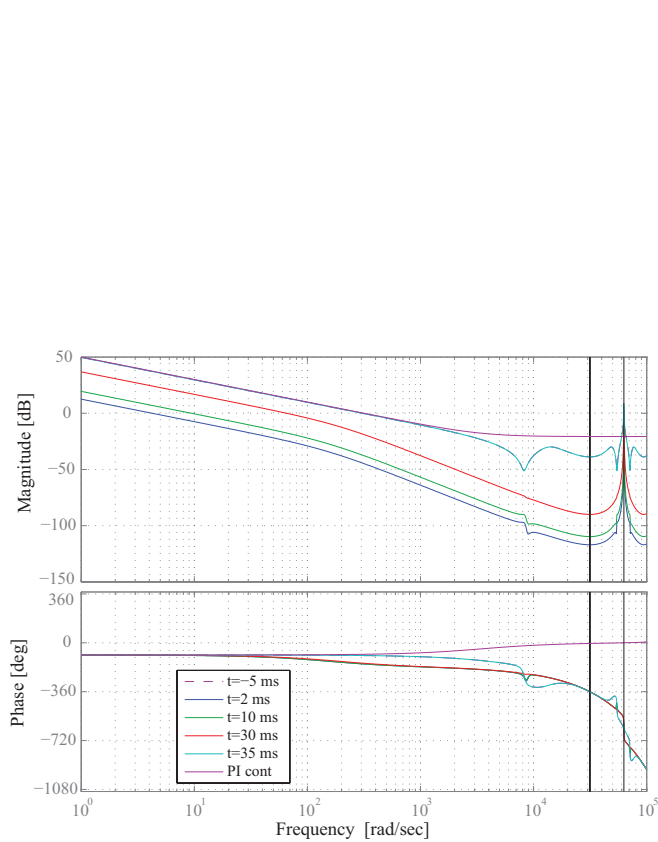35 ms, whereas the PI controller failed to relock the cavity.

Figure 7.9: The time-varying Kalman filter gives rise to a range of controllers at
various instants of time, after applying a 0.4 V step function distur-
bance at $t = 0$ s.

8

Control Investigations for a Squeezed Light Source

In 1981 Caves proposed that the injection of non-classical (in particular so-called *squeezed states* of light [96]) can improve the sensitivity of shot noise limited optical interferometers [24]. In 1985 Slusher *et al.* generated the first vacuum squeezed states [96] and 25 years later Vahlbruch *et al.* realised Cave's idea by injecting squeezed vacuum into the dark port of the GWD GEO600 [25, 97]. In order to ensure the required permanent injection of squeezed states a suitable control scheme is needed [98, 99].

In our laboratory we wanted to produce long-term stable, fixed quadrature squeezing for a high-precision spectroscopy experiment described and simulated in [100]. A control scheme consisting of two individual feedback loops achieved this requirement, where both loops applied PI control. The first feedback loop locked the optical cavity, which surrounded the non-linear medium to resonantly enhance the strength of the non-linear process. The second control loop stabilised the relative phase between the pump and intracavity field and therefore defined the squeezed quadrature. As the cavity lock also affects the relative phase between the two fields, the question arose if this cross-coupling would spoil the desired performance of our squeezed light source. We examined the question in regards to the possibility to describe the squeezed light source as a coupled MIMO system, whose performance could benefit from the implementation of modern control techniques.
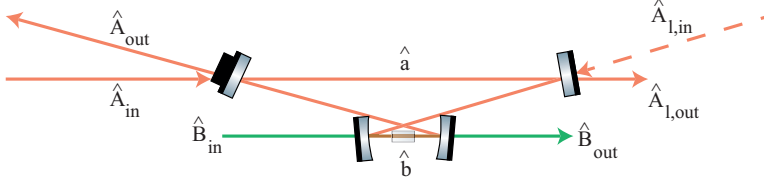
Figure 8.1: Bow-tie resonator including a $\chi^{(2)}$ medium. The schematic presents
all optical fields, which are required to derive the system dynamics.

8.1 Non-Linear $\chi^{(2)}$ Cavity Dynamics

We derive the cavity dynamics for a cavity enhanced squeezing process, see
Fig. 8.1, whereby the cavity is only resonant for the fundamental field A_{in}. The
pump field B_{in} passes the non-linear medium once. The Hamiltonian describing
the non-linear interaction is given by [34]

$$H = i\hbar\chi \left(\hat{b}^\dagger \hat{a}^2 - \hat{a}^{\dagger 2}\hat{b} \right), \tag{8.1}$$

where $\hat{a}, \hat{b}$ and $\hat{a}^\dagger, \hat{b}^\dagger$ are the annihilation and creation operators of the fundamen-
tal/pump field, respectively. χ denotes the coupling strength. Taking the cavity
dynamics (see Chap. 6) into account the equations of motion for the pump and
fundamental field are

$$\dot{\hat{a}} = -2\chi^{(2)}\hat{a}^\dagger\hat{b} - (\kappa_a + i\Delta_a)\hat{a} + \sqrt{2\kappa_A}\hat{A}_{in} + \sqrt{2\kappa_{l,a}}\hat{A}_{l,in}$$
$$\dot{\hat{b}} = \chi^{(2)}\hat{a}^2 - \kappa_b\hat{b} + \sqrt{2\kappa_B}\hat{B}_{in} + \sqrt{2\kappa_{l,b}}\hat{B}_l, \tag{8.2}$$

where κ_A and κ_B are the loss rates of the input mirrors for the input modes $\hat{A}_{in}$
and $\hat{B}_{in}$. $\kappa_{l,a}, \kappa_{l,b}$ denote the internal loss rates related to the loss modes $\hat{A}_{l,in}, B_l$
and κ_a, κ_b are the total loss rates related to the intracavity fields. Δ_a describes
the detuning of the cavity.
We assume an intense pump field which is undepleted by the interaction with
the dielectric medium. The undepleted case allows for the following substitution
$\hat{q} = 2\chi^{(2)}\hat{b}$, where $\hat{b}$ can be expressed in a linearised form of $\hat{b} = \beta e^{i\theta_b} + \delta b$ [34].

This leads to the restructured version of the cavity dynamics of interest

$$\dot{\hat{a}} = -(\kappa_a + i\Delta_a)\hat{a} - \hat{q}\hat{a}^\dagger + \sqrt{2\kappa_A}\hat{A}_{in} + \sqrt{2\kappa_{l,a}}\hat{A}_{l,in},$$

$$\dot{\hat{a}}^\dagger = -(\kappa_a - i\Delta_a)\hat{a}^\dagger - \hat{q}^\dagger\hat{a} + \sqrt{2\kappa_A}\hat{A}_{in}^\dagger + \sqrt{2\kappa_{l,a}}\hat{A}_{l,in}^\dagger. \tag{8.3}$$

Considering the linearisation $\hat{a} = \alpha + \delta a$ leads to the equations of motion for the mean field amplitudes

$$\dot{\alpha} = 0 = -(\kappa_a + i\Delta_a)\alpha - q\alpha^* + \sqrt{2\kappa_A}\alpha_{in} + \sqrt{2\kappa_{l,a}}\alpha_{l,in},$$

$$\dot{\alpha}^* = 0 = -(\kappa_a - i\Delta_a)\alpha^* - q^*\alpha + \sqrt{2\kappa_A}\alpha_{in}^* + \sqrt{2\kappa_{l,a}}\alpha_{l,in}^* \tag{8.4}$$

and fluctuation terms

$$\delta\dot{a} = -(\kappa_a + i\Delta_a)\delta a - \delta q\delta a^\dagger + \sqrt{2\kappa_A}\delta a_{in} + \sqrt{2\kappa_{l,a}}\delta a_{l,in},$$

$$\delta\dot{a}^\dagger = -(\kappa_a - i\Delta_a)\delta a^\dagger - \delta q^\dagger\delta a + \sqrt{2\kappa_A}\delta a_{in}^\dagger + \sqrt{2\kappa_{l,a}}\delta a_{l,in}^\dagger. \tag{8.5}$$

For the derivation of the output variance we need to convert the fluctuation terms to the Fourier domain $\text{FT}[da(t)/dt] = -i\omega\text{FT}[a](\omega)$, take the relations from Eq. 3.44 into account and use the boundary conditions defined in [101]

$$\sqrt{2\kappa_A}\hat{a} = \hat{A}_{out} + \hat{A}_{in},$$

$$\sqrt{2\kappa_A}\hat{a}^\dagger = \hat{A}_{out}^\dagger + \hat{A}_{in}^\dagger. \tag{8.6}$$

For the cavity on resonance $\Delta_a = 0$ and the above stated assumptions the amplitude/phase quadrature for $\delta\hat{A}_{out}$ can be expressed as

$$\delta\hat{X}_{A_{out}}^\pm = \frac{(2\kappa_A - \kappa_a - i\omega \pm |q|)\delta\hat{X}_{A_{in}}^\pm + 2\sqrt{\kappa_A\kappa_l}\delta\hat{X}_{A_l}^\pm}{\kappa_a + i\omega \mp |q|} \tag{8.7}$$

and the variance, see Chap. 3, which is the measure of interest for squeezing experiments becomes

$$V_{A_{out}}^\pm = \frac{\left((2\kappa_A - \kappa_a \pm |q|)^2 + \omega^2\right)V_{A_{in}}^\pm + 4\kappa_l\kappa_A V_{A_l}^\pm}{\kappa_a^2 + \omega^2 \mp |q|^2}. \tag{8.8}$$
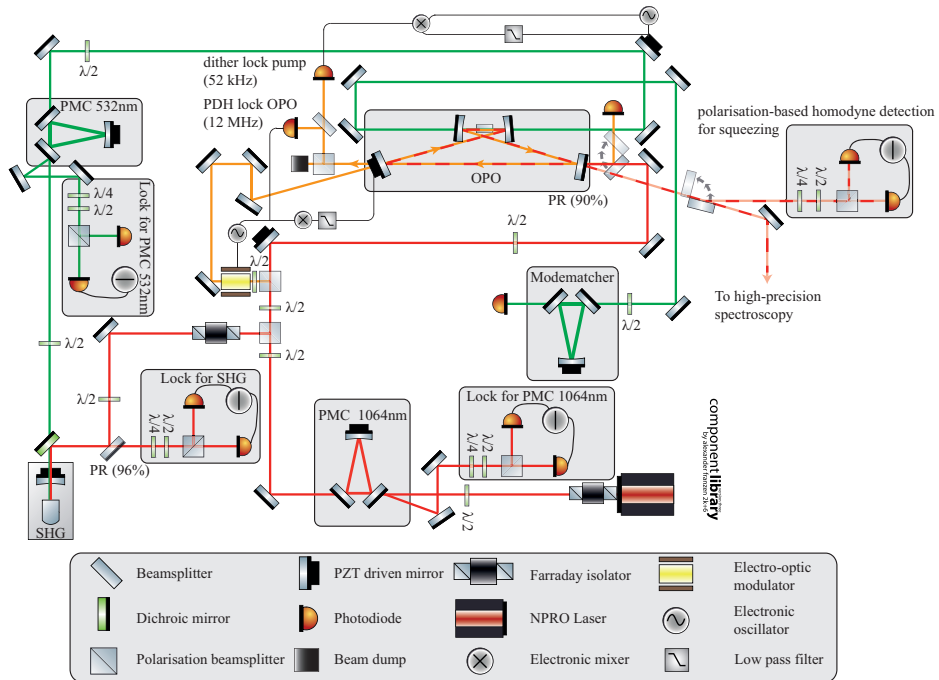
Figure 8.2: Experimental setup for the generation of cavity-enhanced squeezing.
The squeezed states were generated inside a sub-threshold bow-tie
OPO.

8.2 Generation of Squeezed Light

The experimental setup for the generation of cavity enhanced squeezing is pre-
sented in Fig. 8.2, where the main laser source was a continuous wave,
neodymium-doped yttrium aluminium garnet (Nd:YAG) laser at 1064 nm with
a maximal output of 2 W from Innolight GmbH [102]. The 532 nm pump field
driving the generation of squeezed states was obtained via type I phase-matched
SHG, which was realised by a hemilithic Fabry-Pérot resonator. Hereby the
curved rear of the non-linear crystal was used as a cavity mirror. The utilised
$\chi^{(2)}$ medium was magnesium oxide-doped lithium niobate (MgO:LiNbO$_3$), with
dimensions $2 \times 2.5 \times 7.5$ mm^3 and a phase matching temperature of $T \approx 67°$C.
The temperature controller assuring a constant temperature consisted of a neg-

Table 8.1: Parameters of the SHG.

Parameter	Value
Non-linear medium	MgO:LiNbO$_3$
Cavity length	40 mm
Finesse	76
Free spectral range	4.6 GHz
Spectral linewidth	65 MHz
Reflectivity of coupling mirror	92 %
Waist$_{1064}$	$\approx$40 μm

Table 8.2: Parameters of the OPO.

Parameter	Value
Non-linear Medium	PPKTP
Cavity length	1.52 m
Finesse	58
Free spectral range	197.4 MHz
Spectral linewidth	3.96 MHz
Reflectivity of coupling mirror	90 %
Waist$_{532}$	$\approx$18 μm

ative temperature coefficient (NTC) thermistor as the sensor and a Peltier element as the actuator. The Fabry-Pérot resonator was kept on resonance by the polarisation-based homodyne locking scheme [46]. Further details regarding the hemilithic SHG cavity provided by the Quantum Interferometry group of our institute can be found in Table 8.1. The generated 532 nm light field was directed through a modecleaner (MC) cavity, which acts as a polarisation and spatial mode filter. The MC provided a high quality fundamental transverse electromagnetic mode (TEM$_{00}$), which then was matched to the TEM$_{00}$ mode of the OPO, used as squeezed light source. The parameters of the sub-threshold bow-tie OPO, see Fig. 8.2, are given in Table 8.2. We utilised PPKTP as the $\chi^{(2)}$ medium, with dimensions $1 \times 2 \times 10$ mm^3. The required temperature for

the generation of squeezed states with quasi-phase matching was $\approx 30°$C. It was
again stabilised by the combination of a NTC thermistor and a Peltier element.
For a detailed characterisation of the bow-tie OPO we locked the optical cavity
via polarisation-based homodyne detection [46] and blocked the beam path to
the PDH PD. The front light field, which impinged on the partially reflective
coupling mirror had a ratio of 3:100 between the s/p-polarisation, which defined
the signal/local oscillator field, respectively. The ratio slightly differed from the
1:100 ratio, given by a *rule of thumb*, which shall ensure a non-varying shot
noise level, since we needed to increase the error signal for the OPO lock. As ex-
plained in Chap. 3, the polarisation-based homodyne locking scheme performs a
phase-sensitive measurement, thus we read out the phase quadrature. We locked
the relative phase between pump and intracavity field with the help of the dither
locking technique [103]. Hereby the PZT driven mirror placed in the beam path
of the pump field was used as a phase actuator and the applied modulation fre-
quency for the dither lock was $f = 52$ kHz. All feedback loops were realised by
traditional PI control.

The variance of the phase quadrature was acquired with a signal analyser (Ag-
ilent MXA N9020A). The resolution/video bandwidths of the signal analyser
were 1.5 MHz and 91 Hz, respectively, the sweep time was 1.8 s, the averaging
factor was 10 and the internal attenuation was 6 dB. The results of a span mea-
surement are presented in Fig. 8.3. With a pump power of 68 mW, we were
able to observe antisqueezing/squeezing values of 3.78/1.96 dB, respectively. A
zerospan measurement at the first $\mathrm{FSR} = 197.4$ MHz demonstrated that (OPO
in lock) we were able to lock the pump to the maxima/minima of its sweep
which corresponds to antisqueezing/squeezing, respectively. This result demon-
strates the realisation of stable squeezing of a fixed quadrature. We needed to
determine the total losses $\eta_{\mathrm{total}} = 0.5$ of our setup to verify our detected anti-
squeezing/squeezing values [104, 105]. η_{total} is the product of the propagation
efficiency $\eta_{\mathrm{prop}} = 0.92$, the homodyne visibility $\eta_{\mathrm{vis}} = 0.64$, the quantum effi-
ciency of the photodiodes (Perkin Elmer C30617) $\eta_{PD} = 0.98$ and the escape
efficiency $\eta_{\mathrm{esc}} = 0.85$. Fig. 8.5 compares the measured antisqueezing/squeezing
values, which depend on the pump power with a simulated model [104, 105]

$$R_{\pm} = 1 \pm \eta_{\mathrm{total}} \frac{4x}{(1 \mp x)^2 + 4\Omega^2}, \tag{8.9}$$

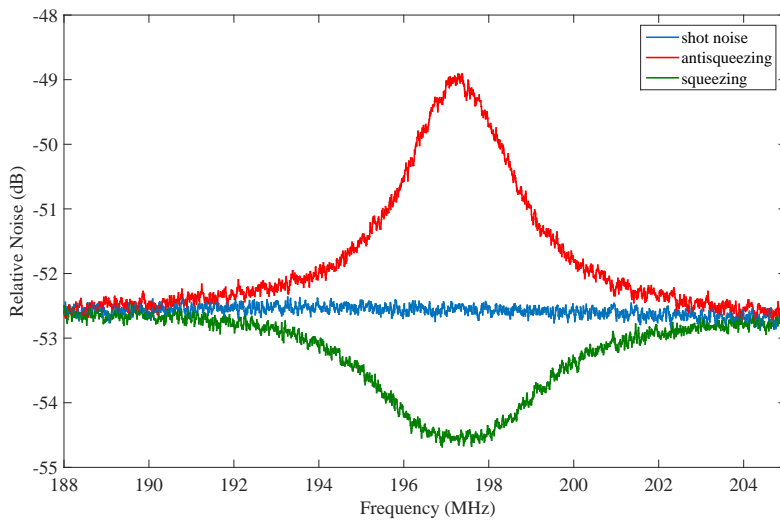$$V_{A_{out}}^{\pm} = 10\log_{10}(R_{\pm}), \tag{8.10}$$

Figure 8.3: We observed antisqueezing/squeezing values of 3.78/1.96 dB for a pump power of 68 mW relative to the shot noise (blue). The measured data shows the frequency-dependence of cavity enhanced antisqueezing/squeezing (orange/yellow), which is directly related to the resonance condition of the optical cavity.
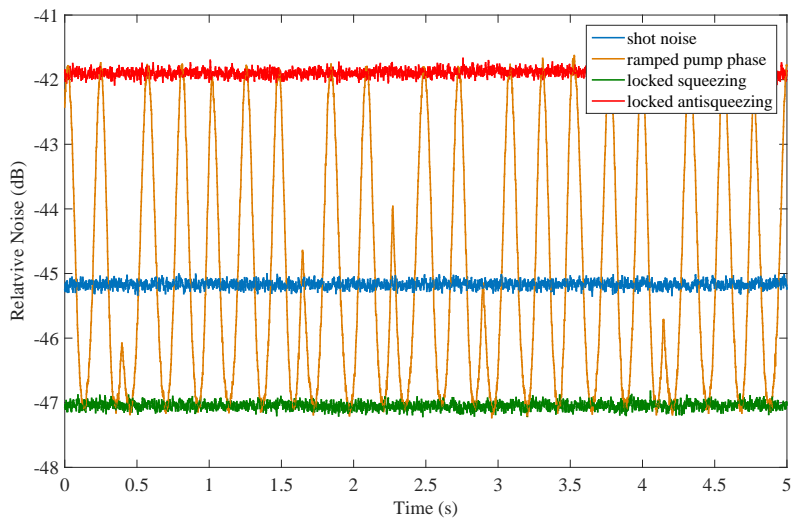
Figure 8.4: A zerospan measurement at the first FSR $= 197.4\,MHz$ demonstrated that we were able to lock the pump field to the maxima/minima of its sweep (orange) which corresponds to antisqueezing/squeezing (purple/yellow), respectively. These results demonstrated the realisation of stable squeezing of a fixed quadrature.
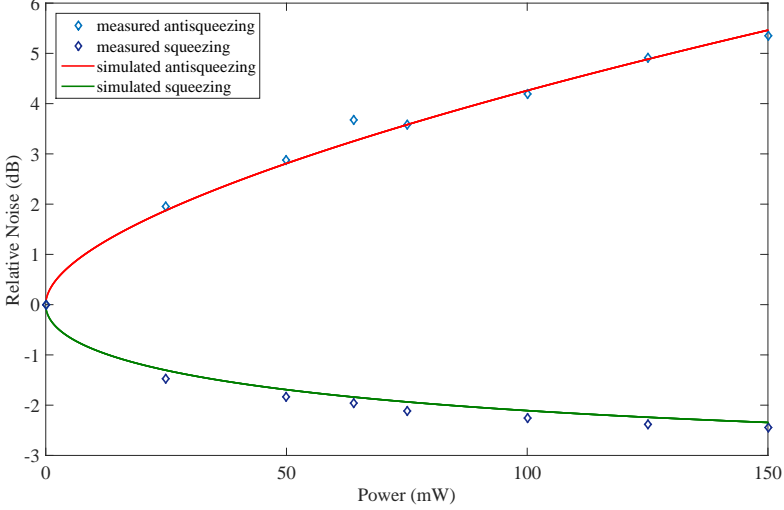
Figure 8.5: Comparison between power-dependent antisqueezing/squeezing values and a fitted model Eq. (8.10).

where Ω describes the detuning of the cavity and $x = \sqrt{P_{th}/P}$ is the normalised pump power with the pump threshold P_{th} and the pump power P. Fig. 8.5 highlights the good agreement between experiment and model.

After the characterisation of the squeezed light source we changed the experimental setup, since the squeezed output should be utilised for high-precision spectroscopy described in [100]. We kept the dither lock of the pump phase, but replaced the polarisation-based homodyne locking scheme by a PDH scheme, whereas the s-polarised control light field was coupled into the cavity from its rear plane mirror and was co-propagating with the squeezed output. The modulation frequency of the PDH scheme was $f = 12\,\text{MHz}$. For the detection of squeezed states we set up the polarisation-based homodyne detection scheme with an external LO. The external LO was given by a p-polarised light field, which impinged on the coupling mirror of the bow-tie OPO and was directly reflected, since the p-polarisation was non-resonant. The relative phase between LO and squeezed output could be varied by a PZT driven mirror. It is worth mentioning that this homodyne detection scheme can observe both quadratures, but it can only be locked to the phase quadrature.

8.3 Control Problem and Conclusions

We investigated the control scheme of our squeezer, which should generate stable, fixed quadrature squeezing, as a potential MIMO control problem. A MIMO problem is present, if the output of one feedback control loop has an impact on the other control loop. In our case, we characterised the influence of the cavity lock on the pump lock and vice versa. The result was that the two feedback loops are completely decoupled, due to the utilised modulation schemes. A disturbance injected by one of the considered control loops is frequency shifted to higher frequencies by the demodulation stage of the other feedback loop. The resulting up-shifted frequency part is well above the unity gain frequency and has therefore no impact on the performance of the feedback loop. Even more important is that the relation between the injected disturbance x and the frequency-shifted signal y is not linear. There is no meaningful TF $G(s) = y(s)/x(s)$ and thus linear control techniques can not be applied. To conclude, we can state that the two control loops can be seen as two decoupled SISO systems.

It is possible to extend the control problem by adding a third variable, given by the feedback loop, which controls the phase of the LO and thereby defines the detection angle of the HD. The consideration of the LO lock can be sensible for a detailed investigation of phase fluctuations $\tilde{\theta}$ caused by the two other locks, which would degrade the squeezing strength [104, 106]

$$R'_{\pm} \approx R_{\pm} \cos^2(\tilde{\theta}) + R_{\mp} \sin^2(\tilde{\theta}). \tag{8.11}$$

Another sensible case including the LO lock is given by experiments trying to measure small signals via a homodyne detection scheme, since these signals would be amplified by the strong LO. Due to these examples, we investigated the case including our LO lock. Although we did not need a highly stable LO lock at that moment, these investigations point out options for future experiments.

In analogy to the first investigations, we were able to directly state that a disturbance injected by the LO feedback loop has no impact on the dither and cavity control loops, because of the implemented modulation schemes. However disturbances injected by the other two feedback loops had an impact on the LO locking loop, which is realised via a modulation-free, polarisation-based homodyne detection scheme. Firstly a disturbance injected by the OPO lock directly affects the relative phase between the squeezed output and the LO, which is explainable by the phase response of a cavity with respect to detuning, induced by the disturbance. Secondly a disturbance injected by the dither lock, where the actuator of
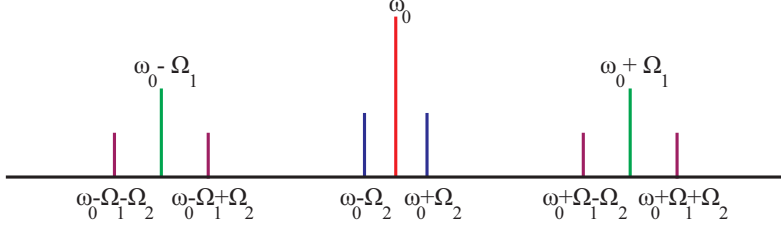
Figure 8.6: Spectrum of a twice modulated carrier light field, with $\Omega_1 > \Omega_2$. The spectrum demonstrates that a disturbance at Ω_2 is preserved.

the control loop also acts as the phase modulator, can be expressed as sidebands of sidebands related to a electromagnetic field $E_{in} = E_0 e^{i\omega_0 t}$ [107]

$$E_{out} = E_0 e^{i\omega_0 t} e^{im_1 \cos \Omega_1 t + \varphi_1} e^{im_2 \cos \Omega_2 t + \varphi_2}, \qquad (8.12)$$

where $m_{1,2}$ are the modulation indices, $\varphi_{1,2}$ the modulation phases and $\Omega_{1,2}$ the modulation frequencies. Ω_1 denotes the dither modulation frequency and Ω_2 denotes a disturbance with this specific frequency. Expanding Eq. 8.12 allowed for a frequency analysis of E_{out}

$$\begin{aligned}
E_{out} = \sum_{n=0}^{N} a_n e^{i\omega_n t} = E_0 \bigg[& e^{i\omega_0 t} + \frac{im_1}{2} \left(e^{(i\omega_0 + \Omega_1)t} + e^{(i\omega_0 - \Omega_1)t} \right) \\
& + \frac{im_2}{2} \left(e^{(i\omega_0 + \Omega_2)t} + e^{(i\omega_0 - \Omega_2)t} \right) \\
& - \frac{m_1 m_2}{4} \left(e^{(i\omega_0 + \Omega_1 + \Omega_2)t} + e^{(i\omega_0 - \Omega_1 + \Omega_2)t} + e^{(i\omega_0 - \Omega_1 + \Omega_2)t} \right. \\
& \left. + e^{(i\omega_0 - \Omega_1 - \Omega_2)t} \right) \bigg]
\end{aligned} \qquad (8.13)$$

With the help of this frequency analysis, illustrated in Fig. 8.6, it was evident that a disturbance at Ω_2 would have an impact on the LO feedback loop and that we would be able to characterise the system via transfer functions, since the disturbance at Ω_2 is preserved.

These non-vanishing coupling terms lead to the fact, that the control of a squeezer, including feedback loops for the OPO, the pump and the LO, can be described as a MIMO control problem. Although we did not implement a MIMO

control scheme, it is important to recognise that the control scheme of a squeezer
can be improved and benefit from a suitable modern control approach, which
is inherently capable of handling the unwanted coupling terms, if needed in the
future.

9

Local Control of a Triple Pendulum Suspension

Earthbound interferometric gravitational wave detectors need to isolate their optical components from seismic noise to reach their desired sensitivity. Without a seismic isolation system, seismic noise would limit the capability of detecting elusive signals like gravitational waves. Usually this isolation is realised by suspended optics, where the optical component can be seen as an end mass of a pendulum. The frequency response of such a driven, damped harmonic oscillator rolls of with $1/f^2$ above its resonance. This suppression of $1/f^2$ is not sufficient, which is why state-of-the-art GWDs utilise triple/quadruple pendulum suspensions reaching a suppression of $1/f^6$ or $1/f^8$ above their resonances, respectively. However on resonance the root mean square (RMS) motion of the lower test mass (end mass) is excited. Due to this RMS motion enhancement triple pendulum suspensions require active control loops, damping the pendulum eigenmodes of each degree of freedom (DOF). The damping of the pendulum resonances is known as *local control* and needs to be distinguished from *global control*, which describes the feedback loops keeping the interferometer at its required operating point. The multiple input multiple output (MIMO) local control problem is usually addressed by traditional control approaches, whereas the system transfer functions, used for the control design, have been measured from co-located sensor/actuator pairs on the upper stage of the suspension. However, the limitation of this approach is the lack of direct information about the end

mass motion, which needs to be minimised. That's why we directly measured
the motion of the lower test mass with respect to an excitation injected at the
upper mass. It is noteworthy that we operated the system in the small displace-
ment regime, assuming that linearised models are able to accurately describe the
system. With the help of the obtained frequency response data we introduce a
host of modern control tools potentially enhancing the performance of the sus-
pension system. The advantage of a systematic control approach is its capability
of dealing with inherent cross-correlations of the triple pendulum suspension. It
is therefore suitable for controlling a complex MIMO system.

9.1 Harmonic Oscillator

The theoretical concept of why suspended optics are suitable as seismic isolation
systems is based on the frequency response of a one dimensional, driven, damped
harmonic oscillator given in the time domain by

$$m\ddot{x}(t) + 2m\gamma\dot{x}(t) + kx(t) = F_{ext}(t). \tag{9.1}$$

Here m denotes the mass, k the spring constant, γ the damping factor, which is
proportional to the velocity $\dot{x}(t)$ and F_{ext} the external force acting on the system
[108]. Taking the Fourier transform of $x(t)$

$$X(\omega) = \frac{1}{\sqrt{2\pi}} \int_0^\infty x(t)e^{-i\omega t}dt \tag{9.2}$$

and the relation

$$(i\omega)^n X(\omega) = \frac{1}{\sqrt{2\pi}} \int_0^\infty \frac{\delta^n x(t)}{\delta t^n}e^{-i\omega t}dt \tag{9.3}$$

into account results in the frequency domain expression of the driven, damped
harmonic oscillator

$$m\left(2i\gamma\omega + \omega_0^2 - \omega^2\right) X(\omega) = F_{ext}(\omega), \tag{9.4}$$

with ω the angular frequency and $\omega_0 = \sqrt{k/m}$ the resonance frequency of the
oscillator. Rearranging Eq. (9.4) results in a transfer function, which frequency-
dependently describes how the oscillator is displaced by an external force

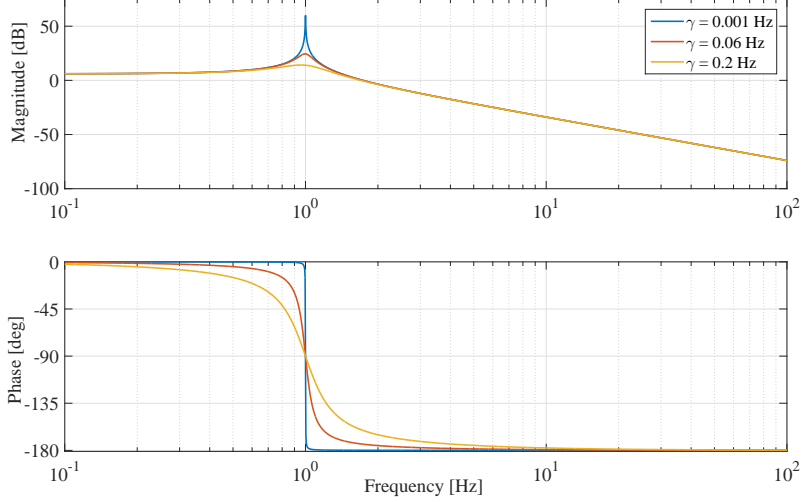$$G(i\omega) = \frac{X(\omega)}{F_{ext}(\omega)}. \tag{9.5}$$

Figure 9.1: Bode plot for a driven, damped harmonic oscillator with varying damping factors γ and a resonance frequency $f_0 = 1\,\mathrm{Hz}$.

Gain and phase of the transfer function G(s) are given by

$$|G(i\omega)| = \frac{1}{m\sqrt{\left(\omega_0^2 - \omega^2\right)^2 + (2\gamma\omega)^2}}, \tag{9.6}$$

$$\varphi(\omega) = \arctan\left(\frac{2\omega\gamma}{\omega_0^2 - \omega^2}\right) \tag{9.7}$$

and shown for a varying γ and a resonance frequency $f_0 = 1\,\mathrm{Hz}$ in Fig. 9.1. Fig. 9.1 highlights that for frequencies $f < f_0$ the system shows a constant response to an external force, whereas on resonance the system response is increased significantly and the phase of the system drops by $180°$. The damping factor γ effects the magnitude of the system response, the steepness of the phase loss and therefore the FWHM Δf of the resonance used to define the quality Q for harmonic oscillators $Q = f_0/\Delta f$. For frequencies above the resonance the external force is suppressed by a factor $1/f^2$, pointing out that seismic isolation can be realised by harmonic oscillators. If the suppression factor of $1/f^2$ is not sufficient, it can be enhanced by cascading multiple harmonic oscillators. Regarding Eq. (5.6) n-cascaded harmonic oscillators result in a suppression factor
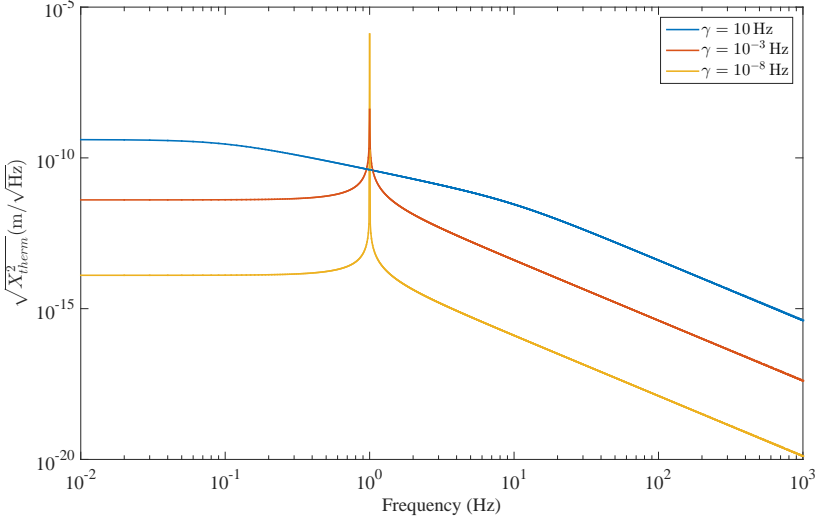
Figure 9.2: Amplitude spectral densities of a harmonic oscillator for various γ
and $T = 296\,\mathrm{K}$, $m = 1\,\mathrm{kg}$ and $f_0 = 1\,\mathrm{Hz}$.

of $1/f^{2n}$ above the nth resonance.

Avoiding an increased RMS motion of the harmonic oscillators requires active
damping of their eigenmodes and cannot be achieved by increased damping fac-
tors γ. The reason for this is given by the fluctuation-dissipation theorem with
an associated power spectrum of the system's fluctuating motion [109]

$$X^2_{therm} = \frac{4k_B T \gamma}{m\left(\omega_0^2 - \omega\right)^2 + \gamma^2 \omega^2}, \tag{9.8}$$

where k_B is the Boltzmann constant and T the temperature. The amplitude spec-
tral densities $\sqrt{X^2_{therm}}(\omega)$ of the motion of a single harmonic oscillator for var-
ious γ is shown in Fig. 9.2 with $T = 296\,\mathrm{K}$, $m = 1\,\mathrm{kg}$ and $f_0 = 1\,\mathrm{Hz}$. The
simulation shown in Fig. 9.2 demonstrates that an increased damping factor γ
results in a broadband increase of the amplitude spectral density $\sqrt{X^2_{therm}}(\omega)$
of the motion of the harmonic oscillator. The energy of the resonance dissipates
into the system and thereby decreases the sensitivity. To evade this sensitivity
limit small damping factors are desired, resulting in an enhancement of RMS
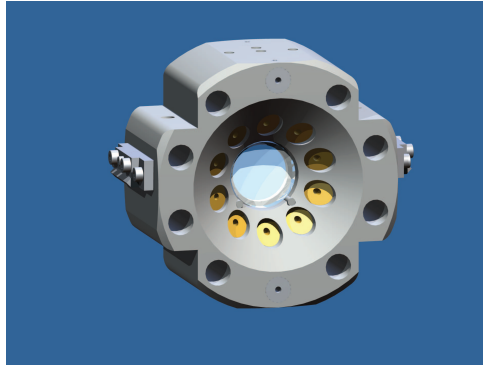
Figure 9.3: Modified lower mass of the suspension.

motion on resonance, which can be suppressed by active damping extracting energy from the system.

9.2 Characterisation of a Triple Pendulum Suspension

We characterised a triple pendulum suspension by transfer functions, measuring the motion of the upper (top-top) and lower (top-bottom) test mass with respect to an excited motion of the upper mass. We wanted to augment the commonly used top-top measurements with direct information about lower mass motion to enable a host of systematic control approaches to enhance the performance of the system. Our investigated triple pendulum suspension is almost identical with the suspension used for the 10 m prototype [110] reference cavity, see Fig. 9.4, and its design was inspired by the suspension system for the GEO600 mode cleaner [111]. The only difference between our setup and the 10 m prototype setup was the lower test mass. Instead of a low loss Suprasil 2 Grade mirror, we utilised a compound aluminium/brass structure with a highly reflective mirror ($\oslash = 1$ inch) in its centre, see Fig. 9.3. Our end mass had the same mass and moments of inertia as the original end mass to guarantee an identical performance of the suspension, but at significantly lower cost, and offering increased variability. The important design parameters of the triple pendulum suspension are shown in

Table 9.1: Parameters of the reference cavity suspension [112].

Parameter	Value
Total length	774.2 mm
Total mass	2714 g
Upper mass	995 g
Intermediate mass	873 g
Lower mass	846 g
Wire diameter upper stage	152.4 μm
Wire diameter intermediate stage	101.6 μm
Wire diameter lower stage	55.2 μm

Table 9.1, and Fig. 9.4 presents a schematic of our system. The triple pendulum suspension provided two vertical isolation stages. The first was given by two cantilevers located at the top of a cage and holding the upper mass. The second stage was built into the upper mass. It is noteworthy that the centre of mass of the lowest mass was not identical with its suspension point. This was desired to ensure a suitable restoring force, although it introduces coupling between modes. The interested reader is referred to [112] for a detailed description of the design process of the reference cavity suspensions.

9.3 Degrees of Freedom

There are six degrees of freedom for a rigid body, see Fig. 9.5. In the case of suspended optics, these correspond to

- Longitudinal: Parallel mirror motion with respect to the optical axis.

- Sideways: Horizontal motion with respect to the optical path.

- Vertical: Vertical motion with respect to the optical axis.

- Yaw: Rotation around the vertical axis.

- Pitch: Rotation around the sideways axis.

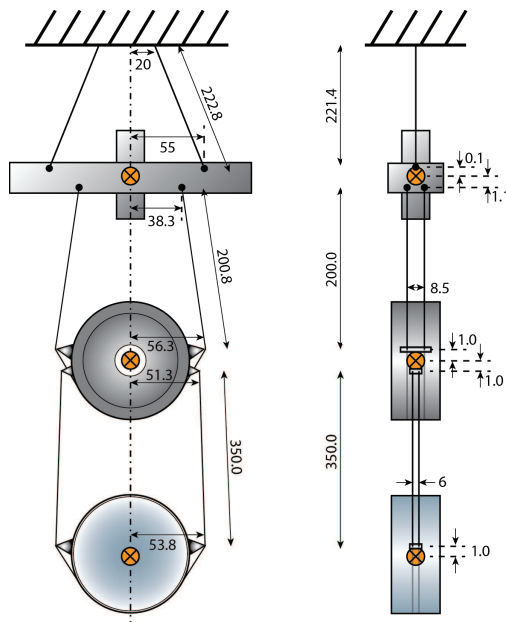- Roll: Rotation around the longitudinal axis.

Figure 9.4: Technical drawing of the triple pendulum suspension including dimensions. The upper mass is attached to cantilevers at the top, which provide a vertical isolation stage. A second vertical isolation stage is located inside the upper mass. The centre of mass of the lower mass is not identical with the suspension point, which is desired to ensure a suitable restoring force, although it introduces coupling between modes.
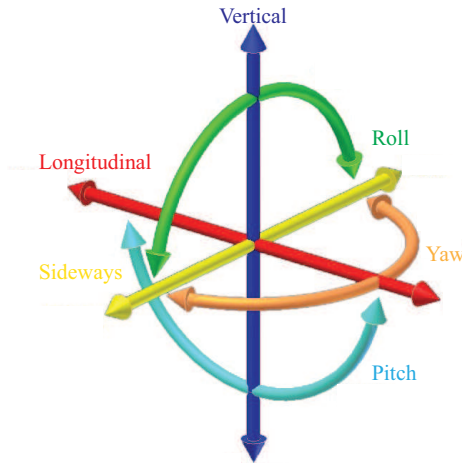
Figure 9.5: Six degrees of freedom for a rigid body.

The DOFs are usually not decoupled from each other, introducing
cross-correlations, which are inherently addressed by a modern control approach.
This is a significant advantage of modern control techniques in comparison to
traditional control, where the coupling terms need to be addressed individually
leading to an increased complexity of the control scheme.

9.4 Co-located Sensor/Actuator

Six co-located sensor/actuator pairs at the upper mass were used to damp and
read out the eigenmodes of the suspension system. The sensor/actuator pairs are
known as Birmingham Optical Sensor and Electro-Magnetic actuators (BOSEMs)
[113], see Fig. 9.6 [114]. A BOSEM consists of a light-emitting diode (LED),
whose light field is collimated by two lenses before it propagates through an
aperture. This aperture creates a flat-top beam needed to ensure that the detected
intensity is linearly dependent on the position of the flag. The magnetic flag is
attached to the upper mass, which allows for sensing its motion, since a chang-
ing position directly affects the detected intensity. The position of the flag can
be changed by the coil actuator, which generates a magnetic field acting on the
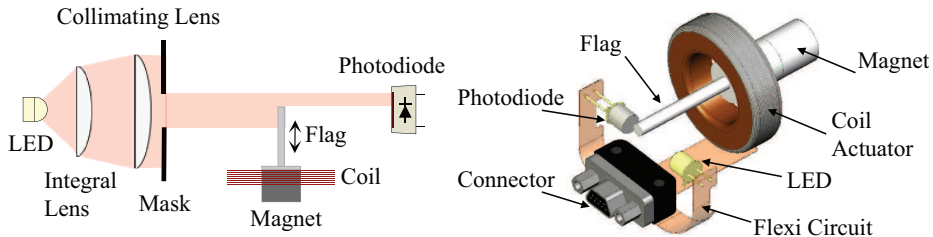
Figure 9.6: The assembly and functionality of a BOSEM consists of a LED, whose light is converted into a flat-top beam by the combination of two lenses and an aperture. The detected intensity is proportional to the position of the magnetic flag, attached to the upper mass. The position of the flag/upper mass can be controlled by a coil actuator, which generates a magnetic field acting on the flag [114].

magnetic flag. The direction of the actuation depends on the sign of the voltage applied to the coils. Since the BOSEM assembly is able to sense and act on the upper mass motion, it provides a suitable sensor/actuator pair for active damping of the system's resonances. To enable the implementation of linear control techniques, the output voltage of the PD must be linearly dependent on the flag position. We tested this requirement by mounting the flag onto a micrometer table and shifting it through the beam path. The results are shown in Fig. 9.7 and demonstrated that the normalised voltage curve of all six BOSEMs exhibited a wide linear range. The slopes of all curves were identical, meaning that the system responses of the BOSEMs were identical and that there was no need for additional scaling factors. The rest position ($0\,\text{mm}$) was set to 50% of the maximum voltage to maximise the dynamic range of the system.

Another requirement to guarantee a linear behaviour of the system was that the magnetic force of the coil acting on the flag is position independent. The fulfilment of this requirement was shown via a Mathematica script written by Mark Barton [115]. The script demonstrated that the force reaches a maximum for given geometry parameters of coil and flag with respect to the distance between the centres of coil and magnet. The maximum is the desirable operating point,
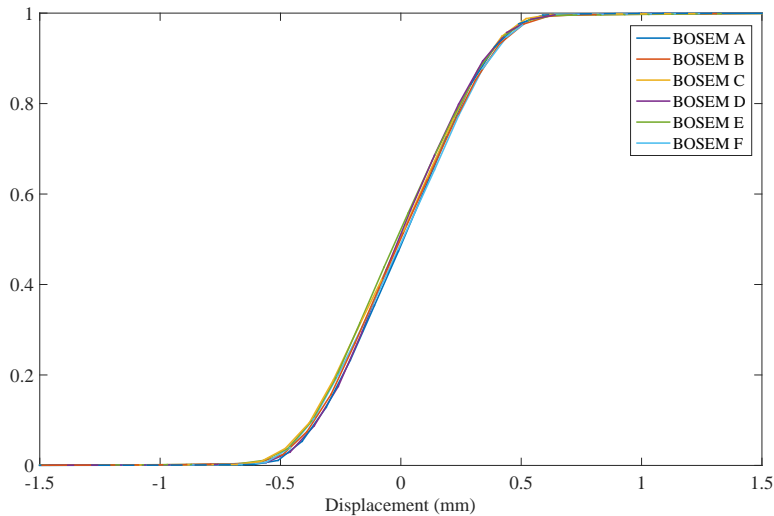
Figure 9.7: Normalised voltage response of all six BOSEM PDs with respect to
flag displacement.

since the force becomes position independent, considering a linear approxima-
tion. The simulation results of [115] are shown in Fig. 9.8 and were verified by
[113], where a detailed BOSEM design study and characterisation can be found.
Furthermore the utilised custom made BOSEM driver/readout electronic, which
satisfies the noise requirements of the 10 m prototype reference cavity, were pro-
vided by the 10 m prototype group and designed by Tobias Westphal [112].

9.5 Optical Levers

The results presented in [113] show that BOSEMs are suitable actuators/sensors
for linear systems. Furthermore our modern control approach should incorpo-
rate the frequency-dependent motion of the lower mass as well. For this reason
we set up two optical levers measuring the lower mass motion for three DOFs
with respect to an excitation injected via the designated BOSEMs [116]. We
decided to measure only yaw, pitch and longitudinal motion, since these DOFs
strongly disturb the output of interferometric measurements with respect to the
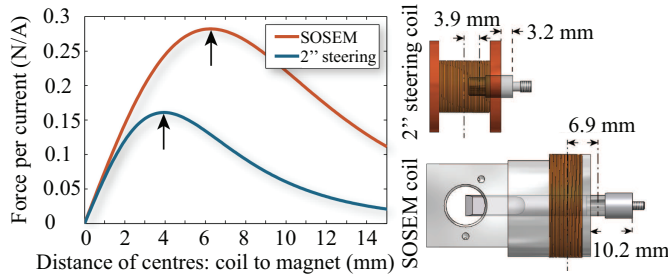
Figure 9.8: Desirable operating point for the coil/magnetic flag assembly, which is given by the maximum force (taken from [115]). The maximum describes the point where the force becomes approximately position independent.

other DOFs. The three other DOFs describe motions which are perpendicular to the optical axis and therefore theoretically don't disturb the output of the interferometer. Realistically a generic coupling factor of 1:1000 can be assumed. The optical levers consisted of collimated laser beams, required to ensure a linear system response by avoiding motion-dependent beam size variations. The incident laser beams impinged on the mirror of the end mass under angles $\theta_{1,2}$ and got reflected. Two quadrant photodiodes (QPD$_{1,2}$) at a distance of $l_{1,2}$ detected the light and the measured data was used to compute the actual lower mass motion of the considered DOFs. A schematic of this setup is shown in Fig. 9.9.

9.5.1 Signal Processing of QPD Signals

A quadrant photodiode consists of four photosensitive areas (A-D) and is schematically illustrated in Fig. 9.10. The location of an impinging laser beam can be calculated by

$$x = \frac{(I_B + I_D) - (I_A + I_C)}{I_{\text{total}}} \qquad \text{and} \qquad (9.9)$$

$$y = \frac{(I_B + I_A) - (I_D + I_C)}{I_{\text{total}}}, \qquad \text{where} \qquad (9.10)$$

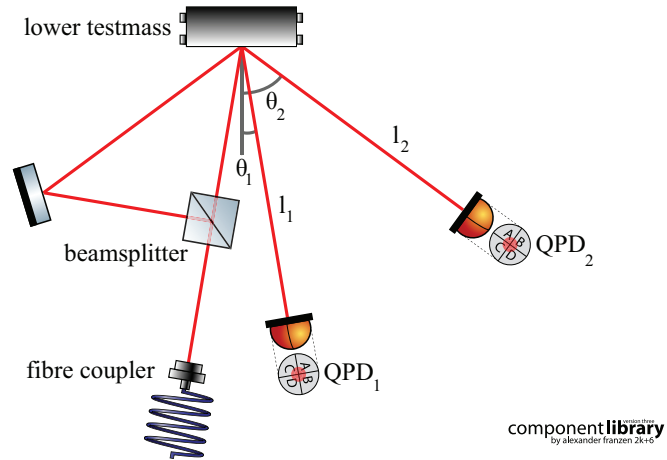$$I_{total} = I_A + I_B + I_C + I_D. \qquad (9.11)$$

Figure 9.9: Schematic of the two optical levers consisting of two collimated laser
beams, which impinge with angles $\theta_{1,2}$ on the lower test mass. The
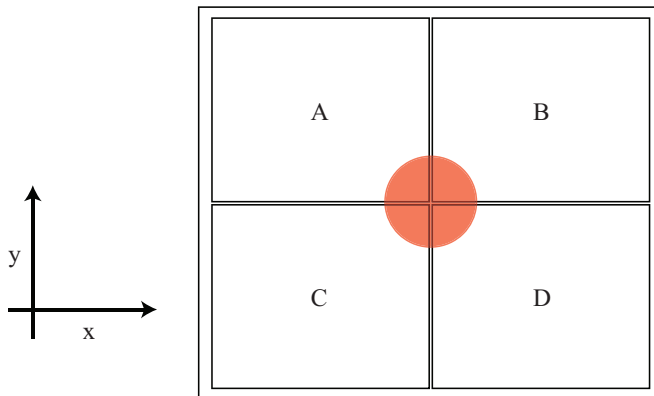reflected beams are detected by $QPD_{1,2}$ at a distance $l_{1,2}$.

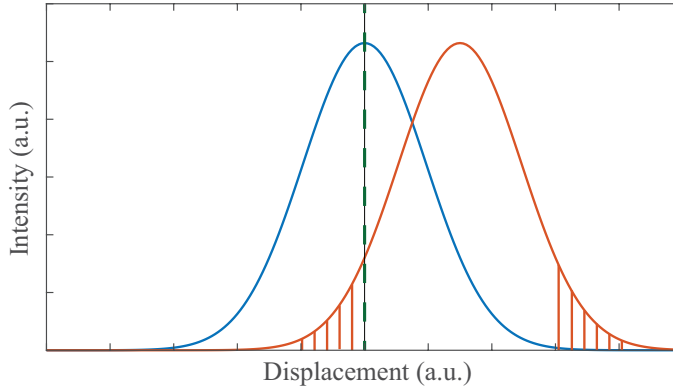Figure 9.10: Schematic of a QPD consisting of four photosensitive areas.

Figure 9.11: The dashed line defines the border between left $L = A + C$ and right $R = B + D$ halves of the QPD. The orange Gaussian profile is displaced by Δx with respect to the centred blue Gaussian profile.

The differences between the detected intensities I_{A-D} of the left and right halves or upper and lower halves determine the beam position for x/y, respectively. The normalisation factor I_{total} is needed to eliminate the influence of intensity fluctuations. To determine the exact position of the laser beam, we needed to take a Gaussian beam profile into account. We derived the intensity values $I(\Delta x)$ for a displacement Δx of the beam along the x-axis. For reasons of simplicity we neglected the $18\,\mu$m gap between the photosensitive areas [117]. This is a reasonable assumption as the beam spot size is always much larger than the size of the gap. Fig. 9.11 illustrates the considered problem, where the orange Gaussian beam is displaced with respect to the centred blue Gaussian. It is sufficient to consider only the left $L = A + C$ and right $R = B + D$ halves of the QPD to calculate a displacement along the x-axis. The total detected intensity of a Gaussian beam is given by

$$I_{total} = I_0\left(w(z)\right) \int_{-\infty}^{\infty} e^{\frac{r}{w(z)}} \, dr = I_0 \sqrt{\frac{\pi}{2}} w_0, \tag{9.12}$$

with $w(z) = w_0$, since the laser beam is collimated. The intensity difference between the left/right halves of the QPD introduced by a Δx displacement of the

laser beam can be expressed as

$$
I_{L-R} = I_0 \int_{-\infty}^{\infty} e^{\frac{r}{w_0} - \frac{\Delta x}{w_0}} dr - 2I_0 \int_{-\infty}^{0} e^{\frac{r}{w_0} - \frac{\Delta x}{w_0}} dr
$$

$$
= I_{total} - 2\, I_0 \underbrace{\int_{-\infty}^{0} e^{\frac{r}{w_0} - \frac{\Delta x}{w_0}} dr}_{\text{orange hatched area}} \tag{9.13}
$$

$$
\frac{I_{L-R}}{I_{total}} = 1 - \mathrm{erfc}\left(\frac{\Delta x \sqrt{2}}{w_0}\right) = I(\Delta x), \tag{9.14}
$$

with erfc the complementary error function. For reasons of symmetry the hatched area is subtracted twice from the total intensity I_{total} to obtain $I(\Delta x)$. $I(\Delta y)$ can be calculated analogously to $I(\Delta x)$ and is given by

$$
\frac{I_{U-L}}{I_{total}} = 1 - \mathrm{erfc}\left(\frac{\Delta y \sqrt{2}}{w_0}\right) = I(\Delta y), \tag{9.15}
$$

where U/L define the upper/lower halves, respectively. For small displacements Δx and Δy the Eq. (9.14) and Eq. (9.15) can be linearised via a Taylor expansion of the error function [118], which results in

$$
I(\Delta x)_{\text{linear}} = -\frac{2}{\sqrt{\pi}} \frac{\Delta x \sqrt{2}}{w_0}, \tag{9.16}
$$

$$
I(\Delta y)_{\text{linear}} = -\frac{2}{\sqrt{\pi}} \frac{\Delta y \sqrt{2}}{w_0}. \tag{9.17}
$$

This linearised form is essential for our investigations, since our systematic control approach considers LTI systems. After the derivation of the motion-dependent intensity values, we needed to determine the relation between the motion of the end mass to the laser beam position on the QPD. The relation was determined for the three DOFs of interest.

For a longitudinal motion ΔL of the lower test mass, see Fig. 9.12, we obtained the following relations regarding an incident laser beam, which is reflected under an angle θ

$$
\sin(2\theta_i) = \frac{\Delta x_{\text{long},i}}{h_i}, \tag{9.18}
$$

$$
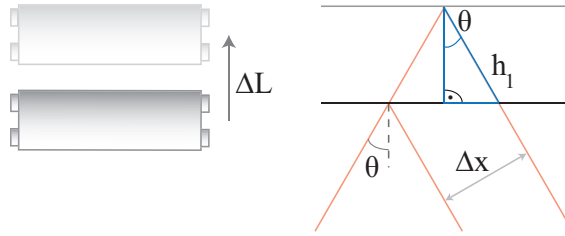\cos(\theta_i) = \frac{\Delta x_{\text{long},i}}{h_i}. \tag{9.19}
$$

Figure 9.12: Longitudinal motion ΔL of the end mass with the resultant displacement Δx of the laser beam reflected under an angle θ.
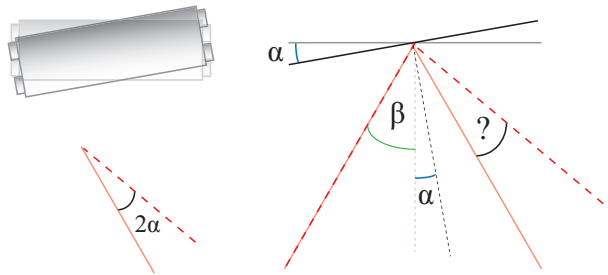

Figure 9.13: An end mass displaced by an angle α results in a displacement Δx on the QPD. To obtain the resulting displacement the arc of the sought angle is projected onto the surface of the QPD at a distance l. β denotes the angle of incidence for the undisplaced case.

$2h_i$ is the additional path length of the light, whereas $i = 1, 2$ denotes the associated optical lever. Solving one of the equations for h_i and inserting the result into the other leads to the longitudinal displacement $\Delta x_{\text{long},i}$

$$\Delta x_{\text{long},i} = 2\sin(\theta_i)\Delta L. \tag{9.20}$$

A lower test mass displaced by the angle α results in a displacement $\Delta x_{\text{yaw},i}$ on the QPD. To obtain the resulting displacement the arc of the sought angle is projected onto the surface of the QPD_i at a distance l_i and $\Delta x_{\text{yaw},i}$ becomes

$$\Delta x_{\text{yaw},i} = 2l_i\alpha. \tag{9.21}$$

It is evident from Eq. (9.20) and Eq. (9.21) that both motions yaw/longitudinal result in a Δx. Hence, the total displacement for the x-axis is given by the

combination

$$\Delta x_i = \Delta x_{\text{long},i} + \Delta x_{\text{yaw},i} = 2\sin(\theta_i)\Delta L + 2l_i\alpha. \qquad (9.22)$$

We set up two optical levers under different angles (see Table 9.2), to be able
to decompose Δx_i into its individual components. Considering two QPDs and
Eq. (9.22) leads to an equation system

$$\Delta x_1 = 2\sin(\theta_1)\Delta L + 2l_1\alpha,$$
$$\Delta x_2 = 2\sin(\theta_2)\Delta L + 2l_2\alpha. \qquad (9.23)$$

Solving one equation for ΔL or α and substituting the result into the other leads
to

$$\Delta L = \frac{l_2\Delta x_1 - l_1\Delta x_2}{2\left(l_2\sin(\theta_1) - l_1\sin(\theta_2)\right)}, \qquad (9.24)$$

$$\alpha = \frac{x_2\sin(\theta_1) - x_1\sin(\theta_2)}{2\left(l_2\sin(\theta_1) - l_1\sin(\theta_2)\right)}. \qquad (9.25)$$

With the known parameters l_i and θ_i it is possible to compute ΔL and α from
the measured data of the QPD_i.

An angular pitch displacement ρ of the end mass results in a Δy_i displaced laser
beam on the QPD_i and is determined analogously to a yaw displacement

$$\Delta y_i = 2l_i\rho. \qquad (9.26)$$

9.5.2 Characterisation of the Optical Levers

We set up two optical levers, see Fig. 9.9, to measure the transfer functions re-
quired for a systematic control approach, whereby the measured lower test mass
motion defines the output and an excitation injected via the BOSEMs the input
of our system. The laser beam of the inner optical lever impinged onto the end
mass mirror under an angle of $\theta_1 = 8°$ and was detected by QPD_1 at a distance
$l_1 = 42\,\text{cm}$, with respect to the lower mass. The parameters of the outer opti-
cal lever were $\theta_2 = 38°$ and $l_2 = 27\,\text{cm}$. Both QPDs were placed in the waist
$w_0 = 700\,\mu\text{m}$ of their nearly collimated beams. The mode matching was needed
to ensure that a displaced laser beam was not changing its diameter and therefore
spoiling the outcome of the measurement. For example a displacement, which
would also reduce the beam size, with respect to the plane of the QPD, would

Table 9.2: Parameters of the optical levers.

Parameter	Value
Length l_1 of the inner optical lever	42.0 cm
Length l_2 of the outer optical lever	27.0 cm
Angle θ_1 of the inner optical lever	8°
Angle θ_2 of the outer optical lever	38°
Waist w_0 of the laser beams	700 μm

result in an erroneously large displacement value. The parameters of the optical levers are presented in Table 9.2.

To verify the functionality of our setup we needed to calibrate the optical levers [119]. Firstly we replaced the lower test mass by a mirror, which was mounted onto a multi-axis micrometer table capable of simulating a pure yaw/pitch displacement of the end mass. Secondly the mirror was mounted onto another micrometer table, which simulated a longitudinal displacement. Intensity curves measured by the QPD_i were compared to theoretically expected intensity curves given by Eq. (9.14-9.17). We used the above derived relations

$$\Delta x_i = \Delta x_{long,i} = 2\sin(\theta_i)\Delta L$$
$$\Delta x_i = \Delta x_{yaw,i} = 2l_i\alpha$$
$$\Delta y_i = 2l_i\rho \tag{9.27}$$

for the calculation of $I(\Delta x_i)/I(\Delta y_i)$. The results for a yaw, pitch and longitudinal motion are shown in Figs. 9.14-9.16, whereas the black curves correspond to the measured Δy, the red curves to the measured Δx, the blue curves to simulated displacements and the green curves to linear fits of the displacement. The results for an angular yaw displacement, see Fig. 9.14, demonstrated that the optical levers worked as required. The simulated Δx displacements (in blue) are in very good agreement with the obtained data (in red). The inner optical lever (QPD_1) was more sensitive to angular displacements, which was expected, since $l_1 > l_2$. The linear fits (in green) match the linear region of the measured data and set an upper limit for the excitation used to generate the system transfer functions. A matched excitation ensures that the system response stays in the linear regime. This is required, since we consider LTI systems. The Δy

Figure 9.14: The upper graph shows the measured results for a yaw displace-
ment $\Delta x_1 / y_1$ and compares them with the theoretically expected
displacement and a linear fit. The linear fit determines the linear
region of system, which is essential for the implementation of lin-
ear control techniques. The lower graph presents the results for the
second optical lever. It can be seen that the first optical lever is
more sensitive to a yaw displacement than the second one, since
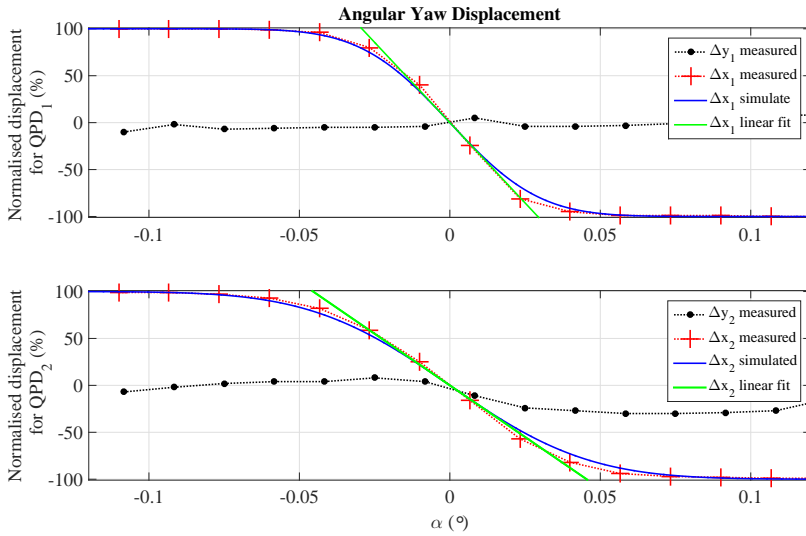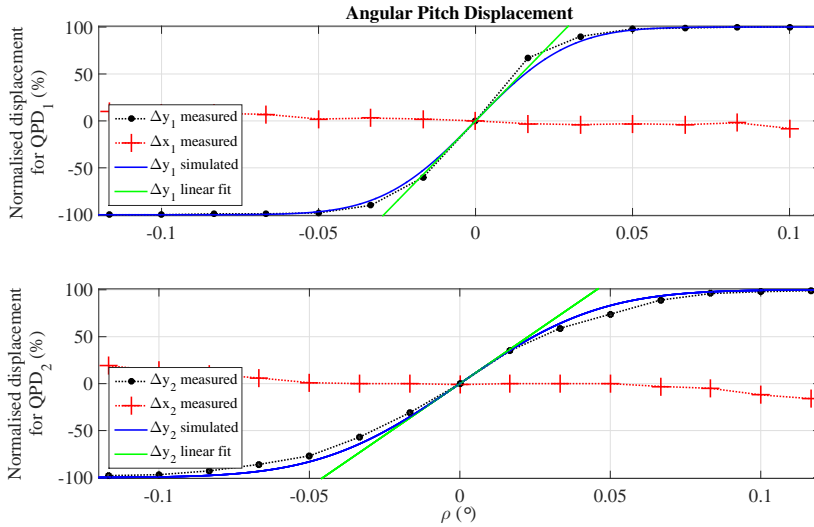$l_1 > l_2$.[119]

Figure 9.15: The upper graph shows the measured results for a pitch displacement $\Delta x_1/y_1$ and compares them with the theoretically expected displacement and a linear fit. The linear fit determines the linear region of system, which is essential for the implementation of linear control techniques. The lower graph presents the results for the second optical lever. It can be seen that the first optical lever is more sensitive to a pitch displacement than the second optical lever, since $l_1 > l_2$.[119]

displacement should ideally be zero for a yaw motion. Δy of the inner optical lever is in very good agreement with this assumption, but the outer optical lever showed a non-zero response. The behaviour of the outer optical lever was also observed for $\Delta x/y$ of the pitch/longitudinal calibrations, respectively. This lead to the conclusion that the orientation of QPD_2 is slightly rotated relative to the optical axis. We circumvented this problem by choosing appropriately small excitations, which allow us to neglect the effect of the rotation. Another possibility would have been the application of a rotation matrix in the post-processing of the measured data. The results for pitch are comparable with the yaw results. The simulated displacements are again in very good agreement with the measured data (in black) and the linear fit defines the upper limit for the excitation.
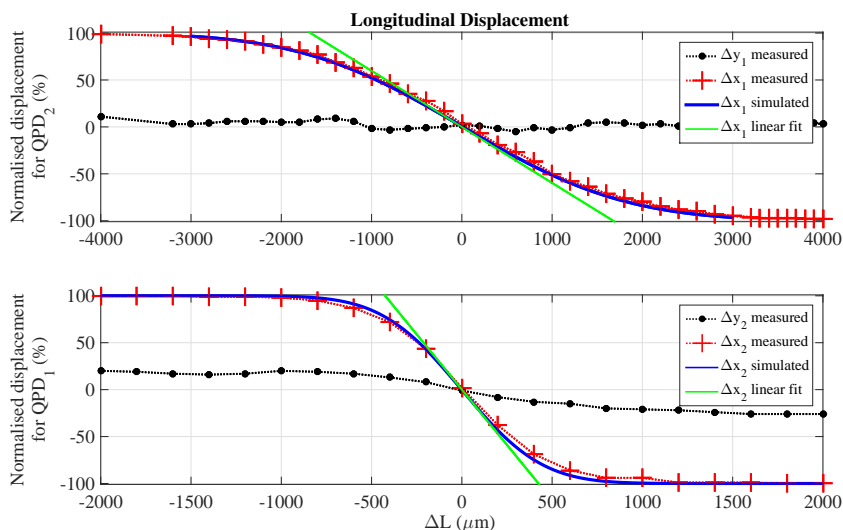
Figure 9.16: The upper graph shows the measured results for a longitudinal displacement $\Delta x_1/y_1$ and compares them with the theoretically expected displacement and a linear fit. The linear fit determines the linear region of system, which is essential for the implementation of linear control techniques. The lower graph presents the results for the second optical lever. It can be seen that the second optical lever is more sensitive to a longitudinal displacement than the first optical lever, since $\theta_1 < \theta_2$.[119]

As mentioned above, QPD_2 showed a non-vanishing Δx response, which is due to its rotated mounting. The longitudinal results show an excellent agreement between the simulated and measured data, with the outer optical lever more sensitive to a longitudinal motion. This was expected, since $\theta_1 < \theta_2$. The upper excitation limit was again obtained from the linear fit and the outer optical lever showed again the characteristic behaviour of a rotated QPD_2. We demonstrated with this calibration that the two optical levers performed as required.

9.6 Characterisation of the Suspension Dynamics

For the implementation of a modern controller, which actively damps the eigenfrequencies of the triple pendulum suspension, we needed to determine the system dynamics corresponding to the three DOFs of interest. For a complete system description a transfer function matrix determining every possible input/output relation was required. How the outputs of the optical levers are related to the DOFs is derived in Eqs. (9.24)-(9.26). We considered the control inputs to be virtual actuators, which directly excite one mode of the three DOFs. The virtual actuators u_l, u_y and u_p refer to specific BOSEM combinations. The BOSEMS attached to the upper mass named with Latin letters are shown in Fig. 9.17 [112] and the derived combinations are given by the utilised BOSEMs (D,E,B and C), where the index out denotes the force of a BOSEM acting on the upper mass

$$u_l = \frac{1}{2}(D_{out} + E_{out}), \tag{9.28}$$

$$u_y = \frac{1}{2}(D_{out} - E_{out}), \tag{9.29}$$

$$u_p = \frac{1}{2}(B_{out} - C_{out}). \tag{9.30}$$

To address the correct mode the relations $D_{out} = E_{out}$ and $B_{out} = C_{out}$ needed to be satisfied, where the force acting on the upper mass depends on the inputs of the coil actuators $D_{coil}, E_{coil}, B_{coil}$ and C_{coil}. Ideally $D_{coil} = E_{coil}$ and $B_{coil} = C_{coil}$ due to the identical BOSEM design. We checked these relations for each DOF by applying constant voltages to the coil inputs and comparing the responses of the system with the calibration curves of the optical levers. The results $B_{coil} = C_{coil}$ satisfied the relation $B_{out} = C_{out}$. However $D_{coil} = E_{coil}$ did not satisfy the relation $D_{out} = E_{out}$. We needed to apply an additional scaling factor $D_{coil} = 0.8725 \cdot E_{coil}$ to fulfil the requirement $D_{out} = E_{out}$. The reason for this factor was a missing magnetic flag holder of BOSEM D, which decreased the magnetic force.

9.7 Control and Data Acquisition System

We used the digital control and data acquisition system (CDS) [120] to actuate the triple pendulum suspension and read out its response. CDS was designed
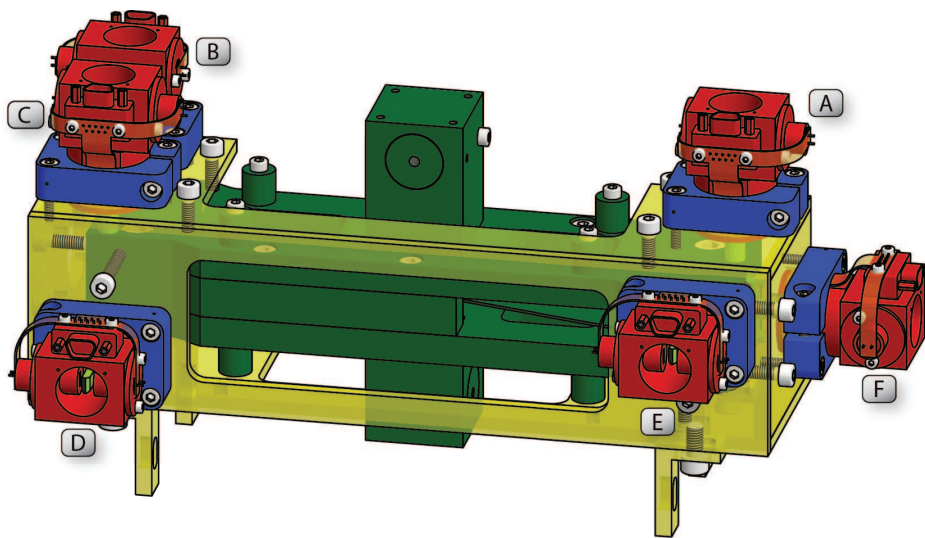
Figure 9.17: The schematic (taken from [112]) shows the upper mass (green)
with attached co-located sensor/actuator pairs. A frame (yellow)
connected with the cage of the suspension clamps the actuator and
readout units (red) of the BOSEMs, whereas the magnetic flag (light
green) is attached to the freely movable upper mass.

at Caltech to facilitate the operation of GWDs. The CDS front-end runs under a real-time Linux system providing 32 ADC-channels and 16 DAC-channels with a 16 bit resolution. The ADC/DAC-channels incorporate matched anti-aliasing/anti-imaging filters, respectively. The sampling rate of the system is 65.536 kHz. Real-time signal processing is achieved by the implementation of Simulink models. These models run on the core of a selected central processing unit of the front-end. The real-time data is displayed via a graphical user interface, called MEDM. We used built-in software called Digital Test Tools (DTT) to obtain the frequency response data of the triple pendulum suspension. DTT computes the desired transfer function via assigned measurements of the inputs/outputs. An interface between DTT and another program called Foton allows for shaping of the excitation signals with the help of digital filters.

9.8 System Identification

Obtaining good quality transfer functions was not easy, due to the dynamic range of 150 dB between signals. The white noise excitation signals required frequency-dependent shaping. We accomplished this via digital filters, which had the shape of the inverted suspension transfer function regarding the excited DOF. This shaping and an appropriate amplitude of the white noise ensured that no sensor saturation effects occurred and that the input was strong enough to distinguish test mass motion from the existent noise floor. Furthermore the digital filter had to account for the transfer function of the coil driver electronics given by

$$G_{driver}(s) = \frac{(s+50)^2}{(s+1)^2}. \tag{9.31}$$

We operated the system in the small displacement regime, assuming that linearised models are able to exactly describe the system. This assumption allows for the usage of linear control techniques, although the overall system is non-linear.

For our input-output model we considered three inputs and six outputs. Because of this highly coupled and resonant system, automated system identification tools performed poorly. The Matlab subspace routine (n4sid) and the prediction error algorithm (PEM) were unable to properly fit models to the frequency response data. Commonly the zeros, affecting the transient response, could not be modelled. As an outcome of this we manually fitted individual transfer functions,

where we needed to place the poles and zeros of the system. We also had to
address the Q-factor of the poles and zeros and the system gain k. A transfer
function containing only resonant poles and zeros can be formulated as

$$H(s) = k \frac{\prod_{i=1}^{m} \left(s^2 + 2\zeta_{z_i}\omega_{z_i}s + \omega_{z_i}^2\right)}{\prod_{j=1}^{n} \left(s^2 + 2\zeta_{p_j}\omega_{p_j}s + \omega_{p_j}^2\right)}, \tag{9.32}$$

where ω_{z_i} and ω_{p_j} are the frequencies of the system zeros/poles and ζ_{z_i} and ζ_{p_j}
are the corresponding damping factors. The Q-factor is $Q = 1/2\zeta$ and $m < n$.
An advantage of our approach was the fact that we could choose our poles/zeros
manually, since the resonance frequencies of the system shifted by very small
amounts over time. Concerning an automated system identification method a
frequency shift could raise a problem, since one mode could be addressed by
two or more frequencies. We characterised the system by determining two trans-
fer function matrices. The first was given by top-top transfer functions, where
the co-located sensors/actuators were used as outputs/inputs. The second matrix
was given by top-bottom transfer functions, where the system was excited via
the coil actuator and the output was given by the readout of the optical levers. As
presented in Fig. 9.18 and Fig. 9.19 the fitted models were in very good agree-
ment with the measured frequency response data. Only the transfer function
corresponding to a longitudinal excitation and the pitch output showed character-
istics we were not able to adequately model or interpret. A further sophisticated
investigation of the closed-loop performance regarding this transfer function is
required to describe the present dynamics. Not only the resonance frequencies
for longitudinal, yaw and pitch, shown in Table 9.3, contributed to the overall
system dynamics, since resonance frequencies (not explicitly measured) of other
DOFs (roll/vertical) could also be observed. It is also worth mentioning that the
determination of the Q-factors was challenging for a variety of modes, which
could affect the performance of the control design. A solution for this problem is
given by measuring the transient response of a selectively excited mode, which
would yield a more exact Q-factor.

An important requirement was that the system is described by one state equa-
tion describing the system evolution, although we used top-top and top-bottom
frequency data. The reason for this is that the system states evolve uniquely,
where the measured differences were caused by the C matrix, which weights the
states to the outputs. We compiled the fitted transfer functions into a 6x3 transfer
function matrix and used the Matlab functions *balreal* and *modred* yielding an

Figure 9.18: Comparison of the fitted models (in red) and the measured frequency response data (in black) for the top-top transfer functions. The fitted models are in good agreement with the measured data.

Table 9.3: Resonance frequencies of the three DOFs of interest.

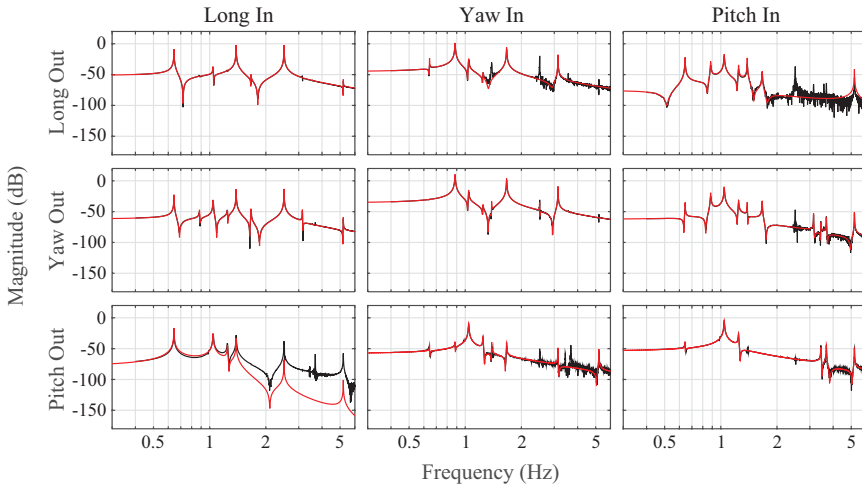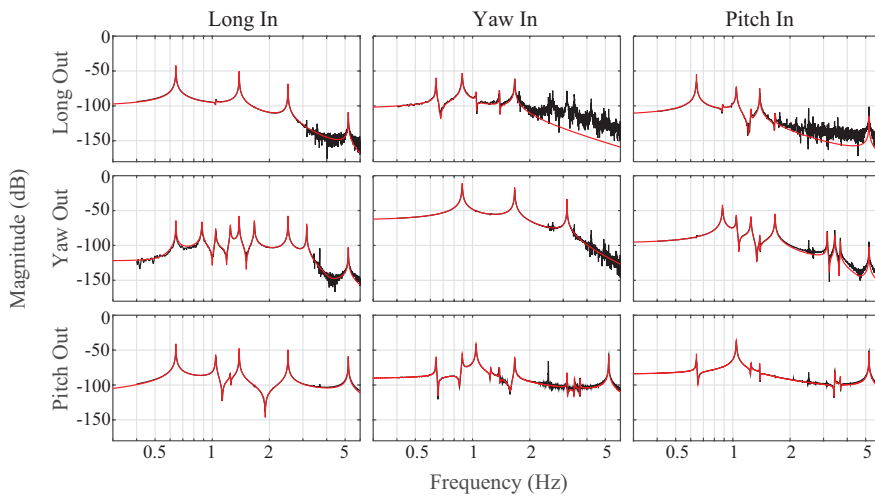| Parameter	Value
Longitudinal	0.64 Hz
	1.38 Hz
	2.51 Hz
Yaw	0.88 Hz
	1.66 Hz
	3.14 Hz
Pitch	1.03 Hz
	5.20 Hz
	10.51 Hz

Figure 9.19: Comparison of the fitted models (in red) and the measured frequency response data (in black) for the top-bottom transfer functions. The fitted models are in good agreement with the measured data.

accurate model containing ≈ 60 states. A state-space model was formulated

$$\dot{x} = Ax + Bu \tag{9.33}$$

$$y = Cx + Du \tag{9.34}$$

$$= \begin{bmatrix} C_{tb} \\ C_{bs} \end{bmatrix} x + \begin{bmatrix} D_{tb} \\ D_{bs} \end{bmatrix} u, \tag{9.35}$$

where $A \in \mathbb{R}^{n \times n}$, $B \in \mathbb{R}^{n \times 3}$, $C \in \mathbb{R}^{6 \times n}$ and $D \in \mathbb{R}^{6 \times 3}$. We defined $C_{tb}, C_{bs} \in \mathbb{R}^{3 \times n}$ and $D_{tb}, D_{bs} \in \mathbb{R}^{3 \times 3}$ to distinguish between the subsystems. The state-space model can be converted into a transfer function, see Chap. 5, via

$$G(s) = C(sI - A)^{-1}B + D. \tag{9.36}$$

A common notation is

$$G(s) = \left[\begin{array}{c|c} A & B \\ \hline C & D \end{array} \right]. \tag{9.37}$$

We defined the subsystems G_{tb} and G_{bs}, describing the transfer functions for top-bottom and top-top, respectively by

$$G_{tb}(s) = \left[\begin{array}{c|c} A & B \\ \hline C_{tb} & D_{tb} \end{array} \right], \quad G_{bs}(s) = \left[\begin{array}{c|c} A & B \\ \hline C_{bs} & D_{bs} \end{array} \right], \tag{9.38}$$

which when combined yield

$$G(s) = \left[\begin{array}{c|c} A & B \\ \hline C_{tb} & D_{tb} \\ C_{bs} & D_{bs} \end{array} \right]. \tag{9.39}$$

9.9 Modern Controller Synthesis

Commonly utilised controllers, which actively damp the eigenmodes of the system, use for example *velocity feedback*. Hereby $Bu = -G\dot{x}$, directly affecting the damping term, such that $\tilde{C} = C + G$. A limitation of velocity feedback is spillover, where unmodelled high-frequency dynamics can cause instabilities [121]. Another disadvantage is the increasing control effort towards high frequencies, injecting noise into the system [122]. Another example is the *modal control approach*, implemented for LIGO's quadruple mirror suspensions

[122, 123], modelling the system as a second-order matrix differential equation. While this approach is promising, it must be noted that an estimator was needed to determine all system states [122, 124] and hence the performance of this approach depends on the accuracy of the system model.

Our control design incorporated the motion of the lower test mass, which is usually not assessed for control approaches, although the RMS motion of the end mass defines the performance of the suspension system. There are no previous studies examining the effect of controllers on the end mass motion. We examined the implementation of nominal $\mathcal{H}_2$ controller synthesis techniques, which were developed for highly complex MIMO systems. With a general control formulation it is also straightforward to examine $\mathcal{H}_\infty$ synthesis techniques.

9.9.1 Generalised Control Formulation

We introduce the generalised feedback configuration to convert a control problem into a $\mathcal{H}_2/\mathcal{H}_\infty$ optimisation problem [125]. For this approach these signals need to be modelled:

- u, control input/s,

- w, disturbance input/s - the impact of the disturbance on the system must be minimised,

- y, the measured output/s and

- z, the performance objective to be minimised.

Fig. 9.20 presents the standardised framework which can be written as

$$\begin{bmatrix} z \\ y \end{bmatrix} = P(s) \begin{bmatrix} w \\ u \end{bmatrix} = \begin{bmatrix} P_{11}(s) & P_{12}(s) \\ P_{21}(s) & P_{22}(s) \end{bmatrix} \begin{bmatrix} w \\ u \end{bmatrix}, \qquad (9.40)$$

with vectors u, w, y and z and the transfer function matrix P. Eq. (9.40) shows, how the controlled input u and the input disturbance w are related to the outputs of a closed-loop system. Here y is the measured output and z defines a performance objective, which shall be minimised. In general z is a virtual output, whereas in our case z can be measured, since our performance criterion is the minimisation of the lower mass motion. We can relate w to z by the linear fractional transform $\mathcal{F}_l(P, K)$ describing the closed-loop system dynamics
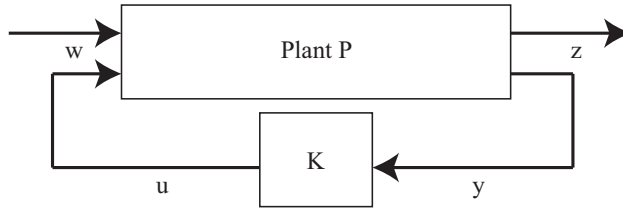
Figure 9.20: A generalised feedback interconnection is shown in this block diagram. The input/output relation of w/z is given by the linear fractional transform $\mathcal{F}_l(P, K)$. The control objective is to compute a controller K that minimises the impact of a disturbance w on the performance criterion z.

including the controller equation $u = Ky$

$$z = \mathcal{F}_l(P, K)w, \tag{9.41}$$

where

$$\mathcal{F}_l(P, K) = P_{11} + P_{12}(I - KP_{22})^{-1}P_{21} \tag{9.42}$$

and K is the controller. $\mathcal{H}_2/\mathcal{H}_\infty$ control designs provoke the minimisation of the $\mathcal{H}_2/\mathcal{H}_\infty$ norms of $\mathcal{F}_l(P, K)$, respectively.

9.9.2 $\mathcal{H}_2$ Optimal Control

The solution to the $\mathcal{H}_2$ optimal control problem is the controller K, which minimises the $\mathcal{H}_2$ norm [125]

$$\|F(s)\|_2 = \sqrt{\frac{1}{2\pi} \int_{-\infty}^{\infty} \operatorname{tr}\left[F^H(j\omega)F(j\omega)\right] d\omega}, \tag{9.43}$$

where $F(s) := \mathcal{F}_l(P, K)$. Minimising this norm minimises the RMS output power z of the generalised system in the presence of a unit-intensity white noise disturbance input [125].

In our case the unknown disturbance is seismic noise. Fig. 9.21 shows the seismic noise spectrum (black)in the x-direction, obtained via geophones located in our laboratory, and an associated 15th-order model (red). The shorthand notation
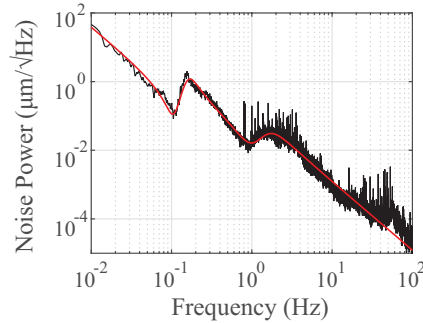
Figure 9.21: Seismic noise spectrum in the x-direction in the laboratory and its
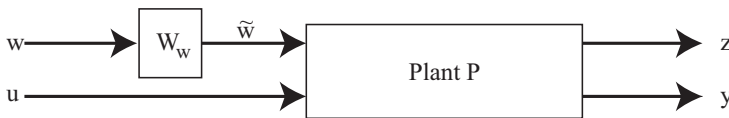associated fit.

Figure 9.22: Coloured noise disturbances can be modelled with additional dy-
namics W_w. In our case W_w was chosen such that the noise spec-
trum $\tilde{w}$ matched the seismic noise spectrum. We reformulated the
plant dynamics to include the augmented noise.

of the seismic noise model is given by

$$W_w(s) = \left[\begin{array}{c|c} A_w & B_w \\ \hline C_w & D_w \end{array} \right]. \tag{9.44}$$

The seismic noise spectrum shows an overall $1/f$ characteristic and is therefore
a non-white noise. To adequately include the effect of the disturbance, we had
to augment the plant with additional dynamics, which coloured the noise. The
plant and noise dynamics are given by Eqs. (9.37), (9.44), respectively. We take
an additional step to point out the series connection of two state-space models
presented in Fig. 9.22. The state space equations are expressed as

$$\dot{x}_w = A_w x_w + B_w u_w \tag{9.45}$$

$$\tilde{w} = C_w x_w + D_w u_w \tag{9.46}$$

$$\dot{x} = Ax + B\tilde{w} + Bu \tag{9.47}$$

$$y = Cx + D\tilde{w} + Du, \tag{9.48}$$

with C and D defined in Eq. (9.35). The series connection of the two systems was calculated by substituting Eq. (9.46) into Eqs. (9.47),(9.48)

$$\dot{x} = Ax + B(C_w x_w + D_w w) + Bu \tag{9.49}$$

$$y = Cx + D(C_w x_w + D_w w) + Du \tag{9.50}$$

and the dynamics of the augmented system were

$$\begin{bmatrix} \dot{x} \\ \dot{x}_w \end{bmatrix} = \begin{bmatrix} A & BC_w \\ 0 & A_w \end{bmatrix} \begin{bmatrix} x \\ x_w \end{bmatrix} + \begin{bmatrix} BD_w \\ B_w \end{bmatrix} w + \begin{bmatrix} B \\ 0 \end{bmatrix} u \tag{9.51}$$

$$y = \begin{bmatrix} C & DC_w \end{bmatrix} \begin{bmatrix} x \\ x_w \end{bmatrix} + DD_w w + Du. \tag{9.52}$$

This was transformed into a generalised plant P

$$P = \left[\begin{array}{cc|cc} A & BC_w & BD_w & B \\ 0 & A_w & B_w & 0 \\ \hline C_{tb} & D_{tb}C_w & D_{tb}D_w & D_{tb} \\ C_{bs} & D_{bs}C_w & D_{bs}D_w & D_{bs} \end{array} \right], \tag{9.53}$$

where $z = G_{tb}(u + \tilde{w})$ describes how the controlled input u and the disturbance w couple from the upper mass to lower mass motion. Thus, z defines the performance criterion we wanted to minimise, which is the RMS motion of the end mass. y is the measured output, which is utilised for feedback control. In our case y is given by the output of the BOSEMs. It is also possible to define additional performance criteria.

9.9.3 $\mathcal{H}_2$ Mixed-Sensitivity Control

Up to now we only considered to minimise z. We enforced no constraints on the characteristic behaviour of the controller or the applied control energy yet. A well-known $\mathcal{H}_2$ mixed-sensitivity technique is the LQG problem, see Chap. 5
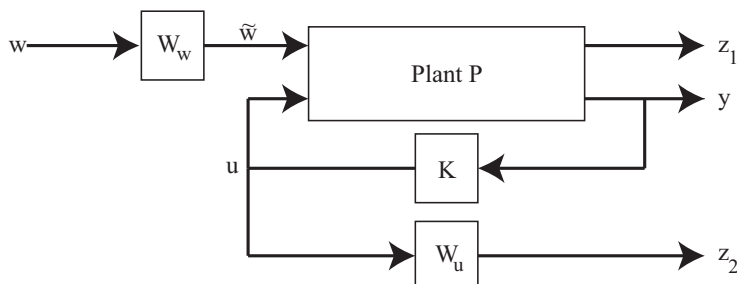
Figure 9.23: The generalised $\mathcal{H}_2$ mixed-sensitivity design enables the frequency
weighting to optimise the control performance. In our case we want
to minimise the RMS motion of the lower mass of the triple pendu-
lum $z_1 = G_{tb}(u + \tilde{w})$ and weight the control input $z_2 = W_u u$. The
weighting function W_u affects the controller bandwidth.

or [125]. Mixed-sensitivity techniques were first introduced in $\mathcal{H}_\infty$ optimisa-
tion problems [126, 127], but can be transferred to $\mathcal{H}_2$ problems with the help
of the generalised framework. To achieve suitable feedback loops, the mixed-
sensitivity techniques allows for frequency-dependent shaping of your controller
[125]. We now show how such constraints and weights can be incorporated into
the generalised plant regarding our system. Let us consider the performance
variables z_1 and z_2

$$z_1 = G_{tb}(u + \tilde{w}) \quad \text{and} \quad z_2 = W_u u. \tag{9.54}$$

z_1 corresponds to the earlier introduced performance criterion, which copes with
the minimisation of the lower mass motion. In addition to z_1 we introduce z_2,
a weighted version of the controlled input u, setting constraints on the applied
control energy. The weight W_u can be expressed as

$$W_u = \left[\begin{array}{c|c} A_u & B_u \\ \hline C_u & D_u \end{array} \right]. \tag{9.55}$$

Such a weighting is desirable as it enables us to define the bandwidth of the
designed controller. Furthermore such a weighting is a more intuitive way to
define the bandwidth in comparison to the LQG approach. A block diagram
of the optimisation problem is presented in Fig. 9.23, and the generalised plant

becomes

$$P = \left[\begin{array}{ccc|cc} A & BC_w & 0 & BD_w & B \\ 0 & A_w & 0 & B_w & 0 \\ 0 & 0 & A_u & 0 & B_u \\ \hline C_{tb} & D_{tb}C_w & 0 & D_{tb}D_w & D_{tb} \\ C_{bs} & D_{bs}C_w & 0 & D_{bs}D_w & D_{bs} \end{array}\right]. \tag{9.56}$$

The Matlab function *h2syn* was used for the controller synthesis. The result was a complex controller consisting of 75 states whose output u got weighted by a transfer function

$$G(s) = \frac{0.003s^2 + 0.006s + 0.003}{s^2 + 100s + 2500}. \tag{9.57}$$

The weighting of the controlled input u ensured that the computed controller did not have a differentiator characteristic. The Bode diagram of the $\mathcal{H}_2$ controller, which should actively damp the suspension resonances, is illustrated in Fig. 9.24. Hereby y_l, y_y, y_p and u_l, u_y, u_p are the outputs of the plant and the controlled inputs to the plant corresponding to the three DOFs of interest, respectively. Furthermore we simulated the closed-loop response of the system, highlighting the performance of this control approach (in orange) in comparison to the undamped case (in blue), see Fig 9.25. The simulation points out that some of the modes are suppressed by $\approx 50\,\text{dB}$ without exciting other modes significantly (or at all). It is worth mentioning that $\mathcal{H}_2$ synthesis techniques are extremely useful with very accurate knowledge of the plant. However there are no stability guarantees for model mismatches [89]. This point is essential for resonant systems, where a small shift in the resonance frequency may have disastrous consequences. Robust control techniques could handle small variations, but require modelling/estimation of uncertainties. These uncertainties limit the performance of robust controllers. For a triple pendulum suspension the modelling of uncertainties is phenomenally complex.

9.9.4 $\mathcal{H}_\infty$ Optimal Control

The procedure for $\mathcal{H}_\infty$ control can be described in analogy to the $\mathcal{H}_2$ scenario. This time the $\mathcal{H}_\infty$ norm is minimised

$$J(K) = \|\mathcal{F}_l(P, K)\|_\infty = \max_\omega \bar{\sigma}\left(\mathcal{F}_l(P, K)(j\omega)\right), \tag{9.58}$$

where $\bar{\sigma}$ is the largest single value. $\mathcal{H}_\infty$ control techniques try to minimise the maximum gain value of the plant. In practise it is more convenient to design a
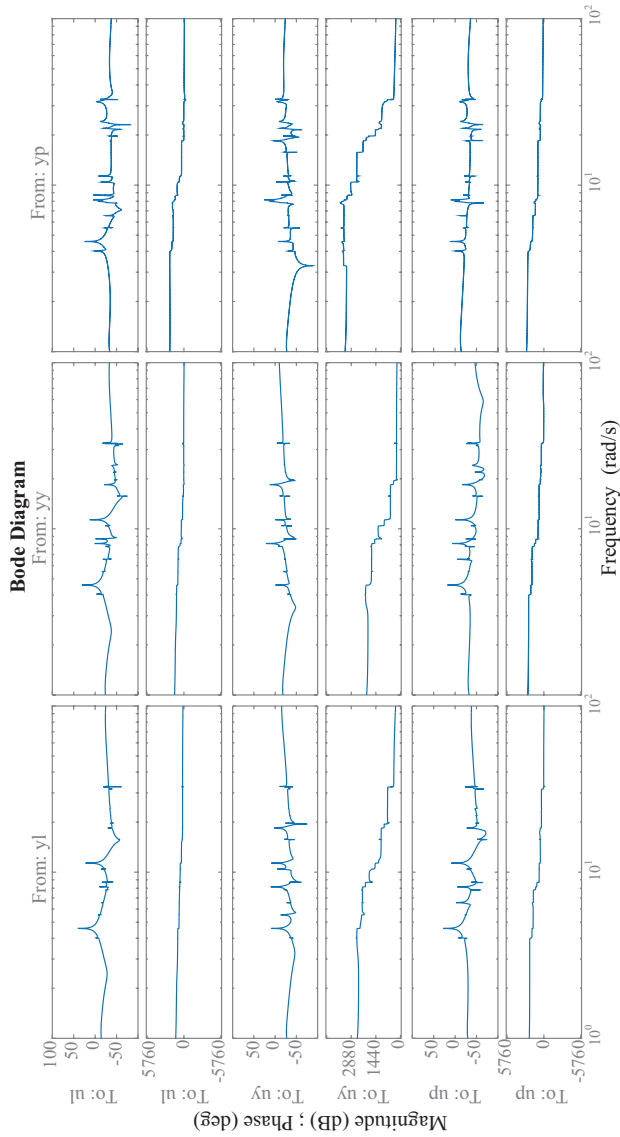
Figure 9.24: Bode plot of the computed $\mathcal{H}_2$ controller. The input of the transfer function is the system output $y_{l,y,p}$ and the output is given by the controlled input $u_{l,y,p}$ associated with the considered DOFs.

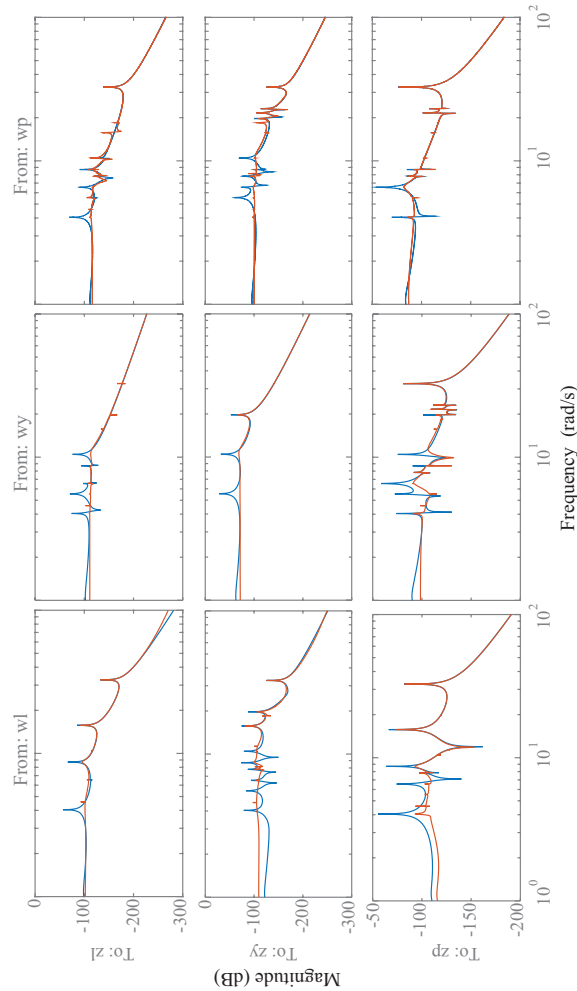Figure 9.25: Simulated closed-loop performance of the $\mathcal{H}_2$ control approach (in orange) in comparison to the undamped case (in blue), highlighting the capability of damping modes by ≈ 50 dB without exciting other modes significantly. The disturbance inputs and the performance criteria with respect to the controlled DOFs are denoted as w_l, w_y, w_p and z_l, z_y, z_y, respectively.

137

suboptimal controller, which satisfies

$$\|\mathcal{F}_l(P,K)\|_\infty < \gamma. \tag{9.59}$$

This control challenge can be solved by decreasing γ iteratively until an optimal
solution is reached [125]. It is also possible to incorporate elements from both
techniques $\mathcal{H}_2/\mathcal{H}_\infty$ for sophisticated multi-objective optimisation schemes.

9.10 Conclusions

We set up a triple pendulum suspension with the help of the 10 m prototype
group for a systematic controller design, which should actively damp the reso-
nant system. Our control design incorporated the RMS motion of the lower mass,
which has never been directly addressed before, although the desired control ob-
jective for suspension control is to minimise the lower mass motion. Detailed
information of this motion was obtained via two fully calibrated optical levers,
which were able to detect the motion corresponding to a longitudinal, yaw and
pitch displacement. These DOFs have the strongest impact on the output of a
Michelson interferometer. We measured the system dynamics by exciting a sys-
tem mode at the top stage and detecting the top/bottom system response for all
three DOFs. The result was a 6x3 transfer function matrix, which was used for
system identification. The manually fitted system model was put into the context
of a generalised control formulation, which was used to examine the applica-
tion of $\mathcal{H}_2/\mathcal{H}_\infty$ controller synthesis techniques. The generalised control formu-
lation allowed for a $\mathcal{H}_2$ mixed-sensitivity control approach incorporating con-
troller weighting functions. We computed a powerful $\mathcal{H}_2$ controller, suitable to
control this highly complex MIMO system including inherent cross-correlations.
The simulated closed-loop performance of the system highlighted the ability of
achieving damping factors of ≈ 50 dB without exciting other modes significantly.
The current task is the experimental implementation of our control scheme. This
task also includes the derivation of a simpler controller, which can be obtained
by applying *model order reduction* techniques, to lower the computational com-
plexity.

It is difficult to intuitively design controllers for MIMO systems. Therefore math-
ematical techniques become advantageous, although the generated controllers
have the same number of states as the plant, which can be impractical due to the
computational complexity. For this reason model order reduction is in general an

area of active research. $\mathcal{H}_2/\mathcal{H}_\infty$ techniques require more complex problem formulations, but offer sophisticated and unique control design possibilities, which could increase the performance of suspension systems.

10

Summary and Outlook

The goal of this thesis was to pave the way for the implementation of modern control techniques in our research field. Mathematical control techniques, inherently capable of coping with undesired coupling terms, become advantageous for complex MIMO systems for which an intuitive controller design approach is not feasible. An example of such a complex MIMO system is a laser interferometric GWD consisting of numerous nested loops; the complexity of GWDs will be further increased by the implementation of some of the advanced techniques considered for next generation gravitational wave detectors [128, 129]. Thus, the application of modern control techniques can be beneficial for a systematic treatment of control challenges and potentially improve the performance of a GWD. The first step towards the defined goal was the construction of a suitable quantum optical test bed for the implementation of modern control approaches. The test bed was a three-mirror ring cavity, whose length needed to be locked to the frequency of a laser. We measured transfer functions to characterise the system. The frequency response data was used to derive a third-order state-space model describing the plant required for the computation of a LQG controller. We augmented the LQG controller by integral action, as with static state feedback control the states of the system cannot converge in the presence of constant input/output disturbances. Our LQG controller with additional integral action was able to lock the cavity, and the closed-loop stability and performance were verified via step response data. We published the results in [31], and the quantum optical test bed was already further utilised for a negative imaginary control ap-

proach [130].

We extended the previous locking scheme by substituting the time-invariant with a time-varying Kalman filter. This substitution allowed for the implementation of an optimal controller, which was capable of coping with large detunings Δ between laser and optical resonator, exceeding the linear region of the error signal. Thus, this approach was suitable as an autolocking scheme. We realised this control approach by utilising the singular perturbation method to simplify our system dynamics and to permit the application of linear control techniques. The combination of error signal and detected transmitted power was used to estimate the detuning of the cavity. We made use of this estimate to compute and implement an optimal controller, which is able to lock the cavity from any given operating point. The results demonstrated improved robustness to disturbances and faster locking times in comparison to a traditional PI controller. More importantly, our controller, incorporating a time-varying Kalman filter, automatically acquired lock for large detunings, which correspond to the non-linear region of the error signal, a feat which cannot be achieved by linear time-invariant controllers. The results obtained show the superior performance of our control scheme and were published in [32]. It is noteworthy that such a control approach could ease the reacquisition of locks and therefore enhance the duty cycle of GWDs.

We further investigated the possibility of placing our squeezed light source in the context of MIMO control problems, for which a modern control approach is beneficial. After a detailed theoretical and experimental characterisation of our bow-tie OPO, we tried to identify possible couplings between the pump lock and the OPO cavity lock. The result was that the two feedback loops were completely decoupled, this is due to the applied modulation schemes; A PDH scheme for the OPO lock and a dither locking scheme for the stabilisation of the relative phase between the intracavity and pump field. We added the LO lock as a third parameter, which is sensible for experiments incorporating a homodyne detection scheme in order to amplify the detected signals. We found that the LO lock has no impact on the other feedback loops, whereas the control loops for the pump and OPO influence the LO loop. Due to these non-vanishing coupling terms, we can state that the control of our squeezed light source, including the LO lock, can be described as a MIMO control problem.

An example of a complex MIMO system is a triple pendulum suspension for optical components of GWDs or other high-precision measurements, which need to strongly isolate their components from seismic noise. Triple pendulum sus-

pensions make use of the characteristic behaviour of cascaded harmonic oscillators and reach a suppression of seismic noise of $1/f^6$ above their resonance frequencies. However, on resonance the RMS motion of the lower mass is excited and therefore suspended optics require active control to damp the eigenmodes of the system. This MIMO control problem is commonly addressed by traditional control approaches, where the system transfer functions have been obtained via co-located sensor/actuator pairs attached to the upper mass of the suspension. The limitation of this control approach is the lack of information concerning the lower mass motion, which needs to be minimised. We set up two optical levers capable of reading out the lower mass motion with respect to the yaw, pitch and longitudinal DOF, which are the DOFs with the strongest influence on the output of an interferometer. We injected a disturbance at the upper mass and measured the response of the lower mass with the help of the calibrated optical levers. We utilised this frequency data to augment the commonly used upper mass-upper mass measurements with upper mass-lower mass measurements to enable a host of systematic control approaches, thereby enhancing the system performance. The result of these measurements was a 60th-order state-space model, which was put into the context of a general control formulation and used to examine the implementation of $\mathcal{H}_2/\mathcal{H}_\infty$ controller synthesis techniques. This generalised formulation allowed for a $\mathcal{H}_2$ mixed-sensitivity control approach, including frequency-dependent controller weighting functions and the consideration of coloured noise. We calculated a powerful $\mathcal{H}_2$ 75th-order controller which achieved damping factors of $\approx 50\,\mathrm{dB}$, without significantly exciting other modes. The next step will be the implementation of our control scheme. One part of the implementation is the derivation of a simpler controller via model order reduction techniques in order to lower the computational complexity which could limit the control loop performance. Fortunately, model order reduction is an area of active research, as the mathematically complex $\mathcal{H}_2/\mathcal{H}_\infty$ control approaches offer sophisticated and unique control design possibilities for MIMO systems.

Bibliography

[1] B.P. Abbott, R. Abbott, T.D. Abbott, M.R. Abernathy, F. Acernese, K. Ackley, C. Adams, T. Adams, P. Addesso, R.X. Adhikari, et al. Observation of gravitational waves from a binary black hole merger. *Physical Review Letters*, 116(6):061102, 2016.

[2] W.H. Press and K.S. Thorne. Gravitational-Wave Astronomy. *Annual Review of Astronomy and Astrophysics*, 10:335, 1972.

[3] B.F. Schutz. Gravitational wave astronomy. *Classical and Quantum Gravity*, 1999.

[4] A. Einstein. Näherungsweise Integration der Feldgleichungen der Gravitation. *Sitzungsberichte der Königlich Preußischen Akademie der Wissenschaften (Berlin)*, pages 688–696, 1916.

[5] Albert Einstein. Über Gravitationswellen. *Sitzungsberichte der Königlich Preußischen Akademie der Wissenschaften (Berlin)*, 1918.

[6] R.A. Hulse and J.H. Taylor. Discovery of a pulsar in a binary system. *Neutron stars, black holes, and binary X-ray sources*, 48:433, 1975.

[7] J.H. Taylor and J.M. Weisberg. A new test of general relativity-Gravitational radiation and the binary pulsar PSR 1913+ 16. *The Astrophysical Journal*, 253:908–920, 1982.

[8] R.A. Hulse. The discovery of the binary pulsar. In *Bulletin of the American Astronomical Society*, volume 26, 1994.

[9] J.H. Taylor. Binary pulsars and relativistic gravity. *Reviews of Modern Physics*, (3):711–719, 1994.

[10] J. Weber. Detection and Generation of Gravitational Waves. *Physical Review*, (1), 1960.

[11] J. Weber. Evidence for Discovery of Gravitational Radiation. *Physical Review Letters*, (24), 1969.

[12] S.W. Hawking and W. Israel. *Three Hundred Years of Gravitation*. Cambridge University Press, 1989.

[13] M.E. Gertsenshtein and V.I. Pustovoit. On the detection of low-frequency gravitational waves. *Soviet Journal of Experimental and Theoretical Physics*, 16:433, 1963.

[14] R. Weiss, D.J. Muehlner, R.L. Benford, D.K. Owens, N.A. Pierre, and M. Rosenbluh. Gravitation Research. *NASA Technical Report*, 1972.

[15] F. Acernese, T. Adams, M. Agathos, K. Agatsuma, A. Allocca, P. Astone, G. Ballardin, F. Barone, M. Barsuglia, A. Basti, et al. The Advanced Virgo Detector. In *Journal of Physics: Conference Series*. IOP Publishing, 2015.

[16] S. Dwyer, LIGO Scientific Collaboration, et al. Advanced LIGO status. In *Journal of Physics: Conference Series*, 2015.

[17] C. Affeldt, K. Danzmann, K.L. Dooley, H. Grote, M. Hewitson, S. Hild, J. Hough, J. Leong, H. Lück, M. Prijatelj, et al. Advanced techniques in GEO600. *Classical and Quantum Gravity*, 31, 2014.

[18] T. Akutsu, KAGRA collaboration, et al. Large-scale cryogenic Gravitational-Wave Telescope in Japan: KAGRA. In *Journal of Physics: Conference Series*, 2015.

[19] C.S. Unnikrishnan. IndIGO and LIGO-India: Scope and Plans for Gravitational Wave Research and Precision Metrology in India. *International Journal of Modern Physics D*, 2013.

[20] S. Hild. Beyond the second generation of laser-interferometric gravitational wave observatories. *Classical and Quantum Gravity*, 2012.

[21] P. Kwee, C. Bogan, K. Danzmann, M. Frede, H. Kim, P. King, J. Pöld, O. Puncken, R.L. Savage, F. Seifert, et al. Stabilized high-power laser system for the gravitational wave detector advanced LIGO. *Optics Express*, 2012.

[22] A.V. Cumming, A.S. Bell, L. Barsotti, M.A. Barton, G. Cagnoli, D. Cook, L. Cunningham, M. Evans, G.D. Hammond, G.M. Harry, et al. Design and development of the advanced LIGO monolithic fused silica suspension. *Classical and Quantum Gravity*.

[23] B.J. Meers. Recycling in laser-interferometric gravitational-wave detectors. *Physical Review D*, 1988.

[24] C.M. Caves. Quantum-mechanical noise in an interferometer. *Physical Review D*, 1981.

[25] LIGO Scientific Collaboration et al. A gravitational wave observatory operating beyond the quantum shot-noise limit. *Nature Physics*, 2011.

[26] H. Grote, K. Danzmann, K.L. Dooley, R. Schnabel, J. Slutsky, and H. Vahlbruch. First long-term application of squeezed states of light in a gravitational-wave observatory. *Physical Review Letters*, 2013.

[27] J.C. Maxwell. A dynamical theory of the electromagnetic field. *Proceedings of the Royal Society of London*, 13:531–536, 1863.

[28] J.C. Maxwell. On Governors. *Proceedings of the Royal Society of London*, 16:270–283, 1868.

[29] R.E. Kalman. A new approach to linear filtering and prediction problems. *Journal of basic Engineering*, 1960.

[30] M.H. Wimmer, D. Steinmeyer, K. Hammerer, and M. Heurs. Coherent cancellation of backaction noise in optomechanical force measurements. *Physical Review A*, 2014.

[31] A.G. Kallapur, D. Schuette, I.R. Petersen, T.K. Boyson, E.H. Huntington, S.Z. Sayed Hassen, H. Song, and M. Heurs. Design and implementation of an optical cavity locking controller test bed system. *Control Systems Technology, IEEE Transactions on*, 2015.

[32] D. Schütte, S.Z. Sayed Hassen, K.S. Karvinen, T.K. Boyson, A.G. Kallapur, H. Song, I.R. Petersen, E.H. Huntington, and M. Heurs. Experimental Demonstration of Frequency Autolocking an Optical Cavity Using a Time-Varying Kalman Filter. *Physical Review Applied*, 2016.

[33] C. Gerry and P. Knight. *Introductory quantum optics*. Cambridge University Press, 2005.

[34] H.A. Bachor and T. C. Ralph. *A Guide to Experiments in Quantum Optics, 2nd*. Wiley, 2004.

[35] W. Nolting. *Analytische Mechanik*, volume 2. Springer Science & Business Media, 2010.

[36] M. Planck. Über irreversible Strahlungsvorgänge. *Annalen der Physik*, 1900.

[37] W. Heisenberg. Über den anschaulichen Inhalt der quantentheoretischen Kinematik und Mechanik. *Zeitschrift für Physik*, 1927.

[38] R.J. Glauber. Coherent and incoherent states of the radiation field. *Physical Review*, 1963.

[39] C. Gardiner and P. Zoller. *Quantum noise: a handbook of Markovian and non-Markovian quantum stochastic methods with applications to quantum optics*. Springer Science & Business Media, 2004.

[40] R. W. Boyd. *Nonlinear optics*. Academic press, 2003.

[41] R.C. Eckardt, C.D. Nabors, W.J. Kozlovsky, and R.L. Byer. Optical parametric oscillator frequency tuning and control. *JOSA B*, 1991.

[42] W. Sellmeier. Zur Erklärung der abnormen Farbenfolge im Spectrum einiger Substanzen. *Annalen der Physik und Chemie*, 1871.

[43] M. Yamada, N. Nada, M. Saitoh, and K. Watanabe. First-order quasi-phase matched LiNbO3 waveguide periodically poled by applying an external field for efficient blue second-harmonic generation. *Applied Physics Letters*, 1993.

[44] D. Meschede. *Optik, Licht und Laser*. Springer-Verlag, 2009.

[45] H.P. Yuen and V.W.S. Chan. Noise in homodyne and heterodyne detection. *Optics Letters*, 1983.

[46] M. Heurs, I.R. Petersen, M.R. James, and E.H. Huntington. Homodyne locking of a squeezer. *Optics letters*, 2009.

[47] W. Demtröder. *Experimentalphysik 2*. Springer, 1995.

[48] R.C. Jones. A New Calculus for the Treatment of Optical Systems. Description and Discussion of the Calculus. *JOSA*, 1941.

[49] A. Freise and K. Strain. Interferometer Techniques for Gravitational-Wave Detection. *Living Rev. Relativity*, 2010.

[50] A. Siegman. *Lasers*. University Science Books, Mill Valley Calif., 1986.

[51] A.L. Schawlow and C.H. Townes. Infrared and optical masers. *Physical Review*, 1958.

[52] R.L. Barger, M.S. Sorem, and J.L. Hall. Frequency stabilization of a cw dye laser. *Applied Physics Letters*, 1973.

[53] R.W.P. Drever, J.L. Hall, F.V. Kowalski, J. Hough, G.M. Ford, A.J. Munley, and H. Ward. Laser phase and frequency stabilization using an optical resonator. *Applied Physics B*, 1983.

[54] D.A. Shaddock, M.B. Gray, and D.E. McClelland. Frequency locking a laser to an optical cavity by use of spatial mode interference. *Optics letters*, 1999.

[55] T.W. Hänsch and B. Couillaud. Laser frequency stabilization by polarization spectroscopy of a reflecting reference cavity. *Optics communications*, 1980.

[56] H. Kogelnik and T. Li. Laser beams and resonators. *Applied optics*, 1966.

[57] B. Willke. Stabilized lasers for advanced gravitational wave detectors. *Laser & Photonics Reviews*, 2010.

[58] M. Mehmet, S. Ast, T. Eberle, S. Steinlechner, H. Vahlbruch, and R. Schnabel. Squeezed light at 1550 nm with a quantum noise reduction of 12.3 dB. *Optics express*, 2011.

[59] B. Friedland. *Control system design: an introduction to state-space methods*. Courier Corporation, 2012.

[60] R.C. Dorf and R.H. Bishop. *Modern control systems*. Pearson (Addison-Wesley), 1998.

[61] G.F. Franklin, J.D. Powell, and A. Emami-Naeini. *Feedback control of dynamic systems*. Pearson, 1994.

[62] A. Abramovici and J. Chapsky. *Feedback control systems: A fast-track guide for scientists and engineers*. Springer Science & Business Media, 2012.

[63] Department of Mechanical Engineering Massachusetts Institute of Technology. Understanding poles and zeros.

[64] K.J. Åström. Control system design lecture notes. *Department of Mechanical and Environmental Engineering University of California Santa Barbara*, 2002.

[65] K. Ogata. *Modern control engineering*. Prentice Hall PTR, 2001.

[66] F.L. Lewis. *Optimal estimation: with an introduction to stochastic control theory*. Wiley New York et al., 1986.

[67] A.M.A. Hamdan and A.H. Nayfeh. Measures of modal controllability and observability for first-and second-order linear systems. *Journal of guidance, control, and dynamics*, 1989.

[68] D.K. Lindner, J. Babendreier, and A.M.A. Hamdan. Measures of controllability and observability and residues. *IEEE transactions on automatic control*, 1989.

[69] M. Tarokh. Measures for controllability, observability and fixed modes. *Automatic ControlIEEE Transactions on Automatic Control*, 1992.

[70] S.Z. Sayed Hassen. *Optimal and Robust Feedback Control of Quantum Systems*. PhD thesis, Australian Defence Force Academy, 2010.

[71] H. Kwakernaak and R. Sivan. *Linear optimal control systems*. Wiley-Interscience New York, 1972.

[72] P. Whittle. Risk-sensitive linear/quadratic/Gaussian control. *Advances in Applied Probability*, 1981.

[73] L.S. Ma and J.L. Hall. Optical heterodyne spectroscopy enhanced by an external optical cavity: toward improved working standards. *IEEE Journal of Quantum Electronics*, 1990.

[74] B.A. Paldus, C.C. Harb, T.G. Spence, B. Wilke, J. Xie, J.S. Harris, and R.N. Zare. Cavity-locked ring-down spectroscopy. *Journal of Applied Physics*, 1998.

[75] S. L. Braunstein and P. Van Loock. Quantum information with continuous variables. *Reviews of Modern Physics*, 2005.

[76] J.S. Neergaard-Nielsen, B.M. Nielsen, C. Hettich, K. Mølmer, and E.S. Polzik. Generation of a superposition of odd photon number states for quantum information networks. *Phys. Rev. Lett.*, 2006.

[77] N. Treps, U. Andersen, B. Buchler, P.K. Lam, A. Maître, H.A. Bachor, and C. Fabre. Surpassing the standard quantum limit for optical imaging using nonclassical multimode light. *Phys. Rev. Lett.*, 2002.

[78] J. Aasi, B. P. Abbott, R. Abbott, T. Abbott, M. R. Abernathy, K. Ackley, C. Adams, T. Adams, P. Addesso, R. X. Adhikari, et al. Advanced LIGO. *Classical and quantum gravity*, 2015.

[79] A.G. Kallapur, D. Schuette, I.R. Petersen, T.K. Boyson, E.H. Huntington, S.Z. Sayed Hassen, H. Song, and M. Heurs. Digital locking of a three-mirror ring cavity. In *2012 IEEE International Conference on Control Applications (CCA)*, 2012.

[80] S.Z. Sayed Hassen, M. Heurs, E.H. Huntington, I.R. Petersen, and M.R. James. Frequency locking of an optical cavity using linear–quadratic gaussian integral control. *Journal of Physics B: Atomic, Molecular and Optical Physics*, 2009.

[81] M. Heurs, E.H. Huntington, S.Z. Sayed Hassen, I.R. Petersen, and M.R. James. Laser Frequency Locking to an Optical Cavity using LQG Control. In *Quantum Communication, Measurement AND Computing (QCMC): Ninth International Conference on QCMC*, 2009.

[82] C. Cohen-Tannoudji, B. Diu, and F. Laloe. *Quantum Mechanics*. de Gruyter, 1978.

[83] P. Van Overschee and B.L.R. De Moor. *Subspace identification for linear systems: theory, implementation, applications*. Kluwer academic publishers Dordrecht, 1996.

[84] S. S. Aphale, S. R. Moheimani, and A. J. Fleming. Dominant resonant mode damping of a piezoelectric tube nanopositioner using optimal sensorless shunts. In *Proc. Amer. Contr. Conf*, 2007.

[85] S. S. Aphale, A. J. Fleming, and S. R. Moheimani. Integral resonant control of collocated smart structures. *Smart Materials and Structures*, 2007.

[86] L. Ljung. Prediction error estimation methods. *Circuits, Systems and Signal Processing*, 2002.

[87] J.P. Hespanha. *Linear systems theory*. Princeton university press, 2009.

[88] T. Glad and L. Ljung. *Control theory*. CRC press, 2000.

[89] J. Doyle. Guaranteed margins for LQG regulators. *IEEE Transactions on Automatic Control*, 1978.

[90] G. Heinzel. *Advanced optical techniques for laser-interferometric gravitational-wave detectors*. PhD thesis, Leibniz Universität Hannover, 1999.

[91] S.Z. Sayed Hassen and I.R. Petersen. Frequency locking of an optical cavity using a time-varying Kalman filtering approach. *IEEE Transactions on Control Systems Technology*, 2014.

[92] P. Kokotovic, H.K. Khalil, and J. O'Reilly. *Singular perturbation methods in control: analysis and design*. SIAM, 1999.

[93] F. S. Acton. *Numerical methods that usually work*. Mathematical Association of America Washington, DC, 1990.

[94] S. Goedecker. Remark on algorithms to find roots of polynomials. *SIAM Journal on Scientific Computing*, 1994.

[95] R. G. Brown. *Introduction to random signal analysis and Kalman filtering*. Wiley New York, 1983.

[96] R.E. Slusher, L.W. Hollberg, B. Yurke, J.C. Mertz, and J.F. Valley. Observation of squeezed states generated by four-wave mixing in an optical cavity. *Physical Review Letters*, 1985.

[97] H. Vahlbruch, A. Khalaidovski, N. Lastzka, C. Gräf, K. Danzmann, and R. Schnabel. The GEO 600 squeezed light source. *Classical and Quantum Gravity*, 2010.

[98] H. Vahlbruch, S. Chelkowski, B. Hage, A. Franzen, K. Danzmann, and R. Schnabel. Coherent control of vacuum squeezing in the gravitational-wave detection band. *Physical Review Letters*, 2006.

[99] A. Khalaidovski, H. Vahlbruch, N. Lastzka, C. Gräf, K. Danzmann, H. Grote, and R. Schnabel. Long-term stable squeezed vacuum state of light for gravitational wave detectors. *Classical and quantum gravity*, 2012.

[100] T. Denker. *High-precision metrology with high-frequency nonclassical light sources*. PhD thesis, Leibniz Universität Hannover, 2016.

[101] M.J. Collett and C.W. Gardiner. Squeezing of intracavity and traveling-wave light fields produced in parametric amplification. *Physical Review A*, 1984.

[102] COHERENT. Mephisto laser, http://www.coherent.com/products/.

[103] F. Herzog, K. Kudielka, D. Erni, and W. Bächtold. Optical phase locking by local oscillator phase dithering. *IEEE Journal of Quantum Electronics*, 2006.

[104] T. Aoki, G. Takahashi, and A. Furusawa. Squeezing at 946nm with periodically poled KTiOPO 4. *Optics express*, 2006.

[105] E.S. Polzik, J. Carri, and H.J. Kimble. Atomic spectroscopy with squeezed light for sensitivity beyond the vacuum-state limit. *Applied Physics B*, 1992.

[106] T.C. Zhang, K.W. Goh, C.W. Chou, P. Lodahl, and H.J. Kimble. Quantum teleportation of light beams. *Physical Review A*, 2003.

[107] J. Clarke, H. Wang, D. Brown, and A. Freise. Revisiting Sidebands of Sidebands in Finesse. 2013.

[108] W. Demtröder. *Experimentalphysik*. Springer, 2005.

[109] P.R. Saulson. *Fundamentals of interferometric gravitational wave detectors*. World scientific, 1994.

[110] T. Westphal, G. Bergmann, A. Bertolini, M. Born, Y. Chen, A.V. Cumming, L. Cunningham, K. Dahl, C. Gräf, G. Hammond, et al. Design of the 10 m AEI prototype facility for interferometry studies. *Applied Physics B*, 2012.

[111] S. Gossler, M.M. Casey, A. Freise, H. Grote, H. Lück, P. McNamara, M.V. Plissi, D.I. Robertson, N.A. Robertson, K. Skeldon, et al. The mode-cleaner system and suspension aspects of GEO600. *Classical and Quantum Gravity*, 2002.

[112] T. Westphal. *Coating thermal noise interferometer*. PhD thesis, Leibniz Universtität Hannover, 2016.

[113] S.M. Aston. *Optical read-out techniques for the control of test-masses in gravitational wave observatories*. PhD thesis, University of Birmingham, 2011.

[114] L. Carbone, S.M. Aston, R.M. Cutler, A. Freise, J. Greenhalgh, J. Heefner, D. Hoyland, N.A. Lockerbie, D. Lodhia, N.A. Robertson, et al. Sensors and actuators for the Advanced LIGO mirror suspensions. *Classical and Quantum Gravity*, 2012.

[115] M. Barton. Calculation and measurement of the OSEM actuator sweet spot position. Technical report, Tech. Rep. LIGO-T10000164-v3, LIGO Laboratory, 2010.

[116] F. Acernese, E. Calloni, R. De Rosa, L. Di Fiore, and L. Milano. An optical readout system for the drag-free control of LISA. *Classical and Quantum Gravity*, 2005.

[117] First Sensor. Part description qp50-6 to, http://www.first-sensor.com/en/products/optical-sensors/detectors/quadrant-pin-photodiodes-qp/.

[118] I.N. Bronstein, J. Hromkovic, B. Luderer, H.-R. Schwarz, J. Blath, A. Schied, S. Dempe, G. Wanka, S. Gottwald, E. Zeidler, et al. *Taschenbuch der Mathematik*. Springer-Verlag, 2012.

[119] B. Schulte. Untersuchung an mechanischen Aufhängungen und inter-
ferometrischen Topologien für zukünftige Gravitationswellendetektoren.
Master's thesis, Universität Bremen, 2015.

[120] R. Bork and LIGO Scientific Collaboration. AdvLIGO CDS design
overview. 2010.

[121] M. J. Balas. Feedback control of flexible systems. *Automatic Control,
IEEE Transactions on*, 1978.

[122] K.A. Strain and B. Shapiro. Damping and local control of mirror sus-
pensions for laser interferometric gravitational wave detectors. *Review of
Scientific Instruments*, 2012.

[123] B.N. Shapiro. *Adaptive modal damping for Advanced LIGO suspensions*.
PhD thesis, Massachusetts Institute of Technology, 2012.

[124] B. Shapiro, M. Barton, N. Mavalvala, R. Mittleman, and K. Youcef-Toumi.
Selection of important parameters using uncertainty and sensitivity analy-
sis. *IEEE/ASME Transactions on Mechatronics*, 2015.

[125] S. Skogestad and I. Postlethwaite. *Multivariable feedback control: analy-
sis and design*. Wiley New York, 2007.

[126] H. Kwakernaak. Robustness optimization of linear feedback systems. In
The 22nd IEEE Conference on Decision and Control, 1983.

[127] M. Verma and E. Jonckheere. L∞-compensation with mixed sensitivity
as a broadband matching problem. *Systems & control letters*, 1984.

[128] D. Blair, L. Ju, C. Zhao, L. Wen, H. Miao, R. Cai, J. Gao, X. Lin, D. Liu,
L.-A. Wu, et al. The next detectors for gravitational wave astronomy.
Science China Physics, Mechanics & Astronomy, 2015.

[129] S. Hild, M. Abernathy, F. Acernese, P. Amaro-Seoane, N. Andersson,
K. Arun, F. Barone, B. Barr, M. Barsuglia, M. Beker, et al. Sensitivity
studies for third-generation gravitational wave observatories. *Classical
and Quantum Gravity*, 2011.

[130] M.A. Mabrok, A.G. Kallapur, I.R. Petersen, D. Schuette, T.K. Boyson, and A. Lanzon. Locking a three-mirror optical cavity: A negative imaginary systems approach. In *2nd Australian Control Conference (AUCC)*, 2012.

Acknowledgements

ACKNOWLEDGEMENTS

CV and Publication List

PERSONAL DATA

Name:	Dirk Schütte
Address:	Voßstraße 9
	30161 Hannover
Nationality:	German
Date of birth:	04.02.1983
Place of birth:	Twistringen

ACADEMIC CAREER

10/2010 – 07/2016	PhD Thesis at Leibniz Universität Hannover
	Institute for gravitational physics
	AG Heurs - Quantum Control
	Modern control of a squeezer
10/2003 – 05/2010	Diploma thesis at Leibniz Universität Hannover
	Diploma thesis at Institute for gravitational physics
	AG Heinzel/Danzmann - LISA
	(Laser Interferometer Space Antenna)
	An InGaAs camera as real-time phasemeter and star-tracker

EXTRA CURRICULAR ACTIVITIES

04/2012	EECI Graduate School on Control *Quantum control and quantum information processing*
02/2013	Seminar *Presentation Skills*
01/2012	Seminar *Write about Science*
06/2010 – 10/2010	Research assistant: AG Laser Interferomter Space Antenna Institute for gravitational physics, Leibniz Universität Hannover

COLLABORATIONS

02/2011 – present	Member of *Ligo Scientific Collaboration* (LSC)
10/2011 – 12/2011	Visit to UNSW Canberra, School of Engineering and Information Technology (SEIT)

EDUCATION

06/1995 – 06/2002	Gymnasium Antonianum Vechta

PERSONAL INTERESTS

Sports	Active member in a variety of sports clubs since 1988: Tennis, Football, Badminton, Table Tennis

Hannover, August 17, 2016

2016

[1] Abbott B. P., ..., **D. Schuette**, ..., et al.. Observation of Gravitational Waves from a Binary Black Hole Merger. *Phys. Rev. Lett.*, **116**(6),061102.

[2] **D. Schuette**, S.Z. Sayed Hassen, K. S. Karvinen, T. K. Boyson, A.G. Kallapur, H. Song, I. R. Petersen, E. H. Huntington and M. Heurs. Experimental Demonstration of Frequency Autolocking an Optical Cavity Using a Time-Varying Kalman Filter. *Phys. Rev. Applied*, **5**(1),014005.

[3] Abbott B. P., ..., **D. Schuette**, ..., et al.. Astrophysical Implications of the Binary Black-Hole Merger GW150914. *Astrophys. J.*, **818**(2),L22.

[4] Abbott B. P., ..., **D. Schuette**, ..., et al.. Localization and broadband follow-up of the gravitational-wave transient GW150914. *eprint arXiv:*, 1602.08492, (astro-ph.HE).

[5] Abbott B. P., ..., **D. Schuette**, ..., et al.. GW150914: Implications for the stochastic gravitational wave background from binary black holes. *eprint arXiv:*, 1602.03847, (gr-qc).

[6] Abbott B. P., ..., **D. Schuette**, ..., et al.. Calibration of the Advanced LIGO detectors for the discovery of the binary black-hole merger GW150914. *eprint arXiv:*, 1602.03845, (gr-qc).

[7] Abbott B. P., ..., **D. Schuette**, ..., et al.. Characterization of transient noise in Advanced LIGO relevant to gravitational wave signal GW150914. *eprint arXiv:*, 1602.03844, (gr-qc).

[8] Abbott B. P., ..., **D. Schuette**, ..., et al.. Observing gravitational-wave transient GW150914 with minimal assumptions. *eprint arXiv:*, 1602.03843, (gr-qc).

[9] Abbott B. P., ..., **D. Schuette**, ..., et al.. The Rate of Binary Black Hole Mergers Inferred from Advanced LIGO Observations Surrounding GW150914. *eprint arXiv:*, 1602.03842, (astro-ph.HE).

[10] Abbott B. P., ..., **D. Schuette**, ..., et al.. Tests of general relativity with GW150914. *eprint arXiv:*, 1602.03841, (gr-qc).

[11] Abbott B. P., ..., **D. Schuette**, ..., et al.. Properties of the binary black hole merger GW150914. *eprint arXiv:*, 1602.03840, (gr-qc).

[12] Abbott B. P., . . . , **D. Schuette**, . . . , et al.. GW150914: First results from the search for binary black hole coalescence with Advanced LIGO. *eprint arXiv:*, 1602.03839, (gr-qc).

[13] Abbott B. P., . . . , **D. Schuette**, . . . , et al.. GW150914: The Advanced LIGO Detectors in the Era of First Discoveries. *eprint arXiv:*, 1602.03838, (gr-qc).

[14] Adrian-Martinez, S., . . . , **D. Schuette**, . . . , et al.. High-energy Neutrino follow-up search of Gravitational Wave Event GW150914 with ANTARES and IceCube. *eprint arXiv:*, 1602.05411, (astro-ph.HE).

[15] Aasi, J., . . . , **D. Schuette**, . . . , et al.. Search of the Orion spur for continuous gravitational waves using a loosely coherent algorithm on data from LIGO interferometers. *Phys. Rev.*, **D93**(4),042006.

[16] Aasi, J., . . . , **D. Schuette**, . . . , et al.. First low frequency all-sky search for continuous gravitational wave signals. *Phys. Rev.*, **D93**(4),042007.

2015

[1] T. Denker, **D. Schütte**, M. H. Wimmer, T. A. Wheatley, E. H. Huntington, and M. Heurs. Utilizing weak pump depletion to stabilize squeezed vacuum states. *Opt. Express*, **23**(13),16517.

[2] A. G. Kallapur, **D. Schuette**, I. R. Petersen, T. K. Boyson, E. H. Huntington, S.Z. Sayed Hassen, H. Song and M. Heurs. Design and Implementation of an Optical Cavity Locking Controller Test Bed System. *Control Systems Technology, IEEE Transactions*, **23**(2),715–721.

[3] Aasi, J., . . . , **D. Schuette**, . . . , et al.. Advanced LIGO. *Class. Quant. Grav.*, **32**,074001.

[4] Aasi, J., . . . , **D. Schuette**, . . . , et al.. Directed search for gravitational waves from Scorpius X-1 with initial LIGO data. *Phys. Rev.*, **D91**(6),062008.

[5] Aasi, J., . . . , **D. Schuette**, . . . , et al.. Characterization of the LIGO detectors during their sixth science run. *Class. Quant. Grav.*, **32**(11),115012.

[6] Aasi, J., . . . , **D. Schuette**, . . . , et al.. Searches for continuous gravitational waves from nine young supernova remnants. *Astrophys J.*, **813**(1),39.

[7] Aasi, J., . . . , **D. Schuette**, . . . , et al.. Narrow-band search of continuous gravitational-wave signals from Crab and Vela pulsars in Virgo VSR4 data. *Phys. Rev.*, **D91**(2),022004.

[8] Aasi, J., ..., **D. Schuette**, ..., et al.. Searching for stochastic gravitational waves using data from the two colocated LIGO Hanford detectors. *Phys. Rev.*, **D91**(2),022003.

2014

[1] Aartsen, M. G., ..., **D. Schuette**, ..., et al.. Multimessenger search for sources of gravitational waves and high-energy neutrinos: Initial results for LIGO-Virgo and IceCube. *Phys. Rev.*, **D90**(10),102002.

[2] Aasi, J., ..., **D. Schuette**, ..., et al.. Application of a Hough search for continuous gravitational waves on data from the fifth LIGO science run. *Class. Quant. Grav.*, **31**,085014.

[3] Aasi, J., ..., **D. Schuette**, ..., et al.. Gravitational waves from known pulsars: results from the initial detector era. *Astrophys. J.*, **785**,119.

[4] Aasi, J., ..., **D. Schuette**, ..., et al.. First Searches for Optical Counterparts to Gravitational-wave Candidate Events. *Astrophys. J. Suppl.*, **211**,7.

[5] Aasi, J., ..., **D. Schuette**, ..., et al.. Constraints on cosmic strings from the LIGO-Virgo gravitational-wave detectors.
Phys. Rev. Lett., **122**,131101.

[6] Aasi, J., ..., **D. Schuette**, ..., et al.. Search for gravitational wave ringdowns from perturbed intermediate mass black holes in LIGO-Virgo data from 2005-2010. *Phys. Rev.*, **D89**(10),102006.

[7] Aasi, J., ..., **D. Schuette**, ..., et al.. Methods and results of a search for gravitational waves associated with gamma-ray bursts using the GEO600, LIGO, and Virgo detectors. *Phys. Rev.*, **D89**(12),122004.

[8] Aasi, J., ..., **D. Schuette**, ..., et al.. First all-sky search for continuous gravitational waves from unknown sources in binary systems. *Phys. Rev.*, **D90**(6),062010.

[9] Aasi, J., ..., **D. Schuette**, ..., et al.. Search for gravitational waves associated with γ-ray bursts detected by the Interplanetary Network. *Phys. Rev. Lett.*, **113**(1),011102.

[10] Aasi, J., ..., **D. Schuette**, ..., et al.. Search for gravitational radiation from intermediate mass black hole binaries in data from the second LIGO-Virgo joint science run. *Phys. Rev.*, **D89**(12),122003.

[11] Aasi, J., ..., **D. Schuette**, ..., et al.. Implementation of an *F*-statistic all-sky search for continuous gravitational waves in Virgo VSR1 data. *Class. Quant. Grav.*, **31**,165014.

[12] Aasi, J., ..., **D. Schuette**, ..., et al.. The NINJA-2 project: Detecting and characterizing gravitational waveforms modelled using numerical binary black hole simulations. *Class. Quant. Grav.*, **31**,115004.

[13] Aasi, J., ..., **D. Schuette**, ..., et al.. Improved Upper Limits on the Stochastic Gravitational-Wave Background from 2009-2010 LIGO and Virgo Data. *Phys. Rev. Lett.*, **113**(23),231101.

[14] Acernese F., ..., **D. Schuette**, ..., et al.. Concepts and research for future detectors. *Gen. Rel. Grav.*, **46**(5),1700.

2013

[1] Aasi, J., ..., **D. Schuette**, ..., et al.. Directed search for continuous gravitational waves from the Galactic center. *Phys. Rev.*, **D88**(10),102002.

[2] Aasi, J., ..., **D. Schuette**, ..., et al.. Search for long-lived gravitational-wave transients coincident with long gamma-ray bursts.
Phys. Rev., **D88**(12),122004.

[3] Aasi, J., ..., **D. Schuette**, ..., et al.. Prospects for Observing and Localizing Gravitational-Wave Transients with Advanced LIGO and Advanced Virgo. *eprint arXiv:*, 1304.0670, (gr-qc).

[4] Aasi, J., ..., **D. Schuette**, ..., et al.. Enhancing the sensitivity of the LIGO gravitational wave detector by using squeezed states of light. *Nature Photon.*, 7, 613-619.

2012

[1] A. G. Kallapur, **D. Schuette**, I. R. Petersen, T. K. Boyson, E. H. Huntington, S.Z. Sayed Hassen, H. Song and M. Heurs. Digital Locking of a three-mirror ring cavity. *Control Applications (CAA), 2012 IEEE International Conference proceeding*, ,794–799.

[2] M. A. Mabrok, A. G. Kallapur, I. R. Petersen, **D. Schuette**, T. K. Boyson, and A. Lanzon. Locking a three-mirror optical cavity: A negative imaginary systems approach. *Control Conference (AUCC) proceeding*, **2**,476–480.